Università degli Studi di Bologna

FACOLTÀ DI SCIENZE MATEMATICHE, FISICHE E NATURALI

Dipartimento di Astronomia

Dynamical Models of Elliptical Galaxies with Central Black Hole

Tesi di Dottorato di:
Andrea Riciputi

Relatore:
Prof. Bruno Marano

Correlatori:
Prof. Luca Ciotti
Dott. Pasquale Londrillo

Coordinatore:
Prof. Gabriele Giovannini

Dottorato di Ricerca in Astronomia
Ciclo XVII

Università degli Studi di Bologna

FACOLTÀ DI SCIENZE MATEMATICHE, FISICHE E NATURALI

Dipartimento di Astronomia

Dynamical Models of Elliptical Galaxies with Central Black Hole

Tesi di Dottorato di:
Andrea Riciputi

Relatore:
Prof. Bruno Marano

Correlatori:
Prof. Luca Ciotti
Dott. Pasquale Londrillo

Coordinatore:
Prof. Gabriele Giovannini

Dottorato di Ricerca in Astronomia

Ciclo XVII

Università degli Studi di Bologna

Facoltà di Scienze Matematiche, Fisiche e Naturali

Dipartimento di Astronomia

Dynamical Models of Elliptical Galaxies with Central Black Hole

Tesi di Dottorato di:	Relatore:
Andrea Riciputi	Prof. Bruno Marano

Correlatori:
Prof. Luca Ciotti
Dott. Pasquale Londrillo

Coordinatore:
Prof. Gabriele Giovannini

Dottorato di Ricerca in Astronomia
Ciclo XVII

To my parents

Contents

List of Figures

Abstract

Elliptical galaxies are stellar system characterized by a very complex intrinsic dynamics, which is tightly connected with their formation process in a way that it has not yet been understood. Observations and detailed analysis reveals that many of their relevant observable quantities depend systematically on some of their global properties, i.e. elliptical galaxies satisfy a few *empirical scaling relations*.

In the present work we focus our attention on two of the scaling relations, the Fundamental Plane and the $M_{\rm BH}$-σ_0 relations, and on the estimate of rotational support presents in ellipticals by means of the so-called v/σ-ϵ plane.

To get a better understanding of these issues, we have adopted a collisionless *axisymmetric two-integrals oblate* model to describe early-type galaxies and we have developed a numerical code to solve its intrinsic and project dynamics.

We found that projection effects only marginally contribute to the Fundamental Plane thickness, 90% of it being attributable to real variations of the physical properties from galaxy to galaxy. Moreover we found that the aperture velocity dispersion (i.e. the velocity dispersion usually measured through the observations) weakly depends on the presence/absence of a central BH demonstrating that the observed $M_{\rm BH}$-σ_0 relation is a non trivial property of elliptical galaxies and bulges. Finally, we found that a note of caution should be used when interpreting the position of galaxies in the v/σ-ϵ diagram as a measure of their degree of rotational support, since in observations the *central* kinematical properties are adopted, instead of the virial ones. Further application of the developed code are in progress.

Chapter 1

Introduction

Elliptical galaxies have been supposed to be simple objects from an astrophysical, and in particular from the dynamical point of view until late 70s, when it became clear that they are not classical rotation ellipsoids (e.g. Binney 1976; Illingworth 1977, and references therein). Nowadays ellipticals are known to be stellar system characterized by a very complex intrinsic dynamics, which is tightly connected with their formation process in a way that it has not yet been fully understood. Moreover, a detailed analysis reveals that many relevant observable quantities of ellipticals (such as their X-ray luminosity) depend systematically on some of their global properties, such as their total mass or optical luminosity. In other words, elliptical galaxies satisfy several *empirical scaling relations*, among which two of the most studied, and probably of the most important, are the Fundamental Plane relation (Djorgovski & Davis 1987; Dressler et al. 1987), and the so-called $M_{\rm BH}$-σ_0 relation (Ferrarese & Merritt 2000; Gebhardt et al. 2000). In the present work we have focused our attention to some of the open questions in this field, in particular we have tried to get more insight in the problem of the thickness of the Fundamental Plane, (Section 1.1), in the definition of the super-massive black hole sphere of influence and of its importance for the $M_{\rm BH}$-σ_0 scaling relation, (Section 1.2), and in the problem of the rotational support of elliptical galaxies (Section 1.3). Finally, in Section 1.4 further applications of this work are briefly outlined.

1.1 Fundamental Plane relation

Elliptical galaxies are a remarkably regular family of stellar systems, that are quite similar in their main structural and dynamical properties, as apparent from both photometric and spectroscopic observations. They also satisfy several (more or less tight) scaling relations, that connect their intrinsic and observational properties. The Fundamental Plane (hereafter, FP) relation (Djorgovski & Davis 1987; Dressler et al. 1987) involves the circularized effective radius R_e, the mean effective surface brightness $\langle \mu_e \rangle$, and the central velocity dispersion σ_0 of ellipticals, and is characterized by a remarkably small scatter (see Figure 1.1). Beyond that, other scaling relations exist, such as the Faber-Jackson relation (Faber & Jackson 1976) that indicate that the central velocity dispersion increases systematically as a function of the galaxy optical luminosity, or the Kormendy relation (Kormendy 1977) that indicates that circularized effective radius increases as a function of the galaxy luminosity.

Also the characteristic of the stellar populations of the ellipticals galaxies are strictly correlated with their total luminosity and internal dynamics, as shown by the color-magnitude relation (Bower et al. 1992) and by the Mg_2-σ_0 relation (e.g. Burstein et al. 1988; Bender et al. 1993). In addition, it is now widely accepted that central super-massive black holes (BH) are a common characteristic of spheroidal stellar systems (e.g. Kormendy & Richstone 1995; van der Marel 1999; de Zeeuw 2001). It has also been found that their mass (M_{BH}) is linearly proportional to the stellar mass (or luminosity) of the host galaxy or bulge, the so-called *Magorrian relation* (Magorrian et al. 1998), and it is even more tightly correlated with the spheroid central stellar velocity dispersion through the M_{BH}-σ_0 relation (Gebhardt et al. 2000; Ferrarese & Merritt 2000). The existence of these scaling relations is of great importance in the context of galaxy formation and evolution studies. The fact that they break the scale-free nature of the gravity indicates that they contain clues on the not purely dynamical mechanisms responsible for galaxy formation and evolution. Therefore, it is apparent that the global scaling relations of ellipticals are teaching us something about how these stellar system were formed and evolved in the cosmological context. The complete understanding of these relations and of the physical reasons behind them are one of the most open and challenging issue in modern astrophysics.

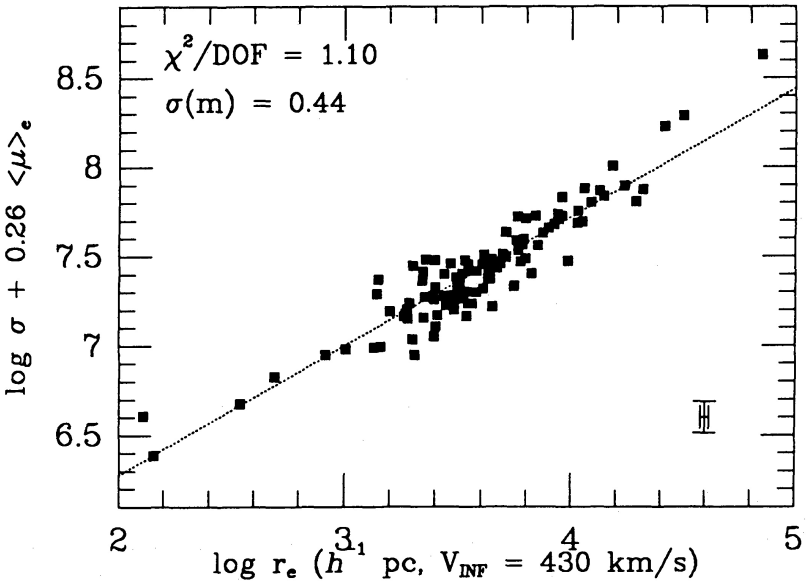

Figure 1.1 – The Fundamental Plane space seen edge-on; its thickness and tight correlation are evident. The dotted line represents the least-squares fits, median errors are indicated by the error bars in the lower left corner. Reduced chi-squares, χ^2/DOF, and estimated error of relations when used as distance predictors, expressed in magnitudes, $\sigma(m)$, are shown in upper left corner. (After Djorgovski & Davis 1987.)

In the first point of this Thesis we will focus on the FP relation, and in particular on the problem of its thickness. In the observational three-dimensional space of central velocity dispersion σ_0, *circularized* effective radius R_e, and mean surface brightness within the effective radius I_e, early-type galaxies approximately locate on a plane, the Fundamental Plane indeed, and represented by the best-fit relation:

$$\log R_e = a \log \sigma_0 + b \log I_e + c. \tag{1.1}$$

The coefficients a, b, and c depend slightly on the considered photometric band (e.g. Pahre et al. 1998; Scodeggio et al. 1998). By measuring R_e in kpc, σ_0 in km/s, and $I_e = L/(2\pi R_e^2)$ in $L_\odot/\mathrm{pc}^2$ (where L is the total galaxy luminosity), reported values in the Gunn r band are $a = 1.24 \pm 0.07$,

$b = -0.82 \pm 0.02$, $c = 0.182$[1] (Jørgensen et al. 1996). One of the most striking observational properties of the FP is its small and nearly constant scatter: the distribution of $\log R_e$ around the best-fit FP has a measured *rms* (after correction for measurement errors), that corresponds to a scatter in R_e at fixed σ_0 and I_e ranging from 15% to 20% (e.g. Faber et al. 1987; Jørgensen et al. 1996).

For a stationary stellar system the scalar virial theorem (see Binney & Tremaine 1987) can be written as

$$\frac{G\Upsilon_* L}{R_e} = K_{\rm V}\,\sigma_0^2, \tag{1.2}$$

where Υ_* is the *stellar* mass-to-light ratio in the photometric band used for the determination of L and R_e, while the coefficient $K_{\rm V}$ takes into account projection effects, the specific mass density, the stellar orbital distribution (such as velocity dispersion anisotropy and rotational support), and the effects related to the presence of dark matter. Equations (1.1) and (1.2) imply that in real galaxies, no matter how complex their structure is, $\Upsilon_*/K_{\rm V}$ is a well-defined function of any two of the three observables (L, R_e, σ_0). For example, by eliminating σ_0 from Equations (1.1) and (1.2) one obtains that along the FP

$$\frac{\Upsilon_*}{K_{\rm V}} \propto R_e^{(2+4b+a)/a}\,L^{-(2b+a)/a}, \tag{1.3}$$

where the dependence of the ratio $\Upsilon_*/K_{\rm V}$ on galaxy properties is commonly referred as the "FP tilt". The physical content of Equation (1.3) is truly remarkable: all stellar systems described by Equation (1.2) are in virial equilibrium, but only those for which $\Upsilon_*/K_{\rm V}$ scales according to Equation (1.3) (and with the same scatter) correspond to real galaxies. In other words, Equation (1.3) indicates that *structural/dynamical* ($K_{\rm V}$) and *stellar population* (Υ_*) properties in real galaxies are strictly connected, possibly as a consequence of their formation process: understanding the origin of the FP tilt is thus of the out most importance for the understanding of galaxy formation.

---

[1] This value of c refers to the Coma cluster and to $H_0 = 50\,{\rm km\,s^{-1}\,Mpc^{-1}}$.

A first possibility in this direction is to focus on the variation of a *single* galaxy property among the plethora in principle appearing in the quantity $\Upsilon_*/K_{\rm V}$, while fixing all the others to some prescribed value: we call this approach *orthogonal exploration* of the parameter space. For instance, one can explore the possibility that a systematic variation of Υ_* with L is at the origin of the FP tilt, while considering the galaxies as strictly homologous systems (i.e., with density and dynamical structures only differing for the physical scales, and thus $K_{\rm V} = {\rm const}$. See Bender et al. 1992; Renzini & Ciotti 1993; van Albada et al. 1995; Prugniel & Simien 1996). Another possibility is to enforce a constant Υ_*, and to assume that the galaxy density profiles, dark matter content and distribution, stellar orbital distribution, and so on, vary systematically with L (e.g. Ciotti & Pellegrini 1992; Caon, Capaccioli, & D'Onofrio 1993; Renzini & Ciotti 1993; Djorgovski 1995; Hjorth & Madsen 1995; Graham & Colless 1995; Ciotti, Lanzoni, & Renzini 1996; Ciotti & Lanzoni 1997; Prugniel & Simien 1997; Bertin, Ciotti, & Principe 2002).

Orthogonal explorations lead to important results, but, besides starting from a (more or less) well motivated choice of the specific parameter assumed to be responsible for the FP tilt, they also bring to a *fine tuning* problem: the large variation of such a parameter along the FP, necessary to reproduce the tilt, must be characterized by a small scatter of it at any fixed position on the FP in order to preserve the observed small thickness (e.g. Renzini & Ciotti 1993). Moreover, the severity of the fine tuning problem is strengthened by the unavoidable projection effects associated with the three-axial shape of early-type galaxies, if they also contribute to FP thickness. Thus, *the interpretation of the FP cannot be limited to the study of its tilt only, but requires to take consistently into account also its thinness* (see Ciotti 1997, for a full discussion of this problem).

Alternatively to the orthogonal exploration method, a statistical approach to this problem, based on Monte-Carlo simulations can be adopted (Bertin et al. 2002). In this study the authors showed that, ascribing the origin of the FP tilt to the *combined* effect of luminosity dependent mass-to-light ratio and shape parameter m in spherically symmetric and isotropic $R^{1/m}$ models (Sersic 1968), can reconcile the FP tilt with the observed large dispersion of m at fixed galaxy luminosity. Note, however, that in the Bertin et al. (2002) analysis the assumed models are *spherical symmetric*, so that the FP thickness is entirely produced by variations from galaxy to galaxy of their *physical* properties. On the other hand, elliptical galaxies are in general non spherical, and the quantities entering the FP expression do depend on the *observation angle*: it is therefore of great interest to estimate the contribution of *projection effects* to the FP thickness, and to quantify its *physical* scatter. Few analytical works have addressed this issue in the past (e.g. Faber et al. 1987; Saglia et al. 1993; Jørgensen et al. 1993; Prugniel & Simien 1994; Jørgensen et al. 1996; van Albada et al. 1995), their conclusions pointing in the direction of a *small contribution* of projection effects to the FP thickness. A different source of information on projection effects is also represented by the end-products of N-body numerical simulations (e.g. Pentericci et al. 1995; Nipoti et al. 2002, 2003b,a; Gonzáles & van Albada 2003). The impression one gets from these simulations is that projection effects can be *significant contributors* to the FP thickness, the range spanned by the models for changing viewing angle being comparable to *rms* scatter of the FP or more.

Recently Lanzoni & Ciotti (2003) have tried to address this issue applying the Monte-Carlo approach to the fully analytical axysimmetric Ferrers (1877) galaxy models. They have found indication that projection effects *marginally* contribute to the observed FP thickness. However Ferrers models are truncated and unrealistically flatter than real galaxies in the central regions, so that doubts can be risen about the reliability of the values of their central velocity dispersion (σ_0), thus leaving the needs to further explore this issue with more realistic galaxy models. In this Thesis, we explore this problem by adopting more realistic galaxy models (see also Riciputi et al. 2005).

1.2 $M_{\mathbf{BH}}$-σ_0 scaling relation

Super-massive black holes (BHs) are found at the center of most elliptical galaxies and bulges of spiral galaxies (e.g. Kormendy & Richstone 1995; van der Marel 1999; de Zeeuw 2001). The mass of these objects in in the range $10^6 \div 10^9\, M_\odot$ and it correlates very well with the central velocity dispersion (σ_0) of the host spheroid (Ferrarese & Merritt 2000; Gebhardt

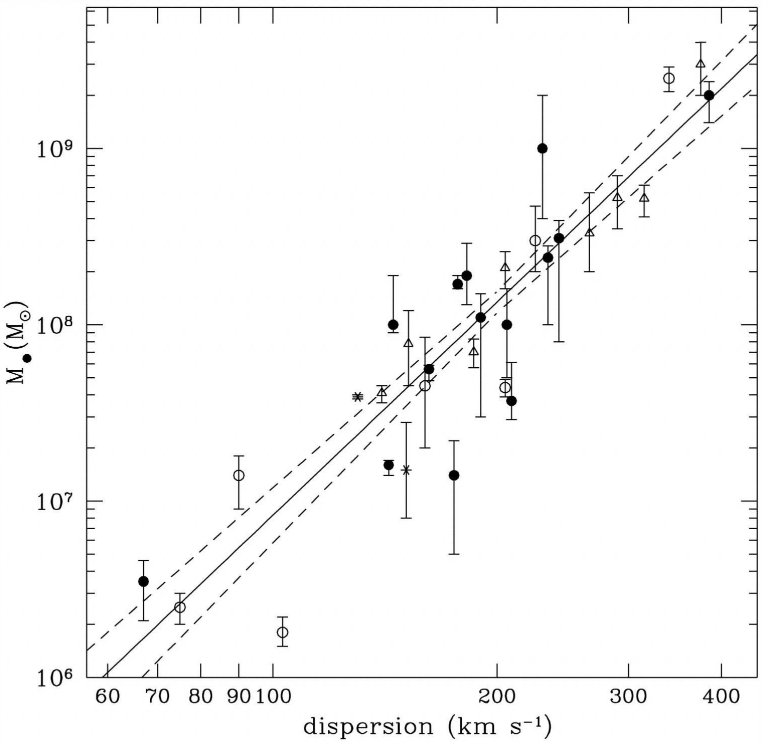

Figure 1.2 – $M_{\rm BH}$-σ_0 relation as proposed by Tremaine et al. (2002). The best-fit is represented by the solid line, while dashed lines show the 1 σ limits on the best-fit correlation. Black hole masses measured by stellar dynamics are denoted by circles (○), those measured by gas kinematic are denoted by triangles (△), those measured by maser kinematic are denoted by asterisks (∗), and Nuker measurements are denoted by filled circles (●).

et al. 2000) as showed in Figure 1.2. The relation can be written in the form:

$$\log\left(\frac{M_{\rm BH}}{M_\odot}\right) = \alpha \log\left(\frac{\sigma_0}{200\,{\rm km\,s^{-1}}}\right) + \beta \qquad (1.4)$$

where the original estimates of the coefficients, and in particular of the slope α, were different, with Gebhardt et al. (2000) who found $\alpha = 3.75 \pm 0.3$, and Ferrarese & Merritt (2000) who found $\alpha = 4.8 \pm 0.5$. Later works from the same authors gave more similar results: $\alpha = 4.58 \pm 0.52$ according to Ferrarese (2001), and $\alpha = 4.02 \pm 0.32$ according to Tremaine et al. (2002). The possible sources of the difference in the values of the slope have been discussed by Merritt & Ferrarese (2001b) and Tremaine et al. (2002). For the value of the intercept β, we recall that $\beta = 8.13 \pm 0.06$ and $\beta = 8.22 \pm 0.08$ are found by Tremaine et al. (2002) and Ferrarese (2001), respectively. Despite the debate about the exact value of the slope, there is general agreement on the fact that the $M_{\rm BH}$-σ_0 relation has a very small intrinsic dispersion (about $0.25 \div 0.3$ dex in BH mass for fixed σ_0). The *real* reason behind the fact that a local quantity as the black hole mass ($M_{\rm BH}$) and a global property of the host spheroid as the velocity dispersion (σ_0) are so tightly linked together are still far away from a complete comprehension, but seems to point out that the correct interpretation of elliptical galaxy formation should be similar to the so-called *monolithic* galaxy formation scenario (Eggen, Lynden-Bell, & Sandage 1962, see also Ciotti & van Albada 2001 and Nipoti, Londrillo, & Ciotti 2003b). In particular a still open issue regards whether the BH presence directly affects the stars velocity dispersion, making the $M_{\rm BH}$-σ_0 relation a trivial one, or not. In order to get a better understanding of this fact it is required to study in detail the dynamics of the central regions of *realistic* galaxy models, how far the *sphere of influence* of the BH extends and how much it affects the velocity dispersions fields.

It is worth noting here that a further scale relation regarding BH masses exists. It has been found by Kormendy & Richstone (1995) and Magorrian et al. (1998), and it shows a linear correlation between the *mass* of the BH and the *total luminosity* of the host spheroid. This relation, usually known as *Magorrian relation*, is characterized by a quite large intrinsic scatter, nevertheless it can be used to have a rough estimate of the central BH by simply measuring the total luminosity of an elliptical galaxy. Moreover, supposing a *constant* mass-to-light ratio ($\Upsilon_* =$ cost.), as it is the case in the present work, the Magorrian relation can be easily used to link together the total stellar mass of the host galaxy with the mass of the central supermassive black hole.

1.3 Rotation in elliptical galaxies

When in late 70s it becomes evident that elliptical galaxies were not classical rotation ellipsoids (for a complete discussion of the subject see Chandrasekhar 1969), and that their shape was not due to the ordered rotational

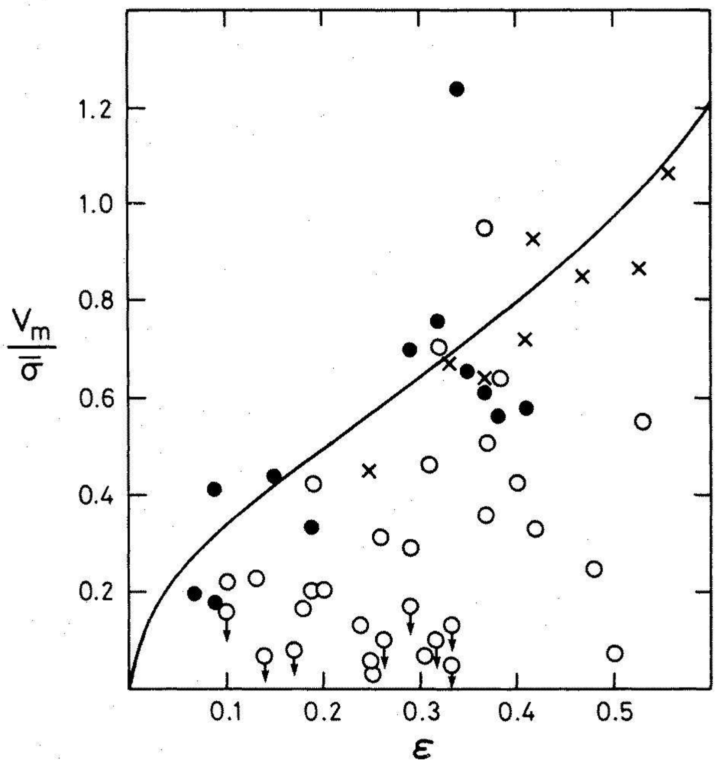

Figure 1.3 – v/σ-ϵ plane after Davies et al. (1983). Faint ellipticals are shown as filled circles, bright ellipticals are shown as open circle, and the bulges of disk galaxies as crosses. The solid line shows the theoretical loci for the oblate galaxies with isotropic velocity dispersions (i.e. classical rotation ellipsoids). Note that in this plot the theoretical curve is already corrected for a "mean" projection effect.

motions, it was suggested that their observed flattening was related to the anisotropy of the velocity dispersion tensor (e.g. Binney 1976; Illingworth 1977). In order to further study whether the ellipticals flattening is only due to ordered motions (*isotropic rotators*) or not, Binney (1978), firstly introduced a new tool: the so-called v/σ-ellipticity plane. Starting from the *scalar virial theorem* applied to classical rotation ellipsoids, he found a relation between the ratio of the ordered rotation to the velocity dispersion (v/σ), and the galaxy ellipticity (ϵ). It is important to stress here that this theoretical relation is derived under the hypothesis that ellipticals are modeled as classical isotropic rotators, with a density distribution stratified over similar ellipsoids (i.e. *homeoids*). In this plane the measurement of the ratio

(v/σ), and the observed ellipticity (ϵ) are usually compared to the theoretical curve derived by Binney representing the behavior of classical spheroids. The place where the observed galaxies are on this plane gives a measure of ordered and random motions present in the galaxies. In Figure 1.3 the v/σ-ϵ plane is shown, after Davies et al. (1983). It is worth noting that most of the galaxies (especially the brighter ones) are located below the theoretical curve, and this results is usually interpreted as the fact that, while low luminosity ellipticals are well represented by *isotropic rotators*, the bigger ones are supported by *velocity dispersion anisotropy.*

However, such a comparison may be misleading, because (1) galaxies need not to conform to the properties of classical spheroids, with density stratified on homeoidal surfaces (Roberts 1962), (2) the observations sample the central regions and may thus provide insufficient information for a proper comparison with the theoretical expectations, and (3) projection effects may alter the position of the observed ellipticals on the plane. Indeed, Evans & de Zeeuw (1994), in the study of their "power-law" models, noted that their *nearly* isotropic models are associated with points in the v/σ-ϵ plane systematically below the curve of the classical spheroids, which is obtained from virial (and therefore integrated) quantities. Nevertheless, this problem is worth to be studied in further detail, since the models proposed by Evans & de Zeeuw (1994) have a density distribution not stratified over homeoids, and a totally isotropic velocity dispersion tensor cannot be defined for them, thus violating two of the hypothesis made by Binney deriving the theoretical curve. The analysis of Evans & de Zeeuw has been confirmed by the work of Ciotti & Bertin (2005), based on a different and simpler analysis.

1.4 Present and further applications

All the topics discussed so far are pointing toward the needs of better modeling elliptical galaxies. These needs require models whose density distribution and intrinsic dynamics resemble as closely as possible those of the *real* early-type galaxies, leaving us still able to deal with the mathematics necessary to make quantitative prediction from the models itself. As it will be explained in the following Chapters, adopting *oblate axisymmetric cuspy models* with a density distribution stratified over *homeoids*, and an intrinsic dynamics driven by the *Collisionless Boltzmann Equation*, is a good starting point. A complete understanding of the *intrinsic* and *projected dynamics* of the adopted models is thus required in order to get more insight in the issues outlined in the previous Sections. However, as it will be explained in the following, the task of recovering the intrinsic and projected dynamical fields, for a selected model with a prescribed density distribution, cannot be accomplished without resorting to the numerical approach. After giving a theoretical framework of the problem in Chapter 2, Chapter 3 outlines the implementation of the numerical code which represents one of the main results of this Thesis. In Chapter 4 a brief description of the adopted models is provided, and finally in Chapter 5 the results so far achieved are described.

However the applications of this works do not end with the problems outlined above. Many more issue related to elliptical galaxies, and even bulges of spiral galaxies can be tackled with the aid of the numerical tool developed during this work. Among all these possibilities, it has been considered at the moment to apply the developed code to the problem of measuring the Hubble constant H_0 by means of the gravitational lensing. This technique has been first proposed in a seminal paper by Refsdal (1964) who realized that the multiple images of a variable background source generated by a foreground gravitational lens show a time delay $\Delta\tau$ which is proportional to the absolute scale of the source-lens-observer system and does depends on H_0. In particular he showed that the quantity $H_0\,\Delta\tau$ depends only on the lens model and the redshifts of the lens and the background source (for a complete discussion of this and other related topics see Narayan & Bartelmann 1999, and references therein). Being the time delay $\Delta\tau$, the source redshift, and the lens redshift measured with the observations, an accurate lens model which reproduces the position and magnification of the images yield a value for the Hubble constant. The main advantage of determining the H_0 through gravitational lensing over other methods are: (1) the ability of the method to deal with distant object where peculiar velocities are negligible when compared to the Hubble flow, (2) it does not rely on any distance ladder, so being independent of every other method, (3) it is based on fundamental physics (i.e. General Relativity), which is fully tested in the relevant weak-field limit of gravity. Nevertheless there is a drawback, that consists in the existing degeneracy between the lens mass profile and H_0. It has been shown recently that a combination of stellar kinematics and gravitational lensing can be used to place tight constraints on the mass distribution of the lens (usually an early-type galaxy) inside its Einstein radius (see Koopmans & Treu 2002; Treu & Koopmans 2002a), and hence made a good estimation of the value of the Hubble constant. However the mass distribution models for the lens adopted so far are spherical, leaving unanswered the question how a flattened shape for the lens affect the estimates for H_0. Addressing this issue is the next application of the tool developed during this work that we want to face with. Another application of the developed code will be the study of the dark matter dominated dwarf spheroidals.

Chapter 2

Dynamics of axysimmetric collisionless systems

In order to get a deeper insight in the astrophysical problems outlined in Chapter 1, an overview of methods and problems of the *Stellar Dynamics* of the early-type galaxies is required. The main task of Stellar Dynamics is to obtain a *qualitative* understanding of the structure and the evolution of stellar systems (e.g., open and globular clusters, galaxies, clusters of galaxies) and to develop mathematical methods (both *analytical* and *numerical*) able of *quantitative* predictions. Stellar Dynamics deals with gravitational systems made of a large number of "particles" (known as N-body systems), and it has very strong connections with Analytical Mechanics, Statistical Mechanics, Fluid Dynamics, and Plasma Physics, and it also shares with these disciplines many mathematical techniques and results. However, as it is well known, the N-body problem when $N \geq 3$ *cannot* be solved exactly starting from its differential equations and initial conditions, so that alternative approaches are necessary. It should be clear that these alternative approaches are *not* incorrect, but, rather, they make some *additional assumptions* in order to obtain the problem solution. In Section 2.1 a brief overview of the theoretical problem and of the additional assumptions required by these approaches is given. In Section 2.2 and Section 2.3 the Jeans equations and the projected dynamics derivation for the special case of an axisymmetrical, two-integrals model are outlined.

2.1 Theoretical background

Systems made of a large number of “particles” that evolve under the mutual gravitational interaction, are generally called N-body systems, and the equations of motion for each of the N particles (expressed in a Cartesian inertial frame of reference S_0) are given in the Newtonian formulation by:

$$\dot{\mathbf{x}}_i = \mathbf{v}_i \, , \tag{2.1a}$$

$$\dot{\mathbf{v}}_i = -\frac{1}{m_i}\frac{\partial U}{\partial \mathbf{x}_i} \qquad \text{for } i = 1, \ldots, N \, , \tag{2.1b}$$

$$U = -\frac{G}{2}\sum_{\substack{i,j=1\\ i\neq j}}^{N} \frac{m_i m_j}{\|\mathbf{x}_i - \mathbf{x}_j\|} \, , \tag{2.1c}$$

where m_i, $\mathbf{x}_i$, and $\mathbf{v}_i$ are mass, position, and velocity of the i-th star, U is the potential energy, $\partial U/\partial \mathbf{x}_i$ is the gradient of U with respect to $\mathbf{x}_i$, and finally $\|\mathbf{x}\| \equiv \sqrt{x_1^2 + x_2^2 + x_3^2}$ is the standard Euclidean norm. The constant $G = 6.672 \times 10^{-8}\,\mathrm{cm}^3\,\mathrm{s}^{-2}\,\mathrm{g}^{-1}$ is the universal gravitational constant. The problem is usually formulated with the assignment of the initial conditions:

$$\mathbf{x}_i(0) = \mathbf{x}_i^0 \, , \tag{2.2a}$$

$$\mathbf{v}_i(0) = \mathbf{v}_i^0 \, , \tag{2.2b}$$

for $i = 1, \ldots, N$. It is worth noting that all the phenomena related to other factor than gravitational force, in particular to the presence of interstellar gas and electromagnetic fields, in general are neglected when dealing with “pure” N-body problems. This is the case of elliptical galaxies that are known to be particularly gas-poor, and to have weak magnetic fields.

As it is well known, if $N \geq 3$, the equation (2.1a) and (2.1b) are not solvable in the classical meaning of the word, i.e., the problem cannot be reduced to $6N - 1$ independent integrations. A first alternative approach to the direct integration is to restrict the interest to some *specific properties* of the N-body system, hoping that the related evolutionary differential equations are easier to investigate. Borrowing concepts and techniques from Statistical Mechanics, the problem can be tackled using the Liouville theory. Unfortunately, this methods does not lead to any advantage in the aim of finding a solution, because, despite its statistical nature, it is equivalent, in terms of complexity, to the direct solution of the original problem. While the statistical approach can be considered a good starting point, it is clear that further assumptions on the behavior of the N-body systems are required, and it is necessary to move from an exact *theory* to *modeling*.

To this purpose it is important to note that in a N-body system, composed by a large number of "particles", where the only acting force is the gravitational force, the *direct interaction* between two particles can be considered *negligible* over a certain time-scale, usually called *two-body relaxation time* ($\tau_{\rm 2b}$). This fact is due to the long-range nature of the gravitational force, and following semi-quantitative arguments, it can be proved that:

$$\tau_{\rm 2b} \sim \frac{N}{\ln N}\,\tau_{\rm cross}\,, \tag{2.3}$$

where $\tau_{\rm cross}$ is the characteristic time-scale over which a system particle "cross" the system itself (see Binney & Tremaine 1987; Ciotti 2000). It easy to show that when systems composed of a large number of "particles" are considered, $\tau_{\rm 2b}$ largely exceeds the Hubble time. For example in the case of elliptical galaxies, that are the matter of the present work, $N \sim 10^{11}$ and $\tau_{\rm cross} \sim 2 \times 10^8$ yrs, ending with a $\tau_{\rm 2b} \sim 10^{6\div7}$ Gyrs, that is many orders of magnitude longer than the Hubble time.

The previous result states that over the time-scale of the life of the Universe the two-body interactions in galaxies can be neglected and early-type galaxies can be treated as *collisionless* systems. This assumption simplifies the original N-body problem, and make it possible to replace the *discrete* and *discontinuous* distribution of N mass particles with a *smooth* and *continuous* density distribution $\rho(\mathbf{x};t)$, that can be taken as a satisfactory description of the true "granular" N-body system, and serves as a *continuous model* for the original problem. Modeling the N-body system with a continuous density distribution leads to the consequence that the original $6N$-dimensional problem has been reduced to the study of the motion of a *single* particle in the usual 6-dimensional phase-space, simplifying enormously the task of its solution.

This new problem is characterized by the so-called *distribution function* (DF) $f(\mathbf{x},\mathbf{v};t)$, which is nowhere negative, and that is defined by the property that

$$M(\Delta\mathbf{x}\Delta\mathbf{v};t) \equiv \int_{\Delta\mathbf{x}\Delta\mathbf{v}} f(\mathbf{x},\mathbf{v};t)\, d^3\mathbf{x} d^3\mathbf{v}\,, \tag{2.4}$$

where $M(\Delta\mathbf{x}\Delta\mathbf{v};t)$ is the total mass contained at time t in the 6-dimensional phase-space volume $\Delta\mathbf{x}\Delta\mathbf{v}$. It is also worth noting that

$$\rho(\mathbf{x};t) = \int f d^3\mathbf{v}\,, \tag{2.5}$$

and that a smooth potential Φ associated with the density distribution is given by solving the Poisson equation:

$$\nabla^2\Phi = 4\pi G\rho\,. \tag{2.6}$$

Equation (2.6) is a key point of the present work. As it will be discussed in Chapter 3, it is an *elliptic partial differential* equation well known in mathematical physics, and its solution it is not trivial for all but the simplest cases (i.e. spherically symmetric). In general a numerical solution is required, and, due to the importance that this equation has in many fields of the Physics, several methods have been developed to accomplish this task. The method we adopted will be outlined in Section 3.1.

Similarly to the Liouville approach, the main goal is now to determine the differential equation in the collisionless regime for the evolution of the distribution function f. It can be proved (e.g., see Binney & Tremaine 1987; Ciotti 2000) that the DF evolves according to the *Collisionless Boltzmann equation* (CBE):

$$\frac{\partial f}{\partial t} + v_i \frac{\partial f}{\partial x_i} - \frac{\partial \Phi_{\mathrm{T}}}{\partial x_i}\frac{\partial f}{\partial v_i} = 0\,, \tag{2.7}$$

where the convention of sum over repeated indices is used, and $\Phi_{\mathrm{T}} = \Phi + \Phi_{\mathrm{ext}}$ and Φ_{ext} is an external gravitational potential considered for sake of generality. For example, it could represent the contribution of a dark matter halo to the total galactic gravitational field when one is interested into the dynamics of the stellar galaxy components. In particular circumstances, as for example the case of dwarf galaxies, it is believed that $\Phi_{\rm ext}$ is the main component of the gravitational field. In other cases, $\Phi_{\rm ext}$ could be the gravitational potential of a central black hole.

Here it is important to stress that both the Liouville and the collisionless approach are derived rigorously. Therefore the difference between the two approaches does not deal with the mathematical formulation, but rather with their ability to describe a given physical system. From this point of view, the Liouville approach is the *exact* description of the motion of a general N-body system in a $6N$-dimensional phase-space, and the Boltzmann approach is the *exact* description of the motion of a perfectly *collisionless* system in a 6-dimensional phase-space. The key problem is the use of the Boltzmann approach in the description of *real, collisional* N-body systems.

2.2 The Jeans equations for two-integrals systems

Despite the enormous simplification of the mathematical problem introduced in the previous Section with the collisionless hypothesis, the CBE is still to complex to be solved in the general case. Therefore, various techniques have been developed in order to extract information from it. The most widely used among these techniques is the so-called *method of moments*, whose basic idea is to look for differential equations simpler than equation (2.7), describing the relations between particular functions defined as *moments* of the DF over the velocity space. The first *Jeans (or moment) equation* is simply obtained by integrating equation (2.7) over all possible velocities, while the second is obtained by multiplying CBE by v_j before integrating over velocities (e.g. Binney & Tremaine 1987, and also Ciotti 2000 for a complete treatment of this topic):

$$\frac{\partial \rho}{\partial t} + \frac{\partial \rho \overline{v_i}}{\partial x_i} = 0\,, \tag{2.8a}$$

$$\frac{\partial \overline{v_i}}{\partial t} + \overline{v_j}\frac{\partial \overline{v_i}}{\partial x_j} = -\frac{\partial \Phi_{\rm T}}{\partial x_i} - \frac{1}{\rho}\frac{\partial \rho \sigma^2_{ij}}{\partial x_j} \qquad (i = 1, 2, 3)\,, \tag{2.8b}$$

where again the convention of the sum over repeated indices is used, and $\overline{v_i}$ and σ^2_{ij} are defined as:

$$\overline{v_i}(\mathbf{x};t) \equiv \frac{1}{\rho(\mathbf{x};t)} \int v_i f \, d^3\mathbf{v} \,, \tag{2.9a}$$

$$\sigma^2_{ij}(\mathbf{x};t) \equiv \frac{1}{\rho(\mathbf{x};t)} \int (v_i - \overline{v_i})(v_j - \overline{v_j}) f \, d^3\mathbf{v} \,. \tag{2.9b}$$

From a physical point of view $\overline{v_i}$ can be interpreted as the mean value of v_i over all velocities of particles that at time t determine the density ρ at $\mathbf{x}$: in this context, f is the *probability density* used as weight function. From now on, the *bar symbol* ($^-$) over the velocity components will indicate this mean value. In a similar way σ^2_{ij} can be interpreted as the components of a *symmetric tensor* $\boldsymbol{\sigma}$ that measures the velocity dispersion of the system weighted over the DF. It is easy to prove that:

$$\sigma^2_{ij} = \overline{v_i v_j} - \overline{v_i}\,\overline{v_j} \,, \qquad (i,j = 1,2,3) \tag{2.10}$$

where the contribution from the streaming motion $\overline{v_i}\,\overline{v_j}$ is manifest.

Equations (2.8a) and (2.8b) apparently resemble the *continuity* and the *Euler* equations of Fluid Dynamics in the presence of a gravitational field, viscosity, without source terms, and where the pressure force $-\nabla p$ is the analogous of last term on the right side of equation (2.8b). Despite this striking similarity, a fundamental difference between fluids and stellar system must be stressed. The equations of Fluid Dynamics are a *closed* set of equations because the pressure p is related to ρ through the *equation of state*, while in collisionless systems a similar relation among the velocity dispersion σ^2_{ij}, and the density distribution ρ *cannot* be introduced from basic physical arguments. This means that multiplying the CBE by $v_j v_k$, $v_j v_k v_l$, $\ldots$, and integrating over velocities, an *infinite* set of equations of increasingly higher order is obtained. Thus, in order to solve equations (2.8a) and (2.8b) it is necessary to assume a more or less arbitrary *closure relation.* This is often done by specifying the properties of the velocity dispersion tensor or, equivalently, by assuming a specific form for the DF.

In all the present work we will assume that the collisionless system under consideration is *stationary* and *axisymmetric.* From a physical point of view, the assumption of stationarity is justified by the fact that most of the stellar systems, such as ellipticals here considered, show a regular morphology, smooth surface brightness distribution, and (relatively) simple stellar kinematics, suggesting that these objects are in a stationary (or quasi-stationary) state. Moreover, it can be proved, that, under the stationary hypothesis, the DF depends only on the *integrals of motion* of the total potential Φ_{T}. In the case of an axisymmetric system, as those here adopted, these classical integrals of motion are the energy E and the axial component of the angular momentum L_z of each stellar orbit, so that the functional dependences of the DF becomes $f = f(E, L_z)$. Furthermore the natural system of coordinates for such a model is the *cylindrical system of coordinates* (R, φ, z). These coordinates are related to the natural Cartesian coordinate system by the relations $R = \sqrt{x_1^2 + x_2^2}$, $\cos\varphi = x_1/R$, $\sin\varphi = x_2/R$, $z = x_3$, while the velocity vector components are $v_R = \dot{R}$, $v_\varphi = R\,\dot{\varphi}$, $v_z = \dot{z}$. It is easy to show that in cylindrical coordinates the velocity dispersion tensor $\boldsymbol{\sigma}$, for a DF $f(E, L_z)$, is *diagonal*, i.e. $\sigma_{ij} \equiv 0$ if $i \neq j$. Furthermore, as a consequence of the assumed hypothesis, it can be proved that the components of the velocity dispersion tensor and the components of the mean velocity have the following properties:

$$\sigma_R = \sigma_z \,, \tag{2.11a}$$

$$\overline{v_R} = \overline{v_z} = 0 \,, \tag{2.11b}$$

where the diagonal components of the velocity dispersion tensor $(\sigma_R, \sigma_\varphi, \sigma_z)$ are written with a single index for simplicity of notation. With all the assumptions and partial results stated above, the relevant Jeans equations can be rewritten as:

$$\frac{\partial \rho \sigma_R^2}{\partial z} = -\rho \frac{\partial \Phi_{\mathrm{T}}}{\partial z} \,, \tag{2.12a}$$

$$\frac{\partial \rho \sigma_R^2}{\partial R} - \frac{\rho(\overline{v_\varphi^2} - \sigma_R^2)}{R} = -\rho \frac{\partial \Phi_{\mathrm{T}}}{\partial R} \,, \tag{2.12b}$$

where the third equation in the φ coordinate is identically zero because the symmetry of the system. *Equations* (2.12a)*, and* (2.12b) *are the second key* *equations of the present work.* Their solution, again by means of numerical methods, provide the required insight in the intrinsic dynamics of the collisionless model. An outline of how the numerical solution is achieved will be given in Section 3.2.

A careful discussion of the boundary condition for the velocity dispersion is needed. If the system has *infinite extent*, then the natural boundary condition is $\rho\sigma_R^2 \to 0$ for $\|\mathbf{x}\| \to \infty$. Otherwise, if the system is *truncated*, it is required that everywhere on the system boundary the *normal* component of the velocity dispersion σ_n vanishes. It can be proved that the above condition is verified *if and only if* $\sigma_R(= \sigma_z) = 0$ on the boundary surface. Given this boundary conditions the formal solution of equations (2.12a) and (2.12b) is obtained by direct integration. It is worth noting that equation (2.12b) gives $\overline{v_\varphi^2}$, and in order to split it into the streaming motion $\overline{v_\varphi}$, and the azimuthal dispersion, $\sigma_\varphi^2 \equiv \overline{(v_\varphi - \overline{v_\varphi})^2}$, some parametrization must be adopted. We choose the Satoh (1980) decomposition, as it will be explained in the Section 3.2.

2.3 Projected dynamics

When observed, astronomical objects (such as elliptical galaxies) and all their dynamical properties appear projected on the plane of the sky. As a consequence, it is important to set the framework for a correct understanding of the relation between *intrinsic* and *projected* dynamics.

In the general case the intrinsic dynamics of a collisionless stellar system is described in a Cartesian inertial frame of reference S_0, with coordinates (x_1, x_2, x_3), while its projected properties are expressed in the observer's frame of reference S', with coordinates (x'_1, x'_2, x'_3), where the *line of sight* (l.o.s.) is chosen to be directed along x'_3. With this choice the plane of the sky is defined as $\pi' = (x'_1, x'_2)$, the l.o.s. direction is defined as $\mathbf{n} \perp \pi'$, and the two different frame of reference are related by a generic rotation matrix $\mathcal{R}(\phi, \theta, \psi)$, so that:

$$\mathbf{x}' = \mathcal{R}\,\mathbf{x} \tag{2.13a}$$

$$\mathbf{v}' = \mathcal{R}\,\mathbf{v}\,. \tag{2.13b}$$

Any dynamic property of the collisionless system can be re-expressed in the new frame of reference S', and then *projected* onto the plane of the sky by integrating along the line of sight its component on $\mathbf{n}$. It easy to show that the *streaming velocity field* and velocity dispersion tensor along the l.o.s. direction are:

$$\begin{aligned}\overline{v_n} &\equiv \overline{v_i\, n_i} \\ &= \overline{v_i}\, n_i\,,\end{aligned} \tag{2.14a}$$

$$\begin{aligned}\sigma_n^2 &\equiv \overline{(v_i\, n_i - \overline{v_i\, n_i})(v_j\, n_j - \overline{v_j\, n_j})} \\ &= \overline{(v_i n_i - \overline{v_n})(v_j n_j - \overline{v_n})} \\ &= \sigma_{ij}^2\, n_i n_j\,,\end{aligned} \tag{2.14b}$$

where again the repeated index convention is assumed. The corresponding projected quantities are obtained by switching to the S' frame reference and integrating over x'_3:

$$\Sigma(x'_1, x'_2)\, \overline{v_p}(x'_1, x'_2) \equiv \int_{-\infty}^{\infty} \rho(\mathbf{x}')\, \overline{v_n}(\mathbf{x}')\, dx'_3\,, \tag{2.15a}$$

$$\Sigma(x'_1, x'_2)\, \overline{V_p}^2(x'_1, x'_2) \equiv \int_{-\infty}^{\infty} \rho(\mathbf{x}')\, \overline{v_n}^2(\mathbf{x}')\, dx'_3\,, \tag{2.15b}$$

and

$$\Sigma(x'_1, x'_2)\, \sigma_p^2(x'_1, x'_2) \equiv \int_{-\infty}^{\infty} \rho(\mathbf{x}')\, \sigma_n^2(\mathbf{x}')\, dx'_3\,, \tag{2.15c}$$

where

$$\Sigma(x'_1, x'_2) \equiv \int_{-\infty}^{\infty} \rho(\mathbf{x}')\, dx'_3\,. \tag{2.15d}$$

In general, when observing a given system, σ_p^2 does not coincide with the *observed* l.o.s. velocity dispersion. In fact, the observations give the l.o.s. velocity dispersion with respect to the observed l.o.s. streaming velocity field

$\overline{v_p}$, while σ_p^2 is defined with respect to $\overline{v_n}$, see Equation (2.14b). To circumvent this problem the correct definition for the l.o.s. velocity dispersion is:

$$\Sigma(x_1', x_2')\, {\sigma^2}_{\rm los}(x_1', x_2') \equiv \int_{-\infty}^{\infty} \rho(\mathbf{x}')\, \overline{\left(v_n - \overline{v_p}\right)^2}\, dx_3' \,, \tag{2.16}$$

that can be expressed in terms of σ_p^2, $\overline{v_p}$, and $\overline{V_p}^2$ (see Ciotti 2000, for a complete derivation):

$${\sigma^2}_{\rm los} = \sigma_p^2 + \overline{V_p}^2 - \left(\overline{v_p}\right)^2 . \tag{2.17}$$

Note that, even in a system with no intrinsic velocity dispersion (i.e. $\sigma_p^2 = 0$), ${\sigma^2}_{\rm los}$ can be greater than zero, because the contribution of the l.o.s. velocity fields $\overline{V_p}^2$, and $\left(\overline{v_p}\right)^2$. Since the observed velocity dispersion is always measured within a given aperture, a velocity dispersion within a given aperture $\sigma_{\rm ap}^2$ is also defined:

$$M(R)\, \sigma_{\rm ap}^2(R) \equiv \int_{R \leq \sqrt{x_1'^2 + x_2'^2}} \Sigma(x_1', x_2')\, {\sigma^2}_{\rm los}(x_1', x_2')\, dx_1' dx_2' \,, \tag{2.18}$$

where $M(R)$ is the mass inside the given aperture of radius R.

In the present work, we have made the assumption that the collisionless systems considered are *axisymmetric*. In this case it can be easily showed that the generic rotation matrix $\mathcal{R}(\phi, \theta, \psi)$, introduced at the beginning of this section, can be reduced to a simple rotation matrix $\mathcal{R}(\theta)$ around the $x_1 \equiv x_1'$ axis:

$$\mathcal{R}(\theta) = \begin{pmatrix} 1 & 0 & 0 \\ 0 & \cos\theta & -\sin\theta \\ 0 & \sin\theta & \cos\theta \end{pmatrix} , \tag{2.19}$$

where $0 \leq \theta \leq \pi/2$, so that $\theta = 0$ corresponds to the face-on view of the system, while $\theta = \pi/2$ to the edge-on view, as shown in Figure 2.1. Given the above relation between the frames of reference S_0 and S', it is

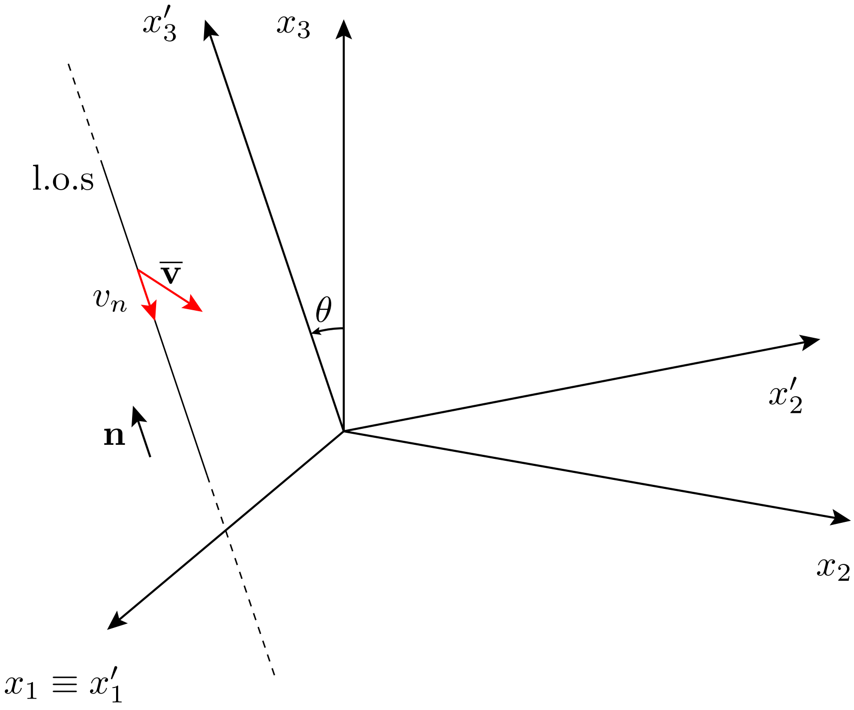

Figure 2.1 – The shape and the projected dynamics of an axisymmetric galaxy model change depending on the observation direction (l.o.s.). The natural systems of coordinates (x_1, x_2, x_3), and the observer systems coordinates (x'_1, x'_2, x'_3), are tilted around $x_1 \equiv x'_1$ axis, of an angle θ. The line of sight versor $\mathbf{n}$ is directed along the x'_3 axis toward the observer.

easy to show that the l.o.s. direction is $\mathbf{n} = (0, -\sin\theta, \cos\theta)$. Moreover an explicit expression for v_p and σ_p^2 can be retrieved. The relation that transforms velocities from the cylindrical coordinates (R, φ, z), where the Jeans equations are solved, to the natural Cartesian coordinates (x_1, x_2, x_3), in which the projection has been developed, are:

$$\overline{v_1} = \overline{v_R} \cos\varphi - \overline{v_\varphi} \sin\varphi \,, \tag{2.20a}$$

$$\overline{v_2} = \overline{v_R} \sin\varphi + \overline{v_\varphi} \cos\varphi \,, \tag{2.20b}$$

$$\overline{v_3} = \overline{v_z} \,, \tag{2.20c}$$

and using equations (2.11b) the expressions above become:

$$\overline{v_1} = -\,\overline{v_\varphi} \sin\varphi \,, \tag{2.21a}$$

$$\overline{v_2} = \overline{v_\varphi} \cos\varphi \,, \tag{2.21b}$$

$$\overline{v_3} = 0 \,. \tag{2.21c}$$

In a similar manner explicit expression for the component of the velocity dispersion tensor can be derived:

$$\sigma_{11}^2 = \sigma_R^2 \cos^2\varphi + \sigma_\varphi^2 \sin^2\varphi \,, \tag{2.22a}$$

$$\sigma_{22}^2 = \sigma_R^2 \sin^2\varphi + \sigma_\varphi^2 \cos^2\varphi \,, \tag{2.22b}$$

$$\sigma_{33}^2 = \sigma_R^2 \,, \tag{2.22c}$$

$$\sigma_{12}^2 = \left(\sigma_R^2 - \sigma_\varphi^2\right) \sin\varphi \cos\varphi \,, \tag{2.22d}$$

$$\sigma_{13}^2 = \sigma_{23}^2 = 0 \,, \tag{2.22e}$$

and thus explicit expressions for equations (2.14a), and (2.14b) can be written as:

$$\overline{v_p} = -\,\overline{v_\varphi}\cos\varphi\sin\theta\,, \tag{2.23a}$$

$$\sigma_p^2 = \sigma_R^2\cos^2\theta + \left(\sigma_R^2\cos^2\varphi + \sigma_\varphi^2\sin^2\varphi\right)\sin^2\theta\,. \tag{2.23b}$$

With these results the *intrinsic dynamics* obtained solving Jeans equations (2.12a), and (2.12b) can be put in direct relation with the *observed dynamics* through equation (2.15a), (2.15b), (2.15c), and (2.17) to get some insight in it. In the following Chapter it will be shown how the theoretical apparatus developed so far, has be implemented in our original numerical code in order to study such collisionless axisymmetric models.

Chapter 3

The numerical code

When dealing with dynamical collisionless galaxy models, as those described in Chapter 2, the first problem is to find a density-potential pair that can resemble as much as possible a *real* galaxy. Usually a given spatial density distribution ρ is assumed to be a good description of the system and then its gravitational potential Φ is reconstructed by solving the Poisson equation. Nevertheless density-potential pairs known analytically are limited to a few trivial cases (most of the times spherically symmetric), while, when more realistic density distribution are considered, the only way to obtain the corresponding gravitational potential Φ is to adopt a numerical approach. The same approach is thus adopted for the solution of the Jeans equations and for the projected dynamics. In the present chapter our numerical code and the numerical methods implemented in it are described and discussed. In Section 3.1 the symmetries of the problem and the solution of the Poisson equation is described, while in Section 3.2 the solution Jeans equations is discussed. The last Section describe the implementation of the projection of the intrinsic model dynamics. The flow chart of our code and the relevant routines are given in Appendix C, while the full code is freely distributed upon request.

3.1 Solving the Poisson equation

As already noted in Chapter 2, our models are axisymmetric, and are supposed to be supported by a dynamics described by a two-integrals distribution function (DF) $f = f(E, L_z)$ (where E and L_z are the energy and the z-component of the angular momentum of stars). With these assumptions, the Poisson and Jeans equations are better solved in spherical (r, ϑ, φ) or cylindrical (R, φ, z) coordinates, since their dependences on the coordinate φ vanishes and the original problem reduces from 3-dimensional to 2-dimensional. In particular, the Jeans equations take a very simple form if solved in cylindrical coordinates, while it turns out that, for the solution of the Poisson equation the spherical coordinates better deserves our numerical method as explained in the following. A further symmetry with respect to the equatorial plane of the model has been assumed, so that we can restrict our simulation to the $(r > 0, 0 < \vartheta < \pi/2)$ quadrant if working in spherical coordinates, and to the $(R > 0, z > 0)$ quadrant if working in cylindrical coordinates. While the latter symmetry assumption is not strictly required by potential theory (e.g. Tassoul 1978), it can be considered absolutely acceptable, and its assumption make the numerical solution faster.

Given a spatial density distribution ρ for a galaxy model the first step in order to reconstruct its dynamics is to calculate the gravitational potential Φ generated by the density distribution itself. The gravitational potential and the density distribution are related by the well known Poisson equation:

$$\nabla^2 \Phi = 4\pi G \rho \, . \tag{3.1}$$

This equation belongs to the family of the elliptic partial differential equations (PDE), well studied in mathematical physics (e.g. Arfken & Weber 2000; Courant & Hilbert 1953; Morse & Feshbach 1953), whose numerical solution can be performed by several different mathematical methods all well studied in literature. In the present work we have chosen to solve it by means of the so-called “spectral methods” (e.g. Gottlieb & Orszag 1977; Canuto et al. 1987). They consists in expanding both the gravitational potential Φ and the density distribution ρ in series of some orthogonal sets of functions. If these sets of functions are chosen to be eigenfunctions of the Laplace operator ∇^2 in the given system of coordinates, the original differential problem becomes an algebraic problem, easily solvable with a numerical code.

Adapting the method from Londrillo & Messina (1990), to the symmetry of our models, we adopt the spherical system of coordinates (r, ϑ, φ) in which the Laplace operator (∇^2) can be written as:

$$\nabla^2 \equiv \frac{1}{r^2}\left(\mathcal{L}_r + \mathcal{L}_\vartheta + \mathcal{L}_\varphi\right) \tag{3.2a}$$

and:

$$\mathcal{L}_r \equiv r\frac{\partial}{\partial r}r\frac{\partial}{\partial r} + r\frac{\partial}{\partial r}\,, \tag{3.2b}$$

$$\mathcal{L}_\vartheta \equiv \frac{1}{\sin\vartheta}\frac{\partial}{\partial\vartheta}\sin\vartheta\frac{\partial}{\partial\vartheta}\,, \tag{3.2c}$$

$$\mathcal{L}_\varphi \equiv \frac{1}{\sin^2\vartheta}\frac{\partial^2}{\partial\varphi^2}\,. \tag{3.2d}$$

Note that the $\mathcal{L}_\varphi$ operator can be omitted from equation (3.1), because our models are assumed to be axysimmetric, so that the Poisson equation becomes:

$$\left(\mathcal{L}_r + \mathcal{L}_\vartheta\right)\Phi(r,\vartheta) = \varrho(r,\vartheta) \tag{3.3}$$

where:

$$\varrho \equiv 4\pi G r^2 \rho\,. \tag{3.4}$$

It can be easily shown (see Abramowitz & Stegun 1972, §8.1) that Legendre polynomials of the first kind $P_l(\cos\vartheta)$ are eigenfunctions for the operator $\mathcal{L}_\vartheta$, so that:

$$\mathcal{L}_\vartheta P_l(\cos\vartheta) = -l(l+1)P_l(\cos\vartheta)\,. \tag{3.5}$$

Hence using a Legendre polynomials series truncated to the order $l_{\max}$, the angular part of ϱ and Φ can be expanded as:

$$\varrho(r,\vartheta) = \sum_{l=0}^{l_{\max}} \varrho_l(r) P_l(\cos\vartheta) \tag{3.6a}$$

$$\Phi(r,\vartheta) = \sum_{l=0}^{l_{\max}} \Phi_l(r) P_l(\cos\vartheta)\,, \tag{3.6b}$$

and, using the orthogonality properties of the Legendre polynomials (see Abramowitz & Stegun 1972, §22.1-22.2), the Equation (3.3) becomes a set of $l_{\max}$ differential equations in the r variable:

$$\Big[\mathcal{L}_r - l(l+1)\Big]\Phi_l(r) = \varrho_l(r) \qquad\qquad 0 \le l \le l_{\max}\,, \tag{3.7}$$

where $\varrho_l(r)$ and $\Phi_l(r)$ are defined as:

$$\varrho_l(r) \equiv \frac{2l+1}{2}\int_0^{\pi} \varrho(r,\vartheta) P_l(\cos\vartheta)\sin\vartheta\, d\vartheta \tag{3.8a}$$

$$\Phi_l(r) \equiv \frac{2l+1}{2}\int_0^{\pi} \Phi(r,\vartheta) P_l(\cos\vartheta)\sin\vartheta\, d\vartheta\,. \tag{3.8b}$$

Each of the Equations (3.7) can be further transformed if we find a set of orthonormal function to expand the radial part of each of the $\varrho_l(r)$ and $\Phi_l(r)$. This task is made easier if we choose to re-map the unbounded variable r into an angular interval u by:

$$r = \tan^2(u/2) \qquad\qquad 0 \le r < \infty\,,\ 0 \le u \le \pi\,, \tag{3.9}$$

and with this change of variable, the $\mathcal{L}_r$ operator becomes:

$$\mathcal{L}_r \equiv \mathcal{L}_u = \frac{1}{4}\sin u \frac{\partial}{\partial u}\sin u \frac{\partial}{\partial u} + \frac{1}{2}\sin u \frac{\partial}{\partial u}\,. \tag{3.10}$$

We can rewrite $\varrho_l(r)$ and $\Phi_l(r)$ using the new coordinate u, and expand them in a series of the Chebyshev polynomials $T_n(\cos u)$ (see Abramowitz

& Stegun 1972, Chapter 22) truncated to the $n_{\max}$ order, so that:

$$\varrho_l(u) = \varrho_{0l} + 2\sum_{n=1}^{n_{\max}} \varrho_{nl}\, T_n(\cos u) \tag{3.11a}$$

$$\Phi_l(u) = \Phi_{0l} + 2\sum_{n=1}^{n_{\max}} \Phi_{nl}\, T_n(\cos u)\,. \tag{3.11b}$$

where:

$$\varrho_{nl} = \frac{1}{\pi}\int_0^\pi \varrho_l(u) T_n(\cos u)\, du \tag{3.12a}$$

$$\Phi_{nl} = \frac{1}{\pi}\int_0^\pi \Phi_l(u) T_n(\cos u)\, du \tag{3.12b}$$

It can be easily shown that Chebyshev polynomials are *not* eigenfunctions of the $\mathcal{L}_u$ operator, in fact:

$$\mathcal{L}_u T_n(\cos u) = \sum_{k=n-2}^{n+2} a_k T_k(\cos u) \tag{3.13}$$

so that the operator loses its self-adjoint character. This implies that, using the properties and orthogonality of these polynomials, the differential equation (3.7) does not become a simple algebraic equation as in the Legendre expansion, but it can be written as a set of *matrix* equations:

$$[\mathsf{A} - l(l+1)\mathsf{I}]\, \boldsymbol{\Phi}_l = \boldsymbol{\varrho}_l \qquad 0 \le l \le l_{\max} \tag{3.14}$$

where A is a penta-diagonal matrix resulting from the Chebyshev expansion, and I is an identity matrix, both of order $n_{\max}$, while $\boldsymbol{\Phi}_l$ and $\boldsymbol{\varrho}_l$ are two vectors with $n_{\max}$ dimension, and with components Φ_{nl} and ϱ_{nl}, respectively. Solving such an equation is computationally more complex than solving a simple algebraic equation, nevertheless the intrinsic resolution power of the Chebyshev polynomials is worth to be implemented. Furthermore, being the resulting matrix penta-diagonal, the computational effort required to invert it is just $\sim O(n_{\max})$, making this extra-cost affordable.

For $l \neq 0$ the linear problem of Equation (3.14), given the vectors $\boldsymbol{\varrho}_l$ and the matrix A, can be easily solved for $\boldsymbol{\Phi}_l$ by means of standard matrix inversion techniques. However, when $l = 0$, the linear problem is *singular* and a further condition is required to recover the missing spectral coefficient Φ_{00}, and to solve Equation (3.14). Setting to zero the potential at infinity ($\Phi \xrightarrow{u \to \pi} 0$) provides the required boundary condition, that in terms of the spectral components corresponds to the relation:

$$\Phi_{00} + 2 \left(\sum_{n=\mathrm{even}} - \sum_{n=\mathrm{odd}} \right) \Phi_{n0} = 0\,, \tag{3.15}$$

from which the missing spectral coefficient Φ_{00} can be calculated. Once all the vectors $\boldsymbol{\Phi}_l$ are known, the gravitational potential Φ, and its gradient $\nabla\Phi$ can be directly calculated in cylindrical coordinates (R, z).

Implementing this algorithm, we have adopted two uniform Chebyshev-Gauss grids in the variable u and ϑ, so that all the integration involved can be performed by means of the Gauss integration method (see Press et al. 1992, §4.5). Furthermore, given the mapping function (3.9), a uniform distribution of nodes for the u-grid corresponds to a not-uniform sampling of the radial domain r, with a coarse sampling for the outer regions and high resolution sampling for the central regions, particularly suited for our cuspy models. The grids for the cylindrical coordinates, over which both the gravitational potential and its gradient are calculated, are build in a similar way, as explained in the following section.

3.2 Solving the Jeans equations

As already shown in Section 2.2, the DF of an axysimmetric collisionless model depends only from energy and the z-component of the angular momentum of stars $f(E, L_z)$, and the Jeans equations, when written in cylindrical coordinates (R, φ, z), assume the simple form:

$$\frac{\partial \rho \sigma_R^2}{\partial z} = -\rho \frac{\partial \Phi_{\mathrm{T}}}{\partial z}, \tag{3.16a}$$

$$\frac{\partial \rho \sigma_R^2}{\partial R} - \frac{\rho(\overline{v_\varphi^2} - \sigma_R^2)}{R} = -\rho \frac{\partial \Phi_{\mathrm{T}}}{\partial R}\,. \tag{3.16b}$$

These equations can be easily solved by direct integration, giving σ_R^2 and $\overline{v_\varphi^2}$. To split the latter into streaming motion $\overline{v_\varphi}$, and azimuthal dispersion, $\sigma_\varphi^2 \equiv \overline{(v_\varphi - \overline{v_\varphi})^2}$, we adopt the Satoh (1980) k-decomposition:

$$\overline{v_\varphi}^2 = k^2(\overline{v_\varphi^2} - \sigma_R^2) \tag{3.17a}$$

$$\sigma_\varphi^2 = \sigma_R^2 + \left(1 - k^2\right)\left(\overline{v_\varphi^2} - \sigma_R^2\right), \tag{3.17b}$$

with $0 \leq k \leq 1$. For $k = 0$ no ordered motions are present, and the velocity dispersion tensor is maximally tangentially anisotropic, while for $k = 1$ the velocity dispersion tensor is isotropic, and the galaxy flattening is due to azimuthal streaming velocity (such a model is the so called *isotropic rotator*). In principle, by relaxing the hypothesis of a constant k and allowing for $k = k(R, z)$, even more rotationally supported models can be constructed, up to the *maximum rotation* case considered in Ciotti & Pellegrini (1996), where $k(R, z)$ is defined so that $\sigma_\varphi^2 = 0$ everywhere.

The integration of equations (3.16a) and (3.16b) are performed over two grids for the cylindrical coordinate, using a standard cubic spline algorithm. The grids are built remapping the unbound variables R and z into two angular interval using the following relations:

$$R = \tan(v/2) \qquad 0 \leq R < \infty\ ,\ 0 \leq v \leq \pi \tag{3.18a}$$

$$z = \tan(w/2) \qquad 0 \leq z < \infty\ ,\ 0 \leq w \leq \pi\ , \tag{3.18b}$$

and adopting uniform Chebyshev-Gauss grids for the variables v and w. In this way, as already stated in Section 3.1, the central regions of the model are sampled at high resolution, as requested by the density cusp and by the possible presence of a central super-massive black hole.

3.3 Projected dynamics

Once the intrinsic dynamics has been derived from Jeans equations, the projected dynamics can be deduced as already explained in Section 2.3. The general framework for the projection of the model properties is given there. Here we recall that to perform projections on the plane of the sky (the projection plane), we assume a Cartesian coordinate system (x'_1, x'_2, x'_3), with the line of sight (*l.o.s.*) directed along the x'_3 axis, and with the x'_1 axis coincident with the x_1 axis of the natural Cartesian system introduced at the beginning of Section 2.3. The angle between x_3 and x'_3 is θ, with $0 \leq \theta \leq \pi/2$: thus $\theta = 0$ corresponds to the face-on view of the galaxy, while $\theta = \pi/2$ to the edge-on view, as showed in Figure 2.1 in the previous Chapter. With this choice, the projection plane is (x'_1, x'_2), and the l.o.s. direction in the natural coordinate system is given by $\mathbf{n} = (0, -\sin\theta, \cos\theta)$[1]. Each of the two systems of coordinates (the natural and the l.o.s. ones) are represented in our numerical implementation by two 2-dimensional grids. Because of the rotation between the two systems of coordinates, the grids are not aligned in general, so that an interpolation for all the quantities of interest is required before performing the projection operation along the l.o.s. direction. The process of interpolation can be intensive, especially when adequate grids are considered, for these reason a *bilinear* interpolation algorithm has been adopted (see Press et al. 1992, §3.6). This kind of interpolation algorithm has a computational cost that does not dominate the simulation execution time when the grids have a large enough number of points, furthermore, it has been tested against higher-order algorithms, such as the cubic-spline interpolation (see Stoer & Bulirsch 1980, §2.4), and it has showed comparable results for our simulated models. After the interpolation phase, the integration along the l.o.s. (i.e. over x'_3) for all the projected dynamical fields of interest (i.e. Σ, $\overline{v_p}$, $\overline{V_p}^2$, σ^2_p, $\sigma^2{}_{\rm los}$, and $\sigma^2_{\rm ap}$) are computed using a cubic-spline algorithm. Due to the symmetry of the considered models, such an integration can be restricted to the two octants $(x'_1 > 0, x'_2 > 0, -\infty < x'_3 < \infty)$, so that all the projected quantities can be given only onto the $(x'_1 > 0, x'_2 > 0)$ quadrant of the plane of the sky.

3.4 Tests

The code has been tested for its accuracy and precision by checking how precisely it reproduces the results obtained with models whose dynamical

---

[1] The l.o.s.vector points *toward* the observer, and so *positive* velocities correspond to a *blue-shift*.

properties are known analytically. For this purpose we have chosen the (Nagai & Miyamoto 1976, see also Ciotti & Pellegrini 1996) models:

$$\rho(R,z) = \frac{M_*}{4\pi r_c^3} \frac{s\widetilde{R}^2 + (s+3\eta)(s+\eta)^2}{\eta^3 \left[\widetilde{R}^2 + (s+\eta)^2\right]^{5/2}}\,, \tag{3.19a}$$

$$\Phi(R,z) = -\frac{GM_*}{r_c} \frac{1}{\sqrt{\widetilde{R}^2 + (s+\eta)^2}}\,, \tag{3.19b}$$

where $s \geq 0$ is the flattening parameter, $\eta = \sqrt{1 + z^2/r_c^2}$, and $\widetilde{R} = R/r_c$; the spherical γ-models (Dehnen 1993; Tremaine et al. 1994):

$$\rho(r) = \frac{3-\gamma}{4\pi} \frac{M_*\, r_c}{r^\gamma (r + r_c)^{4-\gamma}} \tag{3.20a}$$

$$\Phi(r) = \frac{GM_*}{r_c} \begin{cases} -\dfrac{1}{2-\gamma}\left[1 - \left(\dfrac{r}{r+r_c}\right)^{2-\gamma}\right]\,, & (\gamma \neq 2) \\ \ln \dfrac{r}{r+r_c}\,, & (\gamma = 2)\,, \end{cases} \tag{3.20b}$$

and the so-called Ferrers ellipsoids (Ferrers 1877):

$$\rho(m) = \frac{M_*}{4\pi r_c^3} \begin{cases} (1-m^2)^n & (0 \leq m \leq 1) \\ 0 & (m > 1)\,, \end{cases} \tag{3.21}$$

where $m^2 = R^2/r_c^2 + z^2/(q^2 r_c^2)$, and q is the flattening parameter. These models are all axisymmetric, being the spherical γ-models a special case, and thus well suited to be used as the starting density distribution in our code. Furthermore, for all these models, the dynamical quantities and, to some extent, even the projected fields are known analytically, giving us the chance to test the robustness and correctness of our code. Each of these models has been chosen to test the code in a different manner: the Miyamoto-Nagai models can have an high intrinsic flattening, and thus they have been used to test the code ability to reproduce very flattened models. The spherical

γ-models have a density distribution that diverges in the center as $r^{-\gamma}$, and thus can be used to test the code performance of cuspy models. Finally projected dynamics can be tested using Ferrers ellipsoids whose projected velocity dispersion have been already studied by Lanzoni & Ciotti (2003). It turns out that the accordance between their results and our numerical simulation is excellent, despite the fact that Ferrers models are truncated while our code has been implemented considering density distributions that extends to the infinity. All these comparisons give excellent results, with relative errors $\lesssim 10^{-3}$ for the intrinsic dynamical properties, such as the potential Φ, the velocity dispersion fields σ_R and σ_φ, and $\lesssim 10^{-2}$ for the projected fields, such as the projected velocity v_p and velocity dispersion $\sigma_{\rm los}$. Other more complicate tests have been also performed by comparing the code output with explicit solutions of the Jeans equations obtained from the homeoidal expansion of oblate power law models with dark matter halo and central black hole. In Figure 3.1 are shown the gravitational potential (upper panel) and velocity dispersion (lower panel) for a flattened ($s = 5$) Miyamoto-Nagai model. In Figure 3.2 is represented the gravitational potential for a spherical γ-model with $\gamma = 2$. As can be seen the numerical results ($\triangle$ symbols) are in excellent agreement with the expected results (solid line). To further, test the results for projected quantities we have made use of a general consequence of the projected virial theorem:

$$2n_i n_j K_{ij} = -n_1^2 W_{11}^2 - n_2^2 W_{22}^2 - n_3^2 W_{33}^2 \tag{3.22}$$

with K_{ij} and W_{ij} being the kinetic and potential energy tensor (e.g. Ciotti 2000).

A full description of the code and its implementation is given in Appendix C.

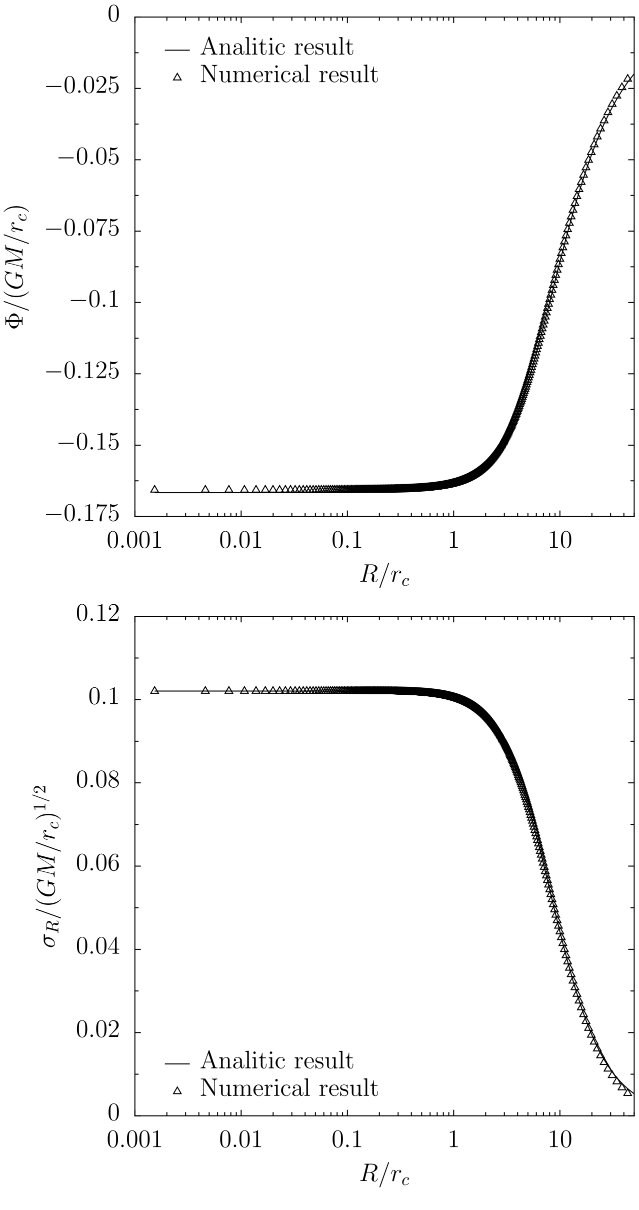

Figure 3.1 – A sample of tests performed using flattened ($s = 5$) Miyamoto-Nagai models; numerical results (triangles) are checked against theoretical formulas (solid lines). The upper panel shows the gravitational potential, while the lower panel shows the velocity dispersion σ_R in the equatorial plane of the test model.

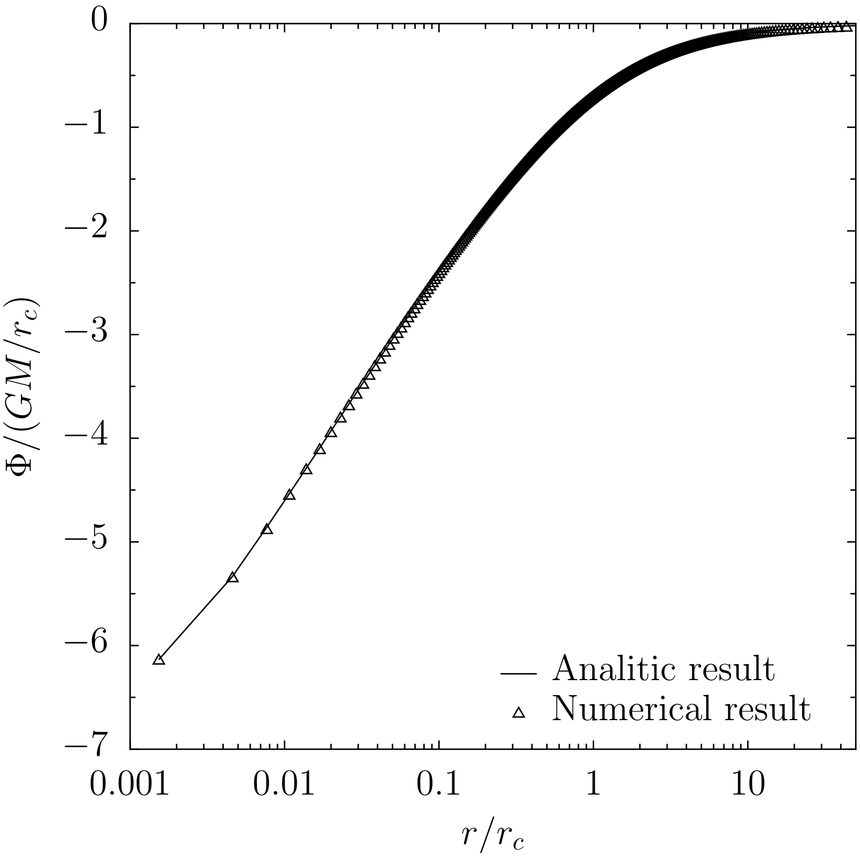

Figure 3.2 – A test performed using spherical cuspy γ-models; numerical results (triangles) are checked against theoretical formulas (solid lines). The gravitational potential for a model with $\gamma = 2$ is shown.

Chapter 4

Galaxy models

The code described in Chapter 3 has be used to determine the gravitational potential, solve the Jeans equations and to compute the projected dynamics for any collisionless system which is axysimmetric and whose dynamics is described by a two-integral distribution function $f(E, L_z)$. Among all possible models whose density distributions and dynamics suite these constraints, we use, in the present work, a family of *oblate* galaxy models with *homeoidal* density distribution, belonging to the so-called γ-models (Dehnen 1993; Tremaine et al. 1994; Qian et al. 1995). We also perform our simulations considering both models with *one* and *two-component*. The one-component models represent the case of galaxies consisting of stars only, while the two-component case corresponds to galaxies with a stellar distribution and a dark matter halo with a possibly different spatial distribution. Moreover, a *central super-massive black hole* can be added to either of these classes of models (Magorrian et al. 1998; Ferrarese & Merritt 2000). In Section 4.1 the one-component models and their generalization from the spherical γ-models to the oblate ones is outlined, while in Section 4.2 the main properties of the two-component models are described. Finally, Section 4.3 briefly shows how a super-massive black hole has been inserted in the simulations.

4.1 One-component models

The spatial density distribution ρ for the *spherically* symmetric γ-model has been first suggested by Dehnen (1993) and Tremaine et al. (1994):

$$\rho(r) = \frac{3-\gamma}{4\pi} \frac{M_* \, r_c}{r^\gamma (r+r_c)^{4-\gamma}} \tag{4.1a}$$

$$M(r) = M_* \left(\frac{r}{r+r_c} \right)^{3-\gamma} , \tag{4.1b}$$

and a simple integration shows that:

$$\Phi(r) = \frac{GM_*}{r_c} \begin{cases} -\dfrac{1}{2-\gamma} \left[1 - \left(\dfrac{r}{r+r_c} \right)^{2-\gamma} \right] , & (\gamma \neq 2) \\ \ln \dfrac{r}{r+r_c} , & (\gamma = 2) \end{cases} \tag{4.1c}$$

where M_* is the total stellar mass of the model, r_c is the scale radius, and $0 \leq \gamma < 3$. Most of the intrinsic and projected dynamics of this family of models can be expressed in terms of elementary functions in some particular cases, and the Hernquist (1990, $\gamma = 1$) and the Jaffe (1983, $\gamma = 2$) models are two special cases of this family. A comparison with the de Vaucouleurs $R^{1/4}$-profile (1948) shows that γ-models are a reasonable approximation for real elliptical galaxies when their density profiles are projected on the plane of the sky.

Unfortunately, early type galaxies are known to be mostly tri-axial and to be characterized by velocity dispersion anisotropy (through the analysis of the v/σ-ϵ plane), so that spherical models cannot be a good description of their dynamics. A first step toward a better representation of the real galaxies consists in considering *oblate axisymmetrical* models, whose density distribution is stratified on *homeoids*. With such a generalization the expression for equation (4.1a) becomes:

$$\rho(m) = \frac{M_* \, (3-\gamma)}{4\pi \, r_c^3 \, q} \frac{1}{m^\gamma \, (1+m)^{4-\gamma}} , \tag{4.2}$$

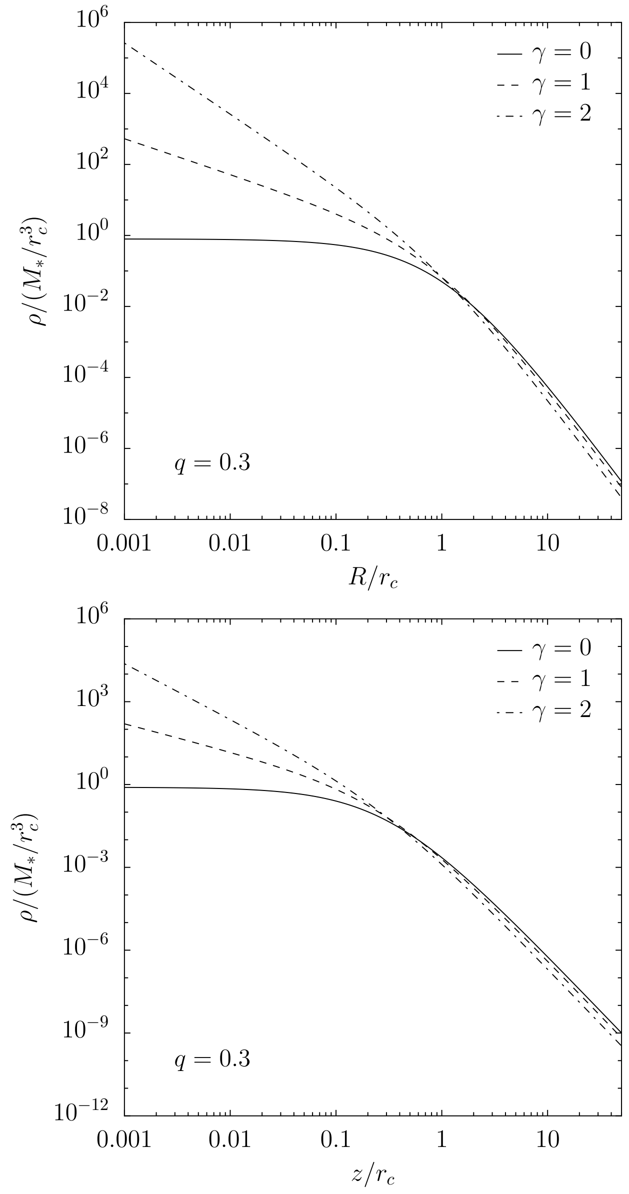

Figure 4.1 – Density distribution for γ-models with different shape and flattening value $q = 0.3$; along the equatorial plane ($z = 0$) in the upper panel, along the symmetry axis ($R = 0$) in the lower panel.

where in cylindrical coordinates[1] (R, φ, z) the isodensity surfaces are labeled by:

$$m^2 \equiv \tilde{R}^2 + \frac{\tilde{z}^2}{q^2}\,, \tag{4.3}$$

with $\tilde{R} \equiv R/r_c$ and $\tilde{z} \equiv z/r_c$, and where the parameter $0 < q \leq 1$ measures the intrinsic model flattening. In order to reduce the dimension of the parameter space, the stellar mass-to-light ratio $\Upsilon \equiv M_*/L$ is assumed to be constant within each model galaxy.

With the assumptions made so far, each model described by equation (4.2) is characterized by the two shape parameters (γ, q). Moreover, as explained in Chapter 3, the Satoh parameter (k), and the line of sight parameter (θ) are required to solve the Jeans equations and to perform the projection operation respectively, so that each of the one-component models described so far are completely defined by *four* parameters (γ, q, k, θ).

In Figure 4.1 the density distribution for models with different values of *gamma*, and flattening parameter $q = 0.3$, are shown. In the right panel the density distribution is plotted along the equatorial plane $(z = 0)$, while the left panel shows the same function along the symmetry axis $(R = 0)$.

4.2 Two-component models

The dark matter (DM) halo of the two-component models is described by a $\rho_h(m)$ profile of the same family of equation (4.2), with mass M_h and scale radius r_h, related to the stellar mass M_* and stellar scale radius r_c by:

$$M_h \equiv \alpha\, M_* \tag{4.4a}$$

$$r_h \equiv \beta\, r_c\,. \tag{4.4b}$$

With this choice each DM component is characterized by the two shape parameter (γ, q), and by the parameter (α, β) introduced above, so that a

---

[1] These coordinates are related to the natural Cartesian coordinate system by the relations $R = \sqrt{x^2 + y^2}$, $\cos\varphi = x/R$, $\sin\varphi = y/R$.

two-component model is defined by a total of *eight* parameters: (γ_*, q_*, γ_h, q_h, k, θ, α, β).

4.3 The central super-massive black hole

In the case a central super-massive black hole (BH) is considered, the total gravitational potential is modified by adding its contribution:

$$\Phi_{\mathrm{BH}}(r) = -\frac{G\,M_{\mathrm{BH}}}{r}\,, \tag{4.5}$$

where M_{BH} is the BH mass, that can be expressed in M_* units defining:

$$M_{\mathrm{BH}} \equiv \mu\, M_*\,. \tag{4.6}$$

Thus, the additional parameter μ is added to one and two-component models when a BH is present. Observations shows that $\mu \simeq 1.3\,10^{-3}$ (Merritt & Ferrarese 2001a; Magorrian et al. 1998).

Finally it is worth noting that all the masses and lengths of the models described in this Chapter have been assumed to be expressed in terms of M_* and r_c respectively. For this reason each model can be considered *scale-free* with respect of these two parameters.

Several quantitative yet analytical properties of these models are reported in Appendix A, where we applied the homeoidal expansion technique discussed by Ciotti & Bertin (2005).

Chapter 5

Results

Although real elliptical galaxies are generally tri-axial, the axisymmetrical models described in Chapter 4 are an acceptable approximation of them, and studying their *intrinsic* and *projected* dynamics is a key point to better understand the astrophysical issues presented in the Chapter 1. Unfortunately, neither the intrinsic dynamic nor the projected dynamic for these models can be solved analytically, and it is here that the code described in Chapter 3, and developed during this work, comes into play. Thanks to its ability to compute the gravitational potential, the intrinsic, and the projected dynamics of the models, it can be used as a tool to investigate the properties of such a family of models. Moreover, the provided results can be used to reach a better insight in galaxy dynamics, and in the astrophysical problems cited in Chapter 1. In Section 5.1 the properties of the adopted family of models are outlined, in Section 5.2 a discussion on the the sphere of influence of the super-massive black hole is provided, in Section 5.3 the contribution of rotation and projection effects to the thickness of the Fundamental-Plane is elucidated, and in Section 5.4 some considerations about the v/σ-ϵ plane are reported. The content of this Chapter is in part discussed in Riciputi et al. (2005).

5.1 Model properties

As stated in Chapter 4 the models adopted in this work can be *one-component* or *two-component*, i.e. made of stars only or made of stars plus a dark matter halo. Each of the one-component γ-models is characterized by the *four* parameters (γ, q, k, θ), where γ determines the shape of the density distribution of the model (see Equation [4.2])), q its flatness (Equation [4.3]), k the degree of tangential anisotropy allowed in the model (Equation [3.17a]), and θ the inclination of the line-of-sight (l.o.s.) with respect to the axis of symmetry of the model (Equation [2.19]). The number of parameters increases up to *nine* if two-component models (i.e., those with a dark matter halo), or models with a central super-massive black hole (BH) are considered. Due to the number of parameters and to the computational time required to complete each simulation run, an *orthogonal exploration* of the parameter space that characterize the model family has been adopted. The alternative to this approach consists in a *Monte-Carlo* simulation, but it is not viable in this case, because its enormous requirement of computational time. The adopted approach guarantees to keep the computational time within reasonable limits, still giving the chance to inspect all the properties of the models.

5.1.1 One-component models

Following the guidelines above we begin our analysis considering the one-component models, focusing in particular on the effects of the various parameters on the projected velocity $\overline{v_p}$ field. A few representative models are here illustrated in some detail, in particular we consider isotropic rotator models ($k = 1$) seen edge-on ($\theta = \pi/2$), since the effects of changing the parameters are maximal for $\overline{v_p}$ in this case. As it always the case in this work, all the lengths are normalized to *scale radius* r_c already defined in Section 4.1, and all the velocities and velocity dispersion are normalized to $\sqrt{GM/r_c}$. Moreover in all the figures the position of the *circularized effective radius* R_e (defined as the radius on the projection plane that contain half of the model mass), and the position of $R_e/8$ will be marked for each model as solid dots (●) and empty dots (○), respectively.

Figure 5.1 shows the resulting projected velocity field for three different

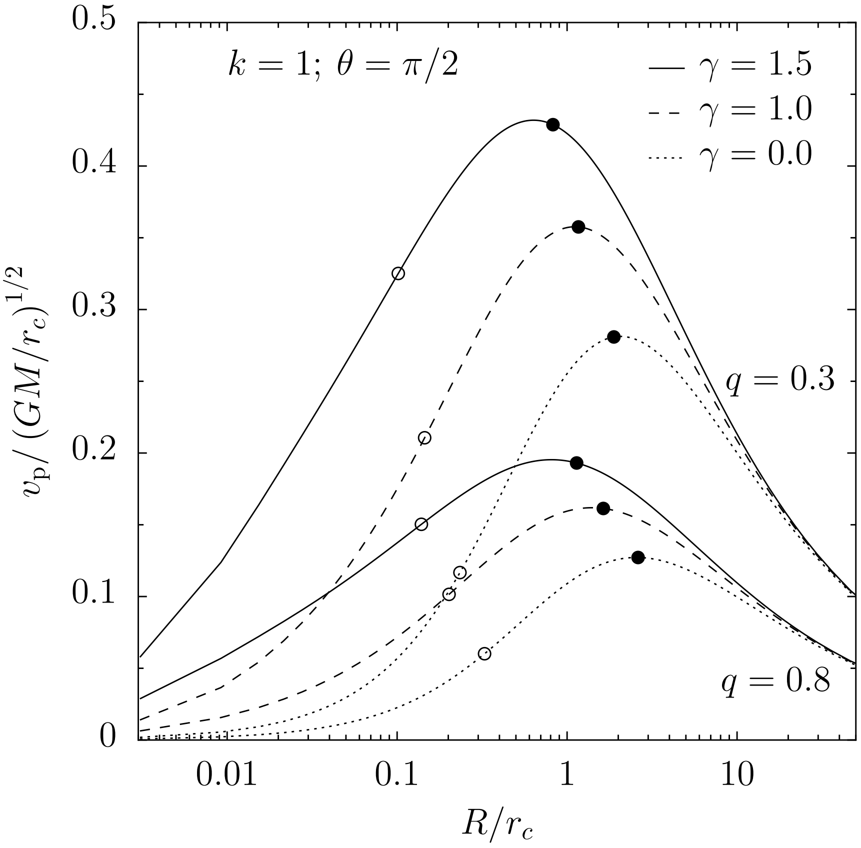

Figure 5.1 – Projected rotation velocity along the equatorial plane for a set of models with $\gamma = 0, 1, 1.5$, and two different flattenings ($q = 0.3$, 0.8). In all cases, models are isotropic rotators ($k = 1$) seen edge-on ($\theta = \pi/2$). Aperture radii corresponding to $R_e/8$ and R_e are marked as empty dots (○) and solid dots (●), respectively.

values of γ $(0, 1, 1.5)$ and two different flattening ($q = 0.3, 0.8$). As expected, $\overline{v_p}$ always vanishes in the central regions. Furthermore, for any fixed value of γ, $\overline{v_p}$ is larger at all radii in the case of maximum ellipticity ($q = 0.3$), than for more spherical models ($q = 0.8$), since larger rotational velocities are necessary to support higher flattenings in the isotropic case. On the other hand, at fixed ellipticity, the presence of a steep central density cusp affects the inner part of the rotation curve, in the sense of larger values of $\overline{v_p}$ and a peak velocity closer to the center for $\gamma = 1.5$, as compared to the cases of a shallower cusp ($\gamma = 1$), and, in turn, of a flat core ($\gamma = 0$). At large distances from the center, instead, $\overline{v_p}$ depends weakly on γ, because the density profile of the adopted family goes to zero as $\sim r^{-4}$ independently of γ and all models have finite mass.

In Figure 5.2 we show the aperture velocity dispersion $\sigma_{\rm ap}$ for the same set of models seen edge-on ($\theta = \pi/2$), in case of fixed maximum flattening $q = 0.3$, either supported by tangential anisotropy ($k = 0$) or by ordered rotation ($k = 1$). Since $\overline{v_p}$ the rotational velocity tends to zero towards the galaxy center, almost no differences are found for the aperture velocity dispersion in the non-rotating ($k = 0$) and maximally rotating ($k = 1$) cases, when $\sigma_{\rm ap}$ is measured within small apertures $r_{\rm ap} \sim R_e/8$, independently of γ. When integrating $\sigma_{\rm los}$ over a larger area ($\sim R_e$), the resulting $\sigma_{\rm ap}$ is larger for $k = 0$ than for $k = 1$, since the tangential anisotropy is maximal in the former case, while the streaming motions (that are maximal for $k = 1$) contribute with both a positive and a negative terms to $\sigma_{\rm los}$ [see equation (2.17)]. The differences between the measured $\sigma_{\rm ap}$ of the anisotropy-supported and rotation-supported models are larger for increasing γ, and attain a value of about 40% for $r_{\rm ap} = R_e$ in the most extreme case ($\gamma = 1.5$). However, for more realistic aperture ($r_{\rm ap} = R_e/8$), these differences are always well within 15%. Considering that the models shown in Figure 5.2 are maximally flattened and seen edge-on, with both these factors contributing to make the difference between the rotating and not rotating cases stronger, we can safely conclude that the contribution of the rotational velocity to the *observed* central velocity dispersion is usually negligible, at least for elliptical galaxies that can be observed within the very central regions, i.e. those that are in the local Universe. This conclusion implies that a systematic decrease of rotational support with increasing luminosity *is not* at the origin of the

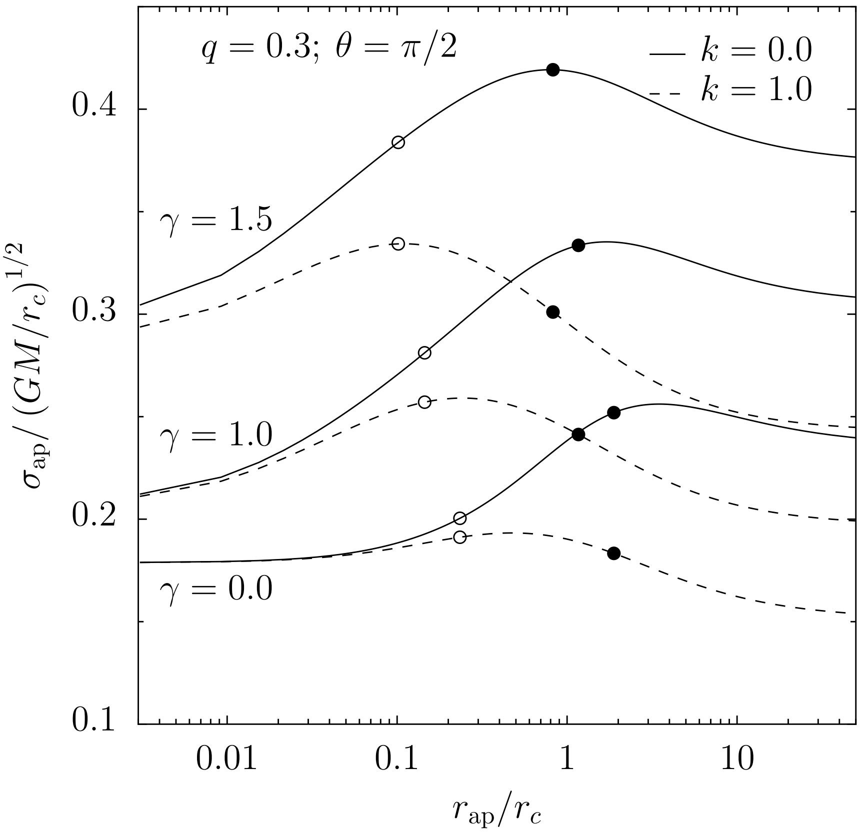

Figure 5.2 – Aperture velocity dispersion $\sigma_{\rm ap}$ as a function of the circular aperture radius $r_{\rm ap}$, for not rotating ($k = 0$) and isotropic ($k = 1$) models, with $\gamma = 0, 1, 1.5$. Maximum flattening ($q = 0.3$) and edge-on projection ($\theta = \pi/2$) are assumed in all cases. Aperture radii corresponding to $R_e/8$ and R_e are marked as empty dots (○) and solid dots (●), respectively.

Fundamental Plane tilt of elliptical galaxies. This result reinforces a similar conclusion found by Lanzoni & Ciotti (2003) that perform a similar analysis adopting different galaxy models as thoroughly explained in Section 5.3.

5.1.2 Two-component models

Similarly to the one-component models, we show the effects of the various parameters on the projected fields for the models with dark matter halo. Many models, with different halo shape, mass, and scale radius have been studied, and here few representative cases are illustrated. In particular the halo is supposed to be a *spherical* ($q_h = 1$) Hernquist ($\gamma_h = 1$) distribution of dark matter, with a mass $M_h = 5M_*$, and with a scale radius $r_h = 2r_c$. Figure 5.3 is the analogous of Figure 5.1 for the two-component models, and it shows the projected velocity fields $\overline{v_p}$ for three different values of γ_* $(0, 1, 1.5)$ and two different flattening ($q_* = 0.3, 0.8$). The same observations already reported in Section 5.1.1 apply here. As it was expected the dark matter halo does not affect significantly the models projected velocity in the central regions, where $\overline{v_p}$ vanishes. At fixed γ_*, $\overline{v_p}$ is larger for more flattened models, and at fixed ellipticity cuspier models have higher value of $\overline{v_p}$ and peak velocity closer to the center. Finally at large distances from the center $\overline{v_p}$ does not depends on γ_*, because $\rho_* \propto 1/m^4$ there, independently of γ_*. As can be easily noted comparing Figure 5.3, and 5.1, adding a DM halo to the models makes their projected velocities steeper, with a larger peak value. For a fixed flattening this effect is more marked for models with a smaller γ_*, making the $\overline{v_p}$ curves more similar.

In Figure 5.4 the aperture velocity dispersion $\sigma_{\rm ap}$ is shown for the same set of models seen edge-on ($\theta = \pi/2$), in case of fixed maximum flattening $q = 0.3$, either supported by tangential anisotropy ($k = 0$) or by ordered rotation ($k = 1$), and with the same spherical Hernquist DM halo. Even in this case almost no differences are found for the aperture velocity dispersion in the non-rotating ($k = 0$) and maximally rotating ($k = 1$) cases, when $\sigma_{\rm ap}$ is measured within small apertures $r_{\rm ap} \sim R_e/8$, independently of γ, because even in these models the rotational velocity $\overline{v_p}$ tends to zero towards the galaxy center. On the other hand, over a larger area ($\sim R_e$), the velocity dispersion $\sigma_{\rm ap}$ is larger for $k = 0$ than for $k = 1$, as it is the case for the one-component models, and the differences are larger for increasing γ_*.

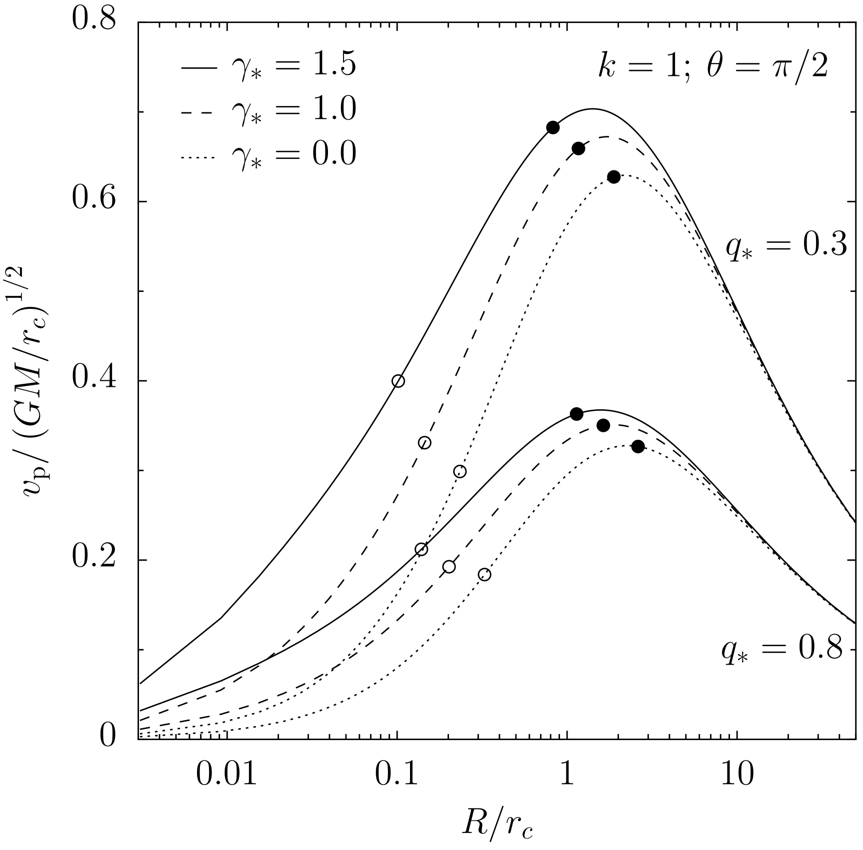

Figure 5.3 – Projected rotation velocity along the equatorial plane for a set of models with $\gamma_* = 0, 1, 1.5$, two different flattenings ($q_* = 0.3$, 0.8), and with an halo with $\gamma_h = 1$, $q_h = 1$, $M_h = 5M_*$, and $r_h = 2r_c$. In all cases, models are isotropic rotators ($k = 1$) seen edge-on ($\theta = \pi/2$). Aperture radii corresponding to $R_e/8$ and R_e are marked as empty dots (○) and solid dots (●), respectively.

Moreover, in presence of a DM halo, these differences attain a value of about 50% for $r_{\rm ap} = R_e$ in the most extreme case ($\gamma_* = 1.5$), while for smaller apertures ($r_{\rm ap} = R_e/8$) the differences are always within 20%, not so far from what it has been found for the one-component models. The same conclusion drawn in the case of the one-component models, can thus be stated here. Even for models with a DM halo, the contribution of the rotational velocity to the *observed* central velocity dispersion is usually negligible, at least for elliptical galaxies observed within the very central regions, and *we conclude that a systematic decrease of rotational support with increasing luminosity is not at the origin of the Fundamental Plane tilt of elliptical galaxies*.

5.2 Black hole sphere of influence

An issue often debated is how a central super-massive black hole (BH) affects the kinematical fields in the central regions of the host galaxy, and if it has a valuable effect on the global characteristics such as the scaling laws of elliptical galaxies (Ferrarese & Merritt 2000). The astrophysical relevance of this problem is obvious, due to the implications of the slope value of the $M_{\rm BH}$-σ_0 relation (Ciotti & van Albada 2001; Nipoti et al. 2003b). In order to address these questions several different models have been explored, varying both the intrinsic and observational parameters (i.e., γ, q, k, $\mu \equiv M_{\rm BH}/M_*$, θ), adopting both one and two-component models, and studying extensively the results of models with and without a BH. The conclusions are similar for all models, so that we report here only a significant example, characterized by $\gamma = 1$, $q = 0.3$, $k = 1$ and a BH mass chosen according to the Magorrian relation: ($\mu = 10^{-3}$, Merritt & Ferrarese 2001a; Magorrian et al. 1998). In Figure 5.5a we show the ratio of the spatial and projected velocity along the major axis between two models with and without the central massive BH. Moreover, while v_φ changes of nearly one order of magnitude in the innermost region, $\overline{v_p}$ is much less affected by the presence of the BH. Figure 5.5b is analogous to Figure 5.5a, for the velocity dispersion. In this case, the intrinsic equatorial one-dimensional velocity dispersion (note that the model is isotropic), the l.o.s.velocity dispersion along the major axis, and finally the aperture velocity dispersion for $r_{\rm ap} \lesssim r_c$, are shown.

As for the rotational velocity, the influence of the BH is negligible for

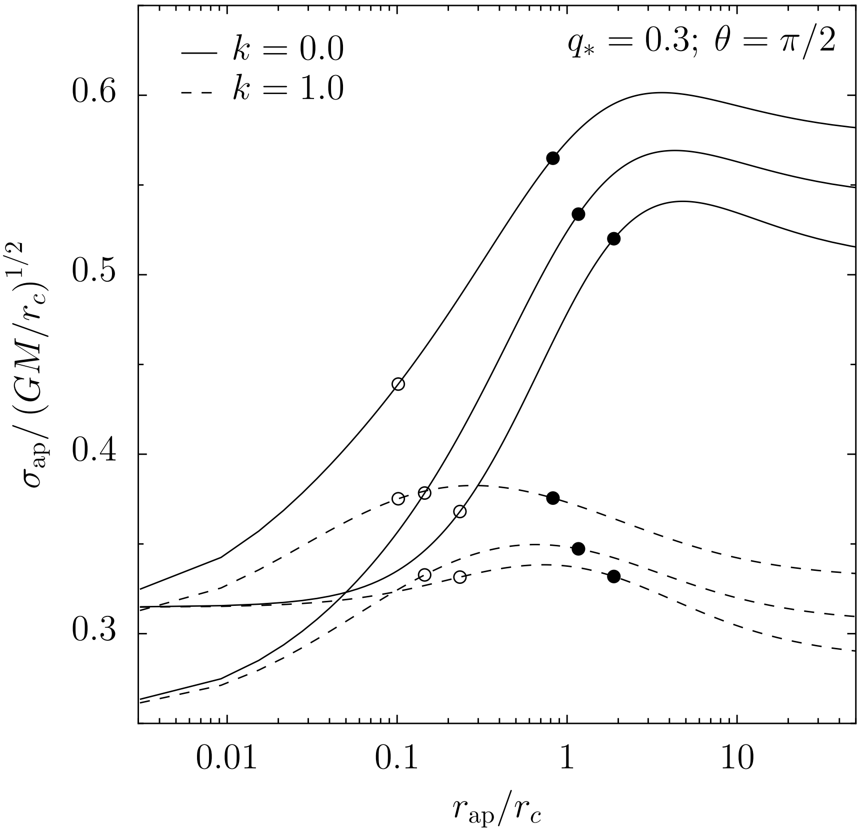

Figure 5.4 – Aperture velocity dispersion $\sigma_{\rm ap}$ as a function of the circular aperture radius $r_{\rm ap}$, for not rotating ($k = 0$) and isotropic ($k = 1$) models, with $\gamma_* = 0, 1, 1.5$. Maximum flattening ($q_* = 0.3$), edge-on projection ($\theta = \pi/2$), and a DM halo with $\gamma_h = 1$, $q_h = 1$, $M_h = 5M_*$, and $r_h = 2r_c$ are assumed in all cases. Aperture radii corresponding to $R_e/8$ and R_e are marked as empty dots (○) and solid dots (●), respectively.

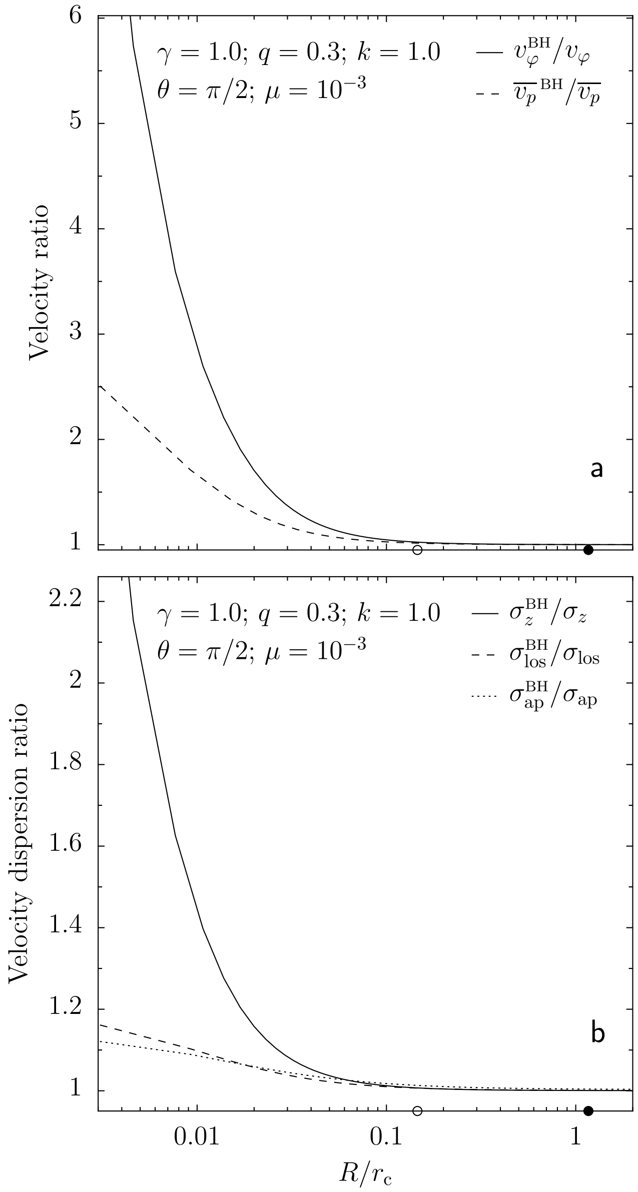

Figure 5.5 – Panel a): Ratio for the azimuthal (solid line) and projected (dashed line) velocities along the major axis between a model with and without a central BH. The model parameters are: $\gamma = 1$, $q = 0.3$, $k = 1$, $\theta = \pi/2$ and $\mu = 10^{-3}$. Panel b): Ratio between the velocity dispersion fields of models with and without a central super-massive black hole. The solid and dashed lines refer, respectively, to the intrinsic and to the projected l.o.s.velocity dispersions along the major axis of the model. The dotted line is the aperture velocity dispersion as a function of the circular aperture radius. Model parameters are the same as in panel a. The empty and solid dots along the x-axis of both panels, mark R_e and $R_e/8$, respectively.

distances from the center larger than $\sim R_e/8$, and it is correspondingly stronger for σ_z, $\sigma_{\rm los}$ and $\sigma_{\rm ap}$. In particular, the latter is never affected for more then 10% even for unrealistically small (very central) aperture radii. We also note that, where relevant, the effect of the BH is stronger on the streaming velocity, than on the velocity dispersion fields. Thus we found that the existence of a super massive BH can be neglected in practically all astrophysical investigations, based on the measured "central" velocity dispersion, like for instance the Faber-Jackson relation (Faber & Jackson 1976), the FP (Djorgovski & Davis 1987; Dressler et al. 1987), and the v/σ plane (Illingworth 1977; Binney 1978), where $r_{\rm ap} \simeq R_e/8$. The main conclusion that can be drawn from these results is that the definition of BH "sphere of influence" cannot be univocal, but it depends on the considered quantities: in particular, if one considers the intrinsic or the projected kinematical fields, the effect of the central BH is quite different. Moreover, in order to reveal the presence of a central super massive BH, and/or estimate its effects, it is worth analyzing the streaming velocity field, while the velocity dispersion is better suited for studies where the influence of the BH needs to be minimal. The weak ($\lesssim 10\%$) dependence of $\sigma_{\rm ap}$ on the presence/absence of a central BH demonstrates that the observed $M_{\rm BH}$-σ relation (Ferrarese & Merritt 2000; Gebhardt et al. 2000) is a non trivial property of elliptical galaxies and bulges, linking together a very local quantity ($M_{\rm BH}$), to a global one (σ), in a way that still needs to be explained. As a consequence of these results, our further investigations are all performed with models with no central BH.

5.3 Fundamental Plane thickness

Addressing the Fundamental Plane (FP) *tilt* and *thickness* issue is a long lasting problem in astrophysics. As already stated in Chapter 1 these to properties of the FP are strictly related to the *structural* and *dynamical* characters of elliptical galaxies, possibly as a consequence of their formation process. In particular it is interesting to study if *ordered motion* and *projection effects* could have some appreciable effect on the thickness of the plane. A significant step forward in the study of the structural and dynamical implications of the tilt and thickness of the FP was made by Bertin et al. (2002), who introduced the more general Monte-Carlo approach discussed above, although limited to spherical models. The Monte-Carlo approach was successively extended by Lanzoni & Ciotti (2003), hereafter LC03, that investigate the importance of projection effects on the FP thickness by adopting fully analytical axysimmetric Ferrers (1877) galaxy models. In particular, LC03 found that while projection effects do contribute to the observed FP scatter, nonetheless the FP *physical scatter* (as determined by variations of the physical properties from galaxy to galaxy), sums up to the 90% of the measured scatter. However, while fully reliable about projection effects on R_e (which are independent of the specific homeoidal density profile adopted), Ferrers models in the central regions are unrealistically flatter than real galaxies, so that doubts can be risen about the use of their central velocity dispersion σ_0. For example, LC03 found that the contribution of ordered streaming motions to the observed velocity dispersion is negligible when small/medium apertures ($\lesssim R_e$) are used for the spectroscopic observations. Here we want to verify if the same conclusions found in LC03 apply also to galaxy models that are cuspy in the central regions, therefore strengthen those results, or not. It is worth re-writing here the FP relation, already pointed out in Chapter 1:

$$\log R_{e\,\mathrm{FP}} \equiv a \log \sigma_0 + b \log I_e + c \,, \tag{5.1}$$

where $\sigma_0 \equiv \sigma_{\mathrm{ap}}$ in our notation, and $I_e \equiv L/(2\pi R_e^2)$, where L is the total galaxy luminosity, i.e. the total mass, since in our models $\Upsilon_* \equiv$ cost. The coefficients a, b, and c depend slightly on the considered photometric band (e.g. Pahre et al. 1998; Scodeggio et al. 1998), and we adopt here the values $a = 1.24 \pm 0.07$, $b = -0.82 \pm 0.02$ and $c = 0.182$ found by Jørgensen et al. (1996) for the Coma cluster.

In this section we investigate the role of projection effects on the observed FP thickness, in particular by considering the effects of ordered rotation on the adopted cuspy galaxy models. For this purpose, we consider the edge-on view of the FP, i.e. the $(\log R_{e\,\mathrm{FP}}, \log R_e)$ space, and we describe how models "move" in it, when changing the intrinsic (q, and k) and observational (θ) parameters. In Figure 5.6 we show the observed FP of the Coma cluster

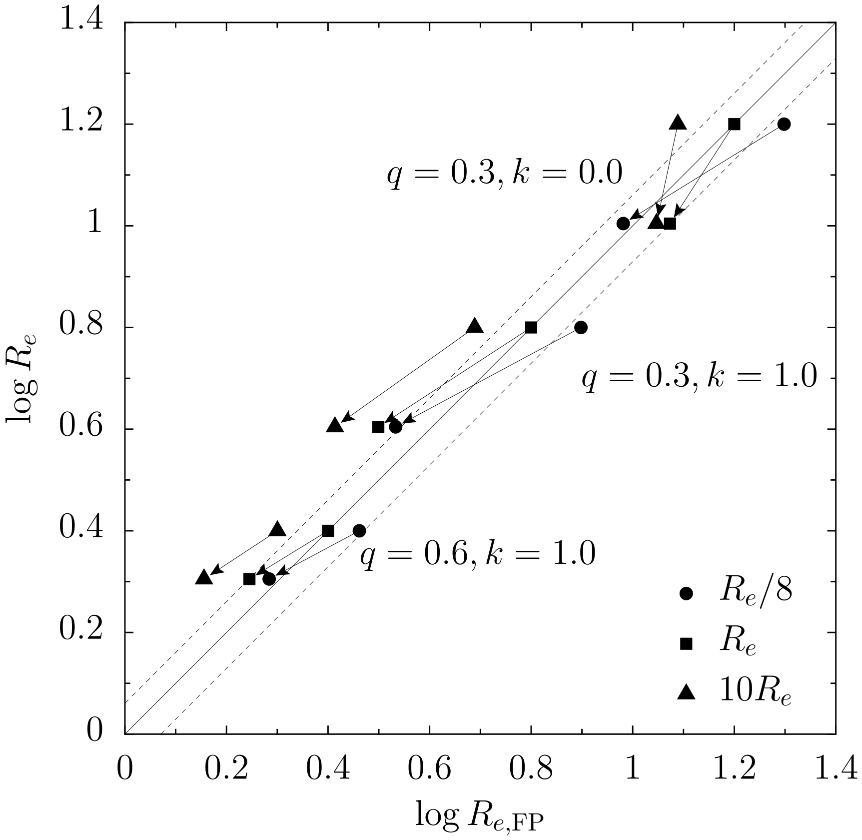

Figure 5.6 – Projection effects on the galaxy models in the ($\log R_{e\,\mathrm{FP}}$, $\log R_e$) space, where the FP is seen edge-on. The solid and dashed lines mark the best-fit and the rms scatter of the observed FP for Coma cluster galaxies. Three models, all with $\gamma = 1$, but different flattening ($q = 0.3$, 0.6), and amount of rotational support ($k = 0$, 1) are shown. Three spectroscopic apertures ($r_{\mathrm{ap}} = R_e/8$, R_e, $10R_e$) within which σ_{ap} is measured, are considered for each model. The l.o.s. projection angle changes from $\theta = 0$ (face-on) at the upper point of the arrows, to the $\theta = \pi/2$ (edge-on) at the lower point of the same arrows. Models are arbitrarily placed in this space, with the cases for $\theta = 0$ and $r_{\mathrm{ap}} = R_e$ exactly settled on the FP best-fit line.

ellipticals and its scatter[1], and we illustrate the behavior of three families of models, all characterized by the same density profile ($\gamma = 1$), but different flattening q and/or amount of rotational support k (see labels in the Figure). Each model is projected along the two “extreme” los directions: face-on ($\theta = 0$), and edge-on ($\theta = \pi/2$). We also investigate the effect of adopting different apertures to measure σ_0, namely $R_e/8$, R_e, and $10\,R_e$. Models are arbitrarily placed in this space, with the case $\theta = 0$, and $r_{\rm ap} = R_e$ placed on the FP best-fit line. As a general remark in case of not spherical systems, varying the projection angle from 0 to $\pi/2$, makes R_e to decrease, thus producing a vertical down-shift of the representative models. Similarly, when R_e decreases, I_e increases, and, given the expression of $R_{e\,\rm FP}$, galaxy models move horizontally towards the left, while an increase of σ_0 produces a horizontal shift towards the right. As expected, displacements are smaller for rounder systems, while the effect of the rotational velocity and the aperture radius is less trivial. For $k = 1$ (isotropic rotators), the variation of $\sigma_{\rm ap}$ with the viewing angle θ is slightly dependent on the considered spectroscopic aperture, so that the model displacements are all in the same direction, almost parallel within each other. A very similar behavior is found for $r_{\rm ap} = R_e/8$ for not rotating anisotropic galaxies ($k = 0$), while the direction of displacements changes in this case if larger apertures are considered. It is worth noting that both the flattening and the projection have been chosen to be *extreme*, thus maximizing the observed “movements” onto the plane. We therefore find that, *due to projection effects, galaxies move in directions which are not exactly parallel to the edge-on FP, but the entity of these displacements is small enough to always maintain the models within the observed FP thickness*. This is true for any flattening, amount of rotational support, and considered aperture, and we have also verified that results are almost independent of the model central cusp γ. A comparison of our results with those found in LC03, where models with flat cores are considered, reveals very similar behaviors, thus confirming this latter finding. Moreover,

---

[1] Note that the observed velocity dispersion entering the FP relation is usually corrected to a circular aperture with diameter $1.19\,h^{-1}$ kpc (e.g. Jørgensen et al. 1999), corresponding to a radial range $\sim 0.05\,R_e$–R_e for $h = 0.5$, and for typical values of R_e. In any case, the FP equations derived by using $R_e/8$ or the fixed metric aperture are in mutual good agreement (see Jørgensen et al. 1996).

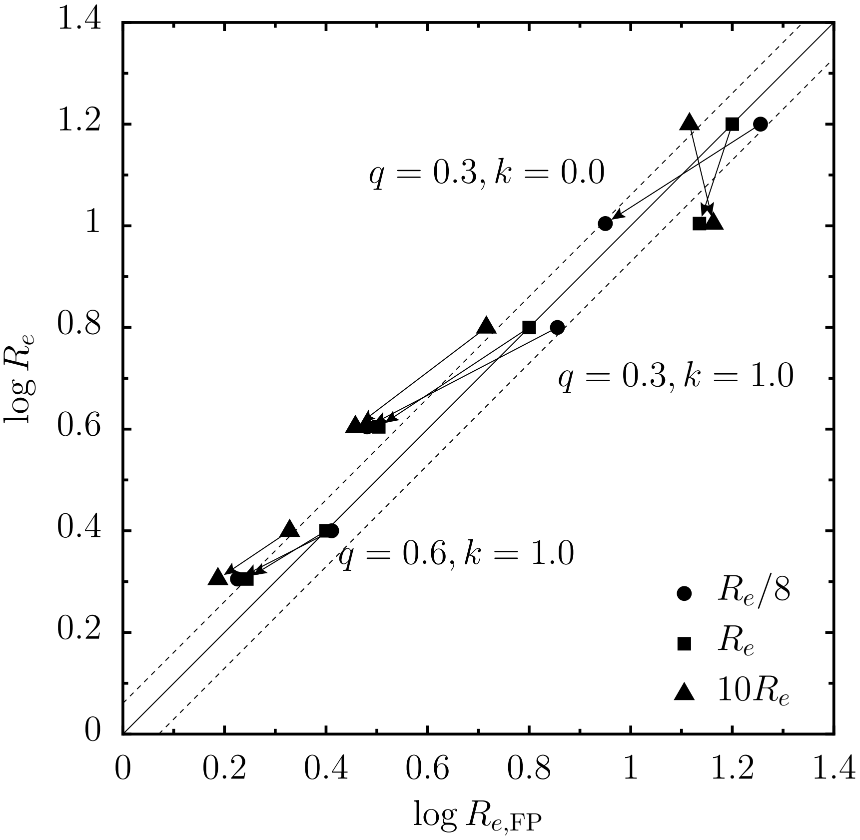

Figure 5.7 – Projection effects on the two-component models in the ($\log R_{e\,\mathrm{FP}}$, $\log R_e$) space, where the FP is seen edge-on. Same parameters and settings of Figure 5.6, plus a spherical ($q_h = 1$), Hernquist ($\gamma_h = 1$) DM halo with a mass $M_h = 5M_*$, and a scale radius $r_h = 2r_c$.

such a similarity between model displacements in our case and in LC03 also suggests that all conclusions of the statistical Monte-Carlo analysis in that paper are still valid when more realistic, cuspy galaxy models are used. In other words, from the trends in Figure 5.6, and the comparison with the results of LC03, we can conclude that projection effects only marginally contribute to the FP thickness, 90% of it being attributable to real variations of the physical properties from galaxy to galaxy.

Similar results are found when two-component models are considered, as can be easily seen looking at Figure 5.7. The Figure is the analogous of Figure 5.6 where a DM halo has been added, the models have the same parameters already cited for the one-component models, i.e. $\gamma_* = 1$, different flattening q_*, and amount of rotational support k. Moreover a spherical ($q_h = 1$), Hernquist ($\gamma_h = 1$) halo, with a mass $M_h = 5M_*$, and a scale radius $r_h = 2r_c$ is adopted as a representative of many more cases that have been studied. It is clear, by comparing Figures 5.7 and 5.6, that the points "movements" on the ($\log R_{e\,\mathrm{FP}}$, $\log R_e$) plane are very similar, especially when isotropic models ($k = 1$) are taken into account. The case of not rotating models ($k = 0$) at medium and large apertures, can be easily explained looking at the high values assumed by σ_{ap} in Figure 5.4 for medium to large apertures, as it was also the case for the one-component models. Thus, the conclusions already drawn for one-component models can be also applied to models with a DM halo, and we can state that, even when two-component models are taken into account, projection effects only marginally contribute to the FP thickness.

5.4 The v/σ-ϵ plane

A question strictly related to the previous one is that of the interpretation of the so-called v/σ-ϵ plane, an important tool often used to investigate to what extent the observed flattening of galaxies is ascribable to the rotation or to the anisotropy of the velocity dispersion tensor (Illingworth 1977; Binney 1978). In fact, it is well known that axisymmetric homeoidal systems of different flattenings, characterized by an isotropic velocity dispersion tensor and supported by streaming motions, describe well defined loci in this plane. In particular, all systems with not negligible anisotropy

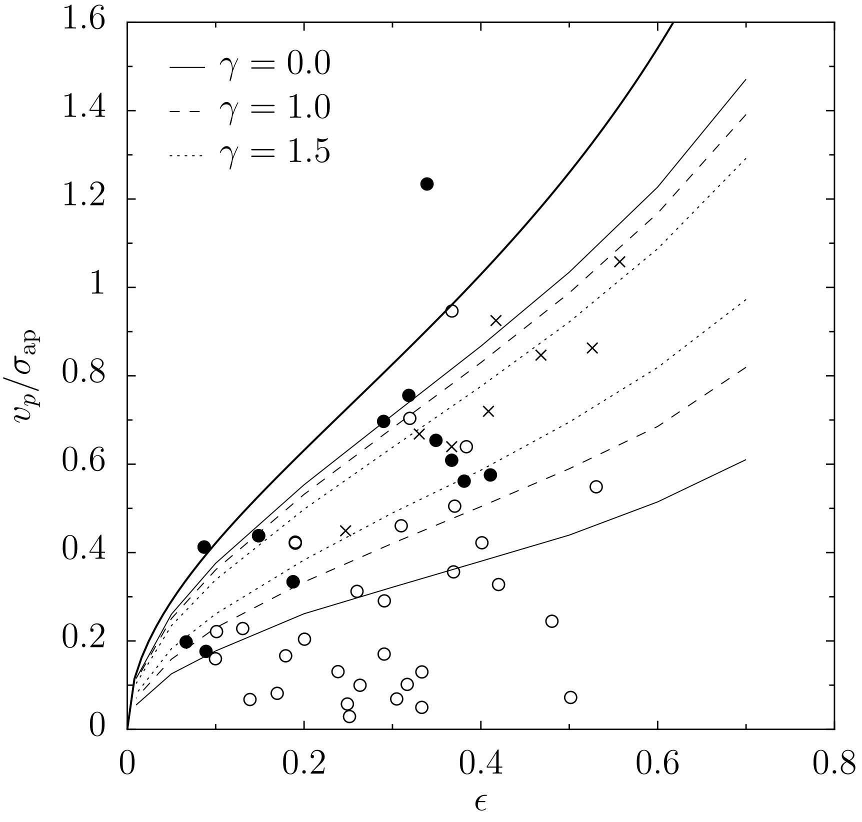

Figure 5.8 – Rotational parameter for isotropic, edge-on models. The solid thick curve is the locus of isotropic, classical ellipsoids as obtained by Binney (1978), and it is not corrected for any projection effect. Symbols are the dataset from Davies et al. (1983); empty dots (○) are bright elliptical galaxies, solid dots (●) are faint elliptical galaxies, and crosses (×) are bulges. The upper set of curves represents our models when $v_p = \overline{v_p}_{\rm max}$, while the lower set of curves represents our models when $v_p = \overline{v_p}(R_e/8)$.

are expected lie below the curve representing models seen edge-on (thick solid line in Figure 5.8, see also Binney & Tremaine 1987). Usually, the test curve is obtained when v and σ represent the mass weighted mean rotation speed and velocity dispersion computed over all the galaxy: in this case, it can be shown that the quantity v/σ does not depend on the specific mass density profile if it is stratified on homeoids (Roberts 1962; Binney & Tremaine 1987). However, observational data used to infer how important is the rotational support for a given galaxy, commonly consist in the *maximum* available value of the rotational velocity along the major axis $v_{\max}$ and the "*central*" l.o.s. velocity dispersion σ_0. Indeed, Evans & de Zeeuw (1994) showed that the $v_{\max}/\sigma_0$ ratio against ellipticity, for their nearly isotropic "power-law" galaxy models, systematically lies below the curve of classical spheroids obtained by using the virial quantities. However, these models are stratified on homeoidal surfaces in the potential, but not in the density distribution, and a totally isotropic velocity dispersion tensor cannot be defined for them, so that a completely coherent comparison with the curve of classical spheroids is not allowed. Ciotti & Bertin (2005) addressed the same issue by adopting axysimmetric power-law galaxy models, in which the potential is obtained by means of homeoidal expansion. The main result is to confirm the results of Evans & de Zeeuw (1994). Here we address this issue further, by studying the behavior of our *one-component* models in the isotropic ($k = 1$), edge-on ($\theta = \pi/2$) case. In particular, we study effects of both varying the steepness of the central cusp, and the definition of velocity and velocity dispersion entering the rotation parameter v/σ. We adopt $\sigma_{ap}(R_e/8)$ to mimic the observed velocity dispersion, and we consider both the maximum projected velocity $\overline{v_p}_{\max}$ and the projected velocity at $R_e/8$, as representative of the measured rotation. The resulting trends of the rotation parameter thus defined, against ellipticity, for edge-on los projections, are shown in Figure 5.8, for models with flat cores ($\gamma = 0$), and steep central cusps ($\gamma = 1, 1.5$). As a first remark, we note that as a consequence of adopting *central* kinematical properties, instead of the virial ones, *all resulting curves lie below the locus of isotropic, classical ellipsoids obtained from the tensor virial theorem.* Deviations with respect to the "classical" expectation are larger when the rotational velocity is measured at $R_e/8$, than at its peak, and a dependence on the shape of the density profile is

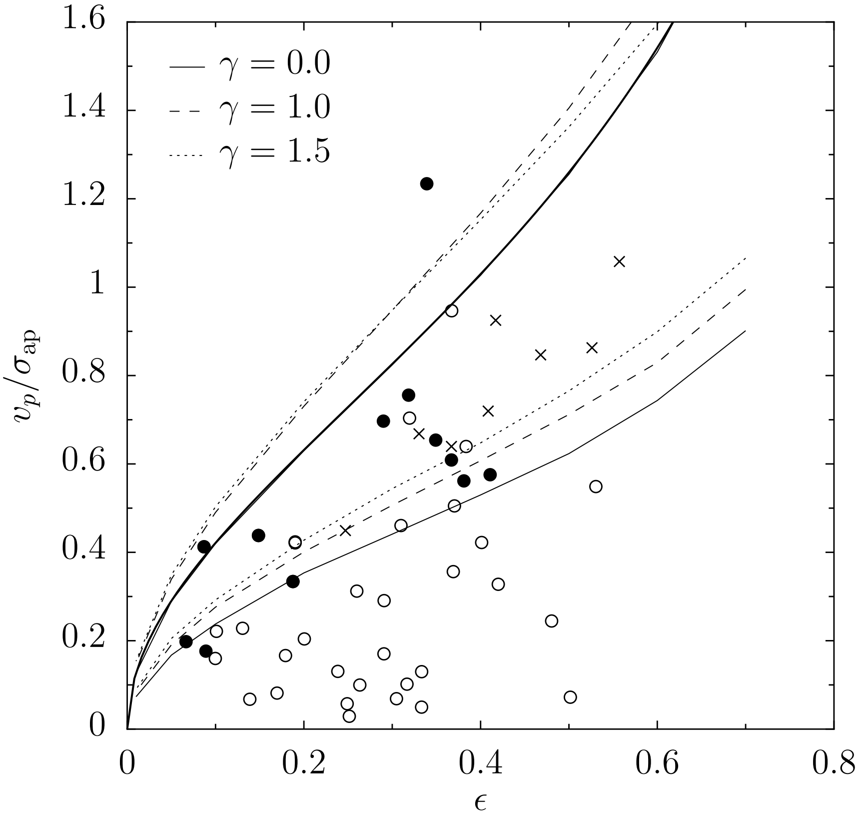

Figure 5.9 – Rotational parameter for isotropic, edge-on models with spherical ($q_h = 1$), Hernquist ($\gamma_h = 1$) DM halo with mass $M_h = 5M_*$, and a scale radius $r_h = 2r_c$. The solid thick curve is the locus of isotropic, classical ellipsoids as obtained by Binney (1978), and it is not corrected for any projection effect. Symbols are the same of Figure 5.8. The upper set of curves represents our models when $v_p = \overline{v_p}_{\rm max}$, while the lower set of curves represents our models when $v_p = \overline{v_p}(R_e/8)$.

also apparent, particularly in the former case. This result confirm Evans & de Zeeuw (1994) and Ciotti & Bertin (2005) (see also Appendix A).

Figure 5.9 shows similar results obtained for models with a spherical ($q_h = 1$), Hernquist ($\gamma_h = 1$) DM halo, with mass $M_h = 5M_*$, and a scale radius $r_h = 2r_c$. It should be noted that when considering the *maximum* projected velocity $\overline{v_p}_{\max}$ as representative of the measured rotation, our models stay above the theoretical curve.

In summary, we confirm that a note of caution should be used when interpreting the position of galaxies in the v/σ-ϵ diagram as a measure of their degree of rotational support. In fact, the locus of isotropic rotators in this plane, quite sensitively depends on the adopted definitions of the kinematical quantities entering the rotation parameter, and, in turn, on the shape of the density profile. Deviations with respect to the case of classical ellipsoids increases with increasing galaxy ellipticity, and typically are in the sense of a *smaller* rotational parameter when central (instead of global) values of the rotation velocity and velocity dispersion are used. An exception to this general trend has been noted in the case of models with DM halo, when the *maximum* projected velocity is adopted as representative of the measured rotation. This results reveals how much attention should be payed when using the v/σ-ϵ plane as a tool to measure the ellipticals degree of rotational support. In addition, one also should take into account that all the discussed results are obtained for models with density distributions stratified on homeoidal surfaces, while real galaxies hardly have such mass profiles.

Chapter 6

Conclusions

DISCUSSION and conclusions of the main results obtained as applications of the developed numerical code are summarized in Section 6.1, emphasizing the key points of the topics faced so far. These results are just simple yet interesting examples of the code developed as the main point of this Thesis. Another possible application of the code is briefly described in Section 6.2.

6.1 Conclusions

In the present work we have constructed a flexible and original code based on "spectral methods" to solve the Jeans equations and project the dynamical fields on the plane of the sky, and we have focused our attention on a number of issues related to the dynamics and scaling relation of elliptical galaxies, as discussed in Chapter 1. In order to get more insight in this topics we have made use of a modelization paradigm based upon the theory of collisionless systems driven by the Collisionless Boltzmann Equation, and adopting *axisymmetric two-integrals oblate* galaxy models to describe *real* early-type galaxies, as summarized in Chapter 2. Despite the simplification introduced with the assumed paradigm, it is not possible to solve the intrinsic and projected dynamics of these models analytically. Thus a numerical approach to the problem must be chosen, and among all the possibilities the one we have adopted and implemented it has been described in Chapter 3. This code has been developed for being flexible, accurate and as general as possible. In Chapter 4 the adopted density distribution models have been described: they are axisymmetric oblate γ-models (Dehnen 1993; Tremaine et al. 1994; Qian et al. 1995), with homeoidal density distribution, and constant stellar mass-to-light ratio. Moreover a dark matter halo and a super-massive black hole can be added. Finally in Chapter 5 the main results found during this work have been reported, especially focusing our attention to address open question regarding the effects of a central super-massive black hole on the intrinsic and projected dynamics of the central regions of the host ellipsoids (Section 5.2). The implications for the "sphere of influence" definition and for the $M_{\rm BH}$-σ relation are there discussed. The projection effects on the Fundamental Plane thickness have been studied in Section 5.3. Finally in Section 5.4, we have studied how our models are placed in the v/σ-ϵ plane, to better understand whether this tool can be considered reliable to measure the amount of ordered and random motions which are present in *real* ellipticals. The conclusions that we have drawn for the adopted class of models are briefly summarized below:

- Rotational velocity contributes to the *observed* (projected) central velocity dispersion in negligible way, thus implying that a systematic decrease of rotational support with increasing luminosity *is not* at the origin of the Fundamental Plane tilt.

- The same result holds when models with a dark matter halo are considered instead of models made of stars only.
- The influence of the super-massive black hole on the dynamics of the host ellipsoid is not negligible only for distances well inside $\sim R_e/8$. In particular projected quantities are alway less affected by the BH presence that the intrinsic one, thus making the definition of the BH "sphere of influence" not univocal, but depending on the considered quantities.
- The weak ($\lesssim 10\%$) dependence of the aperture velocity dispersion on the presence/absence of a central BH demonstrates that the observed $M_{\rm BH}$-σ_0 relation (Ferrarese & Merritt 2000; Gebhardt et al. 2000) is a non trivial property of elliptical galaxies and bulges, linking together a very local quantity ($M_{\rm BH}$), to a global one (σ), in a way that still needs to be explained.
- Regarding the Fundamental Plane thickness, we have found that due to projection effects, galaxies move in directions which are not exactly parallel to the edge-on FP, but the entity of these displacements is small enough to always maintain the models within the observed FP thickness.
- We thus conclude that projection effects only marginally contribute to the FP thickness, 90% of it being attributable to real variations of the physical properties from galaxy to galaxy. Similar results are found when two-component models (i.e. models with dark matter halo) are considered.
- When placing our *isotropic* models on the v/σ-ϵ plane, we note that as a consequence of adopting *central* kinematical properties, instead of the virial ones, all resulting curves lie below the locus of isotropic, classical ellipsoids obtained from the tensor virial theorem, so that a note of caution should be used when interpreting the position of galaxies in the v/σ-ϵ diagram as a measure of their degree of rotational support.

Of course, all these results are far away from giving us a fully comprehension of the elliptical scaling relations. Nevertheless they all point toward the fact that these scaling relations are telling us something, not yet fully understood, about the way in which elliptical galaxies had formed. Our conclusions, obtained for realistic early-type galaxy models, reinforce and extend, those already drawn by Lanzoni & Ciotti (2003), and seem to suggest that scaling relations, and in particular the Fundamental Plane, are the relic of a common formation scenario for elliptical galaxies.

6.2 A further application: the PG1115+80 lens system

Being our code such a flexible tool, we are going to apply it to the study of the lens system PG1115+80 (Treu & Koopmans 2002b). These authors have recently started a survey of spheroidal (E/S0) galaxy with the Echelle Spectrograph and Imager (ESI) on the W.M. Keck II Telescope: the Lens Structure and Dynamics (LSD) Survey (Treu & Koopmans 2002a). The aim of the LSD Survey is to measure the internal kinematics of a dozen gravitational lens galaxies up to $z = 1$, allowing a powerful combination of dynamical and lensing constraints on their mass distribution. The aim of this survey is to clarify the origin of the E/S0 galaxies, and better understanding their internal structure and evolution with redshift. As a side-product of this survey the Hubble constant H_0 can be measured provided that the degeneracies inherent to the mass distribution of the lenses would be broken.

As throughly explained in Treu & Koopmans (2002b), PG1115+80 ($z = 0.31$, Weymann et al. 1980) is not part of the LSD Survey because of the presence of a massive compact group nearby that could affect the mass distribution of lens galaxy through interaction. However, this system is particularly interesting because time delays between the lensed quasar images ($z_s = 1.71$) are available (Schechter et al. 1997; Barkana 1997), which can be used to measure the Hubble constant. Nevertheless the value obtained for H_0 strongly depends on the assumed lens models. Whereas $\rho \propto r^{-2}$ mass models yield values of $H_0 \lesssim 50\,\mathrm{km\,s^{-1}\,Mpc^{-1}}$, steeper or constant mass-to-light models can yield values up to $60 \div 70\,\mathrm{km\,s^{-1}\,Mpc^{-1}}$.

Our aim is to apply our axisymmetric oblate galaxy models to this system, and investigate how their dynamics and projection effects can influence the estimated value for H_0. To pursue this goal, a rather complex convolution/deconvolution pipeline for our simulation data has already been assembled, in order to compare our models with the observations. These, and other refinements, are in progress now.

Appendix A

Homeoidal expansion

A.1 The method

In this Appendix we report a summary of the homeoidal expansion methods. A complete description of this method and a full discussion of its applications is given by Ciotti & Bertin (2005), hereafter CB05. The methods is particularly interesting because it can be used to investigate a variety of exact density-potential pairs with spheroidal, toroidal, or triaxial shapes for which the deviation from spherical symmetry is finite. Here we focus on two-integral axisymmetric models, deriving the explicit expressions for the intrinsic and projected dynamics.

We start by assuming a density distribution stratified on homeoidal surfaces,

$$\rho(\mathbf{x}) = \rho_0\, \tilde{\rho}(m), \tag{A.1}$$

where $\mathbf{x} = (x, y, z)$, ρ_0 is a density scale, and

$$m^2 = \frac{x^2}{a^2} + \frac{y^2}{b^2} + \frac{z^2}{c^2} = \frac{x^2}{a^2} + \frac{y^2}{a^2(1-\epsilon)^2} + \frac{z^2}{a^2(1-\eta)^2}, \tag{A.2}$$

with $a \geq b \geq c > 0$, $b/a \equiv 1 - \epsilon$, and $c/a \equiv 1 - \eta$. Note that this reduces to the prolate case when $\epsilon = \eta < 1$ and to the oblate case when $\epsilon = 0$ and $0 < \eta < 1$.

In models of astrophysical interest, the density ρ may extend to infinity (with finite or infinite mass) or be truncated (i.e., vanishing outside a prescribed boundary surface). For simplicity, in this paper we discuss only non-truncated density distributions.

It is well known (e.g. Kellogg 1953; Chandrasekhar 1969) that the (inner) potential associated with a homeoidal density distribution can be written as

$$\phi(\mathbf{x}) = -\pi\, abc\, \rho_0\, G \int_0^\infty \frac{\widetilde{\Delta\Psi}(\mathbf{x};\epsilon,\eta)}{\Delta(\tau)}\, d\tau, \tag{A.3}$$

where

$$\Delta(\tau) = \sqrt{(a^2+\tau)(b^2+\tau)(c^2+\tau)}, \tag{A.4}$$

$$\widetilde{\Delta\Psi}(\mathbf{x};\epsilon,\eta) = 2\int_{m(\mathbf{x};\tau)}^\infty \tilde{\rho}(m)m\; dm, \tag{A.5}$$

and

$$m^2(\mathbf{x};\tau) = \frac{x^2}{a^2+\tau} + \frac{y^2}{b^2+\tau} + \frac{z^2}{c^2+\tau}. \tag{A.6}$$

A.1.1 The "unconstrained" expansion

If we rescale density and potential to the quantities ρ_0 of Equation (A.1) and $4\pi G\rho_0 a^2$, *respectively*, the Poisson equation for the dimensionless density-potential pair $(\tilde{\rho}, \tilde{\phi})$ becomes

$$\tilde{\nabla}^2\tilde{\phi} = \tilde{\rho}, \tag{A.7}$$

where $\tilde{\nabla}^2 = \partial^2/\partial\tilde{x}^2 + \partial^2/\partial\tilde{y}^2 + \partial^2/\partial\tilde{z}^2$, $\tilde{x} \equiv x/a$, $\tilde{y} \equiv y/a$, $\tilde{z} \equiv z/a$ and

$$\tilde{\phi} = -(1-\epsilon)(1-\eta)\frac{a}{4}\int_0^\infty \frac{\widetilde{\Delta\Psi}(\mathbf{x};\epsilon,\eta)}{\Delta(\tau)}\, d\tau. \tag{A.8}$$

This will be the starting point of our analysis. We now expand the density $\tilde{\rho}(m)$ and the potential $\tilde{\phi}$ given in Equation (A.8) up to the first significant order in the flattening parameters. The calculations are tedious, but straightforward, and so they are not recorded here. We thus find:

$$\tilde{\rho}(m) = \tilde{\rho}(\tilde{r}) + \frac{\epsilon\tilde{y}^2 + \eta\tilde{z}^2}{\tilde{r}}\tilde{\rho}'(\tilde{r}) + O(\epsilon^2+\eta^2), \tag{A.9}$$

where $\tilde{\rho}' \equiv d\tilde{\rho}(m)/dm$ evaluated at $\epsilon = \eta = 0$, and

$$\tilde{\phi} = \tilde{\phi}_0(\tilde{r}) + (\epsilon + \eta)\left[\tilde{\phi}_1(\tilde{r}) - \tilde{\phi}_0(\tilde{r})\right] + (\epsilon\tilde{y}^2 + \eta\tilde{z}^2)\tilde{\phi}_2(\tilde{r}) + O(\epsilon^2 + \eta^2), \quad \text{(A.10)}$$

where

$$\tilde{\phi}_i(\tilde{r}) = \begin{cases} -\dfrac{1}{\tilde{r}}\displaystyle\int_0^{\tilde{r}} \tilde{\rho}(m)m^2\, dm - \int_{\tilde{r}}^{\infty} \tilde{\rho}(m)m\, dm, \quad (i = 0); \\ -\dfrac{1}{3\tilde{r}^3}\displaystyle\int_0^{\tilde{r}} \tilde{\rho}(m)m^4\, dm - \frac{1}{3}\int_{\tilde{r}}^{\infty} \tilde{\rho}(m)m\, dm, \quad (i = 1); \\ \dfrac{1}{\tilde{r}^5}\displaystyle\int_0^{\tilde{r}} \tilde{\rho}(m)m^4\, dm, \quad (i = 2). \end{cases} \quad \text{(A.11)}$$

In the above expressions, the dimensionless spherical radius is defined as $\tilde{r} \equiv r/a = \sqrt{\tilde{x}^2 + \tilde{y}^2 + \tilde{z}^2}$. Note that $\tilde{\phi}_0(\tilde{r})$ is the potential associated with $\tilde{\rho}(\tilde{r})$, as can be seen from its explicit expression. The infinite upper limit of integration appearing in two integrals could be changed to a finite constant if desired; this property is useful to deal with density distributions for which the two integrals would diverge.

So far we have not addressed the question of whether the expansion is legitimate near the origin (where many density distributions commonly considered are singular). Therefore, one should always check that the derived pairs satisfy the Poisson equation.

A.1.2 Expansion at fixed total mass

Suppose that the density ρ is characterized by finite total mass

$$M = 4\pi abc\rho_0\mathcal{M}, \quad \mathcal{M} \equiv \int_0^{\infty} \tilde{\rho}(m)m^2\, dm. \quad \text{(A.12)}$$

In this case we can rewrite the density and the potential in a convenient form:

$$\rho(\mathbf{x}) = \frac{M}{4\pi a^3\mathcal{M}} \frac{\tilde{\rho}(m)}{(1-\epsilon)(1-\eta)}, \quad \text{(A.13)}$$

$$\phi(\mathbf{x}) = \frac{GM}{a\mathcal{M}} \frac{\tilde{\phi}}{(1-\epsilon)(1-\eta)}, \tag{A.14}$$

where $\tilde{\phi}$ is again given by Equation (A.8). A procedure similar to that followed in Section A.1.1 gives to first order:

$$\frac{\tilde{\rho}(m)}{(1-\epsilon)(1-\eta)} = (1+\epsilon+\eta)\tilde{\rho}(\tilde{r}) + \frac{\epsilon\tilde{y}^2 + \eta\tilde{z}^2}{\tilde{r}}\tilde{\rho}'(\tilde{r}) + O(\epsilon^2+\eta^2), \tag{A.15}$$

$$\frac{\tilde{\phi}}{(1-\epsilon)(1-\eta)} = \tilde{\phi}_0(\tilde{r}) + (\epsilon+\eta)\tilde{\phi}_1(\tilde{r}) + (\epsilon\tilde{y}^2+\eta\tilde{z}^2)\tilde{\phi}_2(\tilde{r}) + O(\epsilon^2+\eta^2). \tag{A.16}$$

At variance with the unconstrained expansion, the mass of the density in Equation (A.15), truncated to first order in ϵ and η, is the same as in the full Equation (A.13), as can be proved by direct expansion of its volume integral. In fact, because, by construction, the total mass is kept constant for any choice of (ϵ, η), the integral of the zeroth-order expansion (i.e., the spherical limit) must be equal to the total mass. This implies that the volume integral of *each* element of the asymptotic expansion (in powers of the flattening parameters), beyond the zeroth order, vanishes. This property is reminiscent of an analogous property characterizing expansions in spherical harmonics (see CB05, for a complete discussion of this topic).

Obviously, only finite-mass systems can be expanded at fixed total mass; in turn, the unconstrained expansion described in Section A.1.1 can be applied to all homeoidal systems.

A.1.3 Generating new families of non-spherical density-potential pairs

The calculations presented in the previous Sections are not new. In contrast, the following consequences appear to have gone unnoticed.

First of all, we note that several families of non-spherical density-potential pairs can be obtained from Equations (A.9)-(A.10) (or Equations [A.15]-[A.16]). By ordering arguments and by the linearity of the Poisson equation, it follows that the truncation of Equations (A.9)-(A.10) (or Equations [A.15]-[A.16]) to first order[1] in the flattening parameters produces

---

[1] In principle, the method described below could be applied to generate additional, more complex density-potential pairs by moving to next order terms in the expansion of the Poisson equation.

exact density-potential pairs independently of the value of ϵ and η. In order to be physically acceptable, the density distribution truncated to first order in ϵ and η must be positive definite. This latter requirement is not always met for finite values of ϵ and η, because $\tilde{\rho}'$ is generally negative. A quantitative criterion for the selection of the acceptable values of the flattening parameters is presented in CB05. Density-potential pairs belonging to the families thus constructed can be non-spherical at the "non-linear" level, because the values of the flattening parameters can differ significantly from zero. On the other hand, the truncated potential is also the *approximate* potential for the density in Equation (A.1) (or Equation [A.13]) when $\epsilon \to 0$ and $\eta \to 0$.

Now we proceed one step further and use Equations (A.9)-(A.10) to construct new interesting density-potential pairs, *independent of the ellipticities ϵ and η* defining the homeoidal expansion. In fact, by the same ordering argument used above, it is immediate to see that $\tilde{\phi}_1(\tilde{r}) - \tilde{\phi}_0(\tilde{r}) + \tilde{z}^2\tilde{\phi}_2(\tilde{r})$ is the potential associated with the "density" $\tilde{z}^2\tilde{\rho}'(\tilde{r})/\tilde{r}$. For radially declining density distributions $\tilde{\rho}(\tilde{r})$, we can thus consider the (dimensionless) pair

$$\varrho = \tilde{z}^2 \frac{|\tilde{\rho}'(\tilde{r})|}{\tilde{r}}; \quad \Phi = \tilde{\phi}_0 - \tilde{\phi}_1 - \tilde{z}^2\tilde{\phi}_2. \tag{A.17}$$

Note that such a pair does not contain η anymore! Two similar density-potential pairs can be then obtained trivially by renaming variables, i.e., by replacing $\tilde{z}$ with $\tilde{y}$ or $\tilde{x}$ in Equation (A.17). We now combine the three density-potential pairs linearly to get the following generally "triaxial" solution

$$\varrho = (\alpha\tilde{x}^2 + \beta\tilde{y}^2 + \gamma\tilde{z}^2)\frac{|\tilde{\rho}'(\tilde{r})|}{\tilde{r}}, \tag{A.18}$$

$$\Phi = (\alpha + \beta + \gamma)[\tilde{\phi}_0(\tilde{r}) - \tilde{\phi}_1(\tilde{r})] - (\alpha\tilde{x}^2 + \beta\tilde{y}^2 + \gamma\tilde{z}^2)\tilde{\phi}_2(\tilde{r}). \tag{A.19}$$

As special cases of the above equations we can derive two different density-potential pairs characterized by axial symmetry. The first family is characterized by $\alpha = \beta = 0$ and $\gamma = 1$ (thus reducing to Equation [A.17]), while the other by the condition $\alpha = \beta = 1$ and $\gamma = 0$, and so it is given by

$$\varrho = \tilde{R}^2 \frac{|\tilde{\rho}'(\tilde{R})|}{\tilde{R}}; \quad \Phi = 2(\tilde{\phi}_0 - \tilde{\phi}_1) - \tilde{R}^2\tilde{\phi}_2, \tag{A.20}$$

where $\tilde{R} \equiv \sqrt{\tilde{x}^2 + \tilde{y}^2}$ is the dimensionless cylindrical radius. In Equation (A.17) the density vanishes on the equatorial plane, while in Equation (A.20) the density vanishes on the z axis. This latter family is more interesting, because the associated density distributions are characterized by toroidal geometry.

We conclude this Section by pointing out that the fact that Equations (A.17)-(A.20) indeed identify explicit density-potential pairs can be checked *a posteriori* by deriving the potential Φ from the density ϱ by means of a standard expansion in spherical harmonics (see CB05). However, without the insight provided by the explicit homeoidal relations, the existence of an analytical solution of this type would have been unexpected. If we started with a seemingly simpler idea, i.e., to transform the density in Equation (A.1) in spherical coordinates and then to expand it in spherical harmonics, we would have discarded all the expansion terms above the monopole as candidates for acceptable density distributions because the related mass vanishes (as in the case presented in Section A.1.2). In contrast, the present method works because, at least to first order, it is possible to isolate a density term with *constant* (in our case, negative) sign over all the space.

A.2 The Jeans equations of stellar dynamics for axisymmetric density-potential pairs (embedded, if desired, in a spherical external field)

In this Section, in view of applications to galactic dynamics, we study the Jeans equations for axisymmetric density-potential pairs either in the form of Equations (A.17) and (A.20), or in the axisymmetric cases of Equations (A.9)-(A.10) and (A.15)-(A.16) (we recall that in these latter cases $\epsilon = 0$ and $\epsilon = \eta$ describe *oblate* and *prolate* ellipsoidal systems, respectively). In our study we can also include the case in which the density distributions mentioned above are added to a separate spherically symmetric density distribution. In the following, we will assume that the resulting ϱ is positive definite.

In all the axisymmetric cases described above, the pair (ϱ, Φ) belongs to the general family of density-potential pairs

$$\rho_{[R]} = A(r) + R^2 B(r), \quad \phi_{[R]} = C(r) + R^2 D(r), \tag{A.21}$$

where the subscript $[R]$ means that the pair is made explicit with respect to R by using (if required) the identity $z^2 = r^2 - R^2$. As will be clear in the following, the possibility to switch to an alternative representation (i.e., from $\rho_{[R]}$ and $\phi_{[R]}$ to $\rho_{[z]}$ and $\phi_{[z]}$) is useful for the solution of the Jeans equations (when no subscript appears, it means that either form can be considered). Note that for $D(r) \propto 1/r^4$ the potential belongs to the class of Stäckel potential (Stäckel 1890).

Let us assume that the density-potential pair defines the equilibrium configuration of a stellar dynamical system for which the underlying distribution function f depends on the two classical integrals E and J_z (star energy and z-component of the angular momentum, per unit mass), so that the velocity dispersion tensor σ_{ij} is diagonal and $\sigma_{RR} = \sigma_{zz}$; for simplicity, we will denote this dispersion by σ^2, and by σ_φ^2 the dispersion $\sigma_{\varphi\varphi}$. Along the azimuthal direction, part of the kinetic energy can be stored in systematic motions[2], so that $\overline{v_\varphi^2} = u_\varphi^2 + \sigma_\varphi^2$. Therefore, the relevant Jeans equations can be written as :

$$\frac{\partial \rho\sigma^2}{\partial z} = -\rho \frac{\partial \phi}{\partial z}, \tag{A.22}$$

and

$$\frac{\partial \rho\sigma^2}{\partial R} - \rho \frac{\overline{v_\varphi^2} - \sigma^2}{R} = -\rho \frac{\partial \phi}{\partial R}. \tag{A.23}$$

The natural boundary condition for Equation (A.22) is $\rho\sigma^2 \to 0$ for $z \to \infty$. For an assigned pair (ρ, ϕ) these equations allow us to derive the related kinematical quantities $(\overline{v_\varphi^2}, \sigma^2)$.

Given the form of the density-potential pair in Equation (A.21), Equation (A.22) can be solved by changing integration variable from z to r (at

---

[2] As usual, a bar over a quantity means average over phase-space velocities. In particular, $u_\varphi \equiv \overline{v_\varphi} = \int f v_\varphi \, d^3\mathbf{v}/\rho$.

fixed R), thus obtaining

$$\rho\sigma^2 = \int_z^\infty \rho \frac{\partial\phi}{\partial z'}\, dz' = \int_r^\infty \rho_{[R]} \frac{\partial\phi_{[R]}}{\partial r'}\, dr'. \tag{A.24}$$

Usually, for simple density distributions, the integral can be expressed in closed form. The second of the Jeans equations is then solved by differentiation with respect to R (at fixed z):

$$\rho\,(\overline{v_\varphi^2} - \sigma^2) = R\left(\frac{\partial\rho\sigma^2}{\partial R} + \rho\frac{\partial\phi}{\partial R}\right) = \frac{R^2}{r}\left[\frac{\partial(\rho\sigma^2)_{[z]}}{\partial r} + \rho\frac{\partial\phi_{[z]}}{\partial r}\right]. \tag{A.25}$$

Clearly an ambiguity remains as to the amount of support related to systematic motions with respect to that of random motions in the toroidal direction. A commonly used decomposition assumes (Satoh 1980)

$$u_\varphi^2 \equiv k^2(\overline{v_\varphi^2} - \sigma^2), \tag{A.26}$$

and so

$$\sigma_\varphi^2 = \sigma^2 + (1-k^2)(\overline{v_\varphi^2} - \sigma^2). \tag{A.27}$$

In the above decomposition, k is generally taken to be a given constant (but see Ciotti & Pellegrini 1996). When $k = 0$ the system is azimuthally supported only by velocity dispersion, and no net rotation is present; in the opposite limit, $k = 1$, the velocity dispersion is isotropic. Of course, the above procedure can be applied only when $\overline{v_\varphi^2} - \sigma^2$ is everywhere a positive quantity. Unfortunately, no physical justification is available to tell a priori for which density-potential pairs this requirement is met.

A.2.1 Scale-free oblate axisymmetric systems treated in terms of the Jeans equations and the Satoh decomposition

We now apply the formulae derived in Section A.1.1 to the family of power-law oblate ($\epsilon = 0$) spheroids. Thus, we go back to Equation (A.1) and start from

$$\rho = \frac{\rho_0}{m^\gamma}, \quad 0 < \gamma < 3; \tag{A.28}$$

where the range of γ is such that the density profile is radially decreasing and the central mass remains finite[3].

Several properties of these models have been investigated by Qian et al. (1995), who reconstructed their phase-space properties; in addition, Evans (1994) and Evans & de Zeeuw (1994) studied the observational properties that would result from a decomposition similar (but not identical) to the Satoh (1980) decomposition for a similar class of models (which they called "power-law" models, in their scale-free limit).

Here we study the relevant Jeans equations on the basis of the Satoh decomposition, which has found widespread applications to elliptical galaxies (e.g. Binney et al. 1990; van der Marel et al. 1990; van der Marel 1991). We are then able to provide expressions for the intrinsic and projected kinematical profiles in a form that may be useful to model the observations. These expressions can be easily generalized to the case in which a central black hole or a power-law dark matter halo with different flattening are present. One motivation for this analysis goes back to the work of Lanzoni & Ciotti (2003), where it was shown that for flat Ferrers density distributions the presence or absence of rotation has little effect on the observed "central" velocity dispersion (see also van Albada et al. 1995).

From Equations (A.9)-(A.10) we have (the arguments described in CB05 impose $\eta \leq 1/\gamma$):

$$\varrho = \frac{1-\gamma\eta}{\tilde{r}^{\gamma}} + \frac{\gamma\eta\tilde{r}^2}{\tilde{r}^{\gamma+2}}, \tag{A.29}$$

$$\Phi = \begin{cases} -\dfrac{5-\gamma-(4-\gamma)(\gamma-1)\eta}{(5-\gamma)(3-\gamma)(\gamma-2)\tilde{r}^{\gamma-2}} - \dfrac{\eta\tilde{r}^2}{(5-\gamma)\tilde{r}^{\gamma}}, & (\gamma \neq 2) \\[2ex] \dfrac{(3-2\eta)\ln\tilde{r}}{3} - \dfrac{\eta\tilde{r}^2}{3\tilde{r}^2}, & (\gamma = 2). \end{cases} \tag{A.30}$$

The presence of a central black hole of mass $M_{\rm BH}$ can be modeled in Equation (A.30) by adding a term $-\mu_{\rm BH}/\tilde{r}$, where $\mu_{\rm BH} \equiv M_{\rm BH}/4\pi\rho_0 a^3$. The density in Equation (A.29) becomes prominently peanut-shaped at high values of η; this is a common property of density distributions built with the

---

[3] The present models provide a simple description of the central regions of the more general γ-models (see also Appendix A).

Schwarzschild (1979) method, of the flattened Plummer sphere (Lynden-Bell 1962), and of the family of "power-law" models (Evans 1994; the family includes the Binney (1981) logarithmic potential as a special case).

For $\gamma > 2$ the potential vanishes at infinity and is negative divergent at the origin. For $0 < \gamma \leq 2$ an upper truncation must be applied to some integrals appearing in Equation (A.11); in Equation (A.30) an additive constant has then been set to zero, so that the potential diverges at infinity and vanishes at the origin. Finally, for $\gamma = 2$ the model is characterized by a flat rotation curve, as the seed density distribution. In fact,

$$v_{\rm c}^2 = \frac{5-\gamma-2\eta}{(5-\gamma)(3-\gamma)\tilde{r}^{\gamma-2}} + \frac{\mu_{\rm BH}}{\tilde{r}}. \tag{A.31}$$

In the entire range $0 < \gamma < 3$ are physically acceptable.

The fully nonlinear (i.e., up to η^2 terms included) Jeans equations (A.22)-(A.23) for the assumed density–potential pair can be solved without difficulty. Here, for simplicity, we use the solution up to first order in η; the analytical expressions of the intrinsic and (edge-on) projected kinematical fields are given in Section A.2.2. In Section A.2.2 we also show that the projection of all the quadratic (intrinsic) kinematical profiles can be obtained explicitly even for $\mu_{\rm BH} \neq 0$; unfortunately, the streaming velocity field cannot be obtained in explicit form when $\mu_{\rm BH} \neq 0$, for this case we can only provide asymptotic expressions for small values of the projected radius. Close to the origin, independently of the value of γ, the dynamical effects of $\mu_{\rm BH}$ are always dominant.

For $\mu_{\rm BH} = 0$, the analysis presented in Section A.2.2 gives (for $3/2 < \gamma < 5/2$)

$$\begin{aligned} M_{\rm p}\,\sigma_{\rm ap}^2 = {} & \frac{\pi^{3/2}\Gamma(\gamma-3/2)\,\tilde{\ell}^{5-2\gamma}}{2(5-\gamma)(3-\gamma)(5-2\gamma)\Gamma(\gamma)} \times \\ & \bigg[2(5-\gamma) + \eta(2\gamma^2 - 7\gamma - 2) \\ & - \frac{4k^2\eta\Gamma^2(3\gamma/4-1/2)\Gamma(\gamma/2)\Gamma(\gamma)}{\Gamma^2(3\gamma/4)\Gamma(\gamma/2-1/2)\Gamma(\gamma-3/2)} \bigg], \end{aligned} \tag{A.32}$$

where $\tilde{\ell} \equiv \sqrt{\tilde{y}^2 + \tilde{z}^2}$ is the (dimensionless) circular aperture radius and Γ is the standard Euler gamma function.

For $\mu_{\mathrm{BH}} \neq 0$ and $l \to 0$ (that is in practice, for apertures not larger than the sphere of influence of the black hole)

$$\begin{aligned} M_{\mathrm{p}}\,\sigma^2_{\mathrm{ap}} = {} & \frac{\mu_{\mathrm{BH}}\pi^{3/2}\Gamma(\gamma/2+1)\,\tilde{\ell}^{2-\gamma}}{2\gamma(2-\gamma)\Gamma(\gamma/2+5/2)}\times \\ & \Bigg[2(3+\gamma)-\gamma(4-\gamma)\eta \\ & - \frac{k^2\eta\gamma(\gamma^2-1)\Gamma^2(\gamma+1/4)}{\Gamma^2(\gamma/2+3/4)}\Bigg], \end{aligned} \tag{A.33}$$

for $1 < \gamma < 2$. Thus, scale-free oblate systems with a central black hole do have finite projected fields in the range $3/2 < \gamma < 2$. In Equations (46)-(47) σ^2_{ap} is the *aperture velocity dispersion* defined as

$$\sigma^2_{\mathrm{ap}}(\ell) \equiv \int_{y^2+z^2\leq \ell^2} \Sigma\sigma^2_{\mathrm{los}} dydz/M_{\mathrm{p}}(\ell), \tag{A.34}$$

where $M_{\mathrm{p}}(\ell)$ is the projected mass within ℓ.

By combining the two formulae above we obtain an expression for the aperture velocity dispersion which is asymptotically correct for small and large apertures when $\mu_{\mathrm{BH}} \neq 0$. Note also, from Equations (A.31)-(A.33) that the definition of the "sphere of influence" of the black hole depends on the quantity that one is referring to, for example the circular velocity or the aperture velocity dispersion.

A.2.2 Solutions of the Jeans equations for low-flattening, scale-free axisymmetric models

Here we record the expressions for the intrinsic and projected kinematical profiles associated with the density profile in Equation (A.29), derived from the Jeans equations of a two-integral model. We adopt the same normalization procedure mentioned at the beginning of Section.

We first note that for $\gamma > 1$ the edge-on projected density ("surface brightness") is

$$\Sigma = \frac{\sqrt{\pi}\,\Gamma(\gamma/2-1/2)}{\Gamma(\gamma/2)\tilde{\ell}^{\gamma-1}}\left[1-\frac{(\gamma-1)\eta\tilde{z}^2}{\tilde{\ell}^2}\right] \tag{A.35}$$

and the mass ("integrated luminosity") contained within the projected radius $\ell = \sqrt{y^2+z^2}$ is

$$M_{\rm p} = \frac{\pi^{3/2}(2+\eta-\gamma\eta)\Gamma(\gamma/2-1/2)}{(3-\gamma)\Gamma(\gamma/2)}\tilde{\ell}^{3-\gamma}. \tag{A.36}$$

Integration of Equation (A.24), truncated to first order in η, gives

$$\begin{aligned}\varrho\sigma^2 = {} & \frac{1}{(5-\gamma)(3-\gamma)\,\tilde{r}^{2(\gamma-1)}}\left[\frac{5-\gamma-4\eta}{2(\gamma-1)} - \frac{(4-\gamma)\eta\tilde{z}^2}{\tilde{r}^2}\right] \\ & + \frac{\mu_{\rm BH}}{(3+\gamma)\,\tilde{r}^{1+\gamma}}\left(\frac{3+\gamma-2\gamma\eta}{1+\gamma} - \frac{\gamma\eta\tilde{z}^2}{\tilde{r}^2}\right).\end{aligned} \tag{A.37}$$

Similarly, from Equation (A.25),

$$\varrho(\overline{v_\varphi^2}-\sigma^2) = \frac{2\eta\tilde{r}^2}{\tilde{r}^{2\gamma}}\left[\frac{1}{(5-\gamma)(3-\gamma)} + \frac{\gamma\mu_{\rm BH}}{(3+\gamma)\tilde{r}^{3-\gamma}}\right]. \tag{A.38}$$

Therefore, for spherical systems ($\eta = 0$), the quantity above vanishes. Finally, to leading order in η

$$\varrho u_\varphi = \sqrt{\varrho \times \varrho u_\varphi d} \sim \frac{k\sqrt{2\eta}\tilde{r}}{\tilde{r}^{3\gamma/2}}\sqrt{\frac{1}{(5-\gamma)(3-\gamma)} + \frac{\gamma\mu_{\rm BH}}{(3+\gamma)\tilde{r}^{3-\gamma}}}. \tag{A.39}$$

The relevant projected kinematical quantities are obtained from the formulae described in Section A.2. Accordingly,

$$\Sigma V_{\rm p}^2 = \frac{2\eta k^2\sqrt{\pi}\tilde{y}^2}{\tilde{\ell}^{2\gamma-1}}\left[\frac{\Gamma(\gamma-1/2)}{(5-\gamma)(3-\gamma)\Gamma(\gamma)} + \frac{\gamma\mu_{\rm BH}}{\tilde{\ell}^{3-\gamma}}\frac{\Gamma(\gamma/2+1)}{2\Gamma(\gamma/2+5/2)}\right], \tag{A.40}$$

and, for $\gamma > 3/2$,

$$\begin{aligned}\Sigma\sigma_{\rm p}^2 = {} & \frac{\sqrt{\pi}\Gamma(\gamma-1/2)}{(5-\gamma)(3-\gamma)\Gamma(\gamma)\tilde{\ell}^{2\gamma-3}}\left[\frac{5-\gamma-4\eta}{2\gamma-3} - \frac{(4-\gamma)\eta\tilde{z}^2}{\tilde{\ell}^2}\right] \\ & + \frac{\mu_{\rm BH}\sqrt{\pi}\Gamma(\gamma/2+1)}{2\Gamma(\gamma/2+5/2)\tilde{\ell}^{\gamma}}\left(\frac{3+\gamma-2\gamma\eta}{\gamma} - \frac{\gamma\eta\tilde{z}^2}{\tilde{\ell}^2}\right) + \frac{1-k^2}{k^2}\Sigma V_{\rm p}^2.\end{aligned} \tag{A.41}$$

Unfortunately, when $\mu_{\rm BH} \neq 0$ no explicit expression is available for the quantities $\Sigma u_{\rm p}$ and $\Sigma u_{\rm p}^2$. This latter quantity is obtained by expanding to lowest order in η the function $(\Sigma u_{\rm p})^2/\Sigma$. In two interesting cases, namely when $\mu_{\rm BH} = 0$ and when $\mu_{\rm BH} \neq 0$ and $\ell \to 0$, asymptotic expressions can be obtained from the projection integral by substituting $\tilde{x}^2 = \tilde{r}^2 - \tilde{\ell}^2$ and then by changing the integration variable to $\tilde{r}/\tilde{\ell}$. One then finds

$$\Sigma u_{\rm p} = -\begin{cases} \dfrac{\sqrt{2\pi\eta}k\tilde{y}}{\tilde{\ell}^{3\gamma/2-1}} \dfrac{\Gamma(3\gamma/4 - 1/2)}{\sqrt{(5-\gamma)(3-\gamma)}\Gamma(3\gamma/4)}, & (\mu_{\rm BH} = 0); \\ \dfrac{\sqrt{2\pi\eta\mu_{\rm BH}}k\tilde{y}}{\tilde{\ell}^{\gamma+1/2}} \dfrac{\sqrt{\gamma}\Gamma(\gamma/2 + 1/4)}{\sqrt{3+\gamma}\Gamma(\gamma/2+3/4)}, & (\mu_{\rm BH} \neq 0,\ \tilde{\ell} \to 0), \end{cases} \tag{A.42}$$

and

$$\Sigma u_{\rm p}^2 = \begin{cases} \dfrac{2\sqrt{\pi}\eta k^2\tilde{y}^2}{\tilde{\ell}^{2\gamma-1}} \times \\ \dfrac{\Gamma^2(3\gamma/4-1/2)\Gamma(\gamma/2)}{(5-\gamma)(3-\gamma)\Gamma^2(3\gamma/4)\Gamma(\gamma/2-1/2)}, \ (\mu_{\rm BH} = 0); \\ \dfrac{2\sqrt{\pi}\eta\mu_{\rm BH}k^2\tilde{y}^2}{\tilde{\ell}^{2+\gamma}} \times \\ \dfrac{\gamma\Gamma^2(\gamma/2+1/4)\Gamma(\gamma/2)}{(3+\gamma)\Gamma^2(\gamma/2+3/4)\Gamma(\gamma/2-1/2)}, \ (\mu_{\rm BH} \neq 0,\ \tilde{\ell} \to 0). \end{cases} \tag{A.43}$$

Near the origin, the black hole contribution to the various intrinsic and projected fields dominates for any value of γ.

Appendix B

A simple, analytical cuspy axisymmetric galaxy model with dark matter halo and central BH

As an application of the homeoidal expansion technique, described in Appendix A, we present here the internal kinematical fields of a simple family of oblate axisymmetric galaxy models with dark matter halo and central black hole (see Ciotti & Bertin 2005, for a complete discussion of the topic). The seed distributions for stars and dark matter are:

$$\rho_* = \frac{\rho_{*0}}{m_*^{\gamma}} \,, \tag{B.1}$$

and

$$\rho_h = \frac{\rho_{h0}}{m_h^{\delta}} \,, \tag{B.2}$$

where $m_*^2 \equiv \tilde{R}^2 + \tilde{z}^2/q_*^2$, $m_h^2 \equiv \tilde{R}^2 + \tilde{z}^2/q_h^2$, and, without loss of generality the scale length of both distributions is r_c. The flattenings are $q_* \equiv 1 - \eta$ and $q_h \equiv 1 - \nu$, and, according to the results found by Ciotti & Bertin (2005), the *unconstrained* expansion is performed for $\eta \leq 1/\gamma$, $\nu \leq 1/\delta$, with $\gamma\,,\delta > 1$. Note that similar two-component *gaseous* models have been also constructed in a different context, by Barnabè et al. (2005), while a model as in Equation (B.1) with a central BH has been already presented in Appendix A. Here, as in the previous Appendix, we restrict to first order terms in the flattening. The explicit expression of the potential expansion has been already given in Appendix A.1, here we just recall that the total potential can be written as:

$$\phi = \widetilde{\phi}_* + \mathcal{R}\widetilde{\phi}_h - \frac{\mu}{\tilde{r}}\,, \tag{B.3}$$

where potentials and square velocities are normalized to $4\pi G\rho_{*0}r_c^2$, all scale length are intended normalized to r_c, the mass of the black hole is $\mu \equiv M_{\rm BH}/4\pi\rho_{*0}r_c^3$, and $\mathcal{R} \equiv \rho_{h0}/\rho_{*0}$. After density and potential expansion, and integration of the Jeans equations we obtain for the stellar component:

$$\begin{aligned} v_c^2 = R\frac{d\phi}{dR} = &- R^2\left[\frac{\gamma+2\eta-5}{R^\gamma\,(\gamma-5)(\gamma-3)}\right.\\ &\left.+\,\mathcal{R}\,\frac{\delta+2\nu-5}{R^\delta\,(\delta-5)(\delta-3)}\right] + \frac{\mu}{R} \end{aligned} \tag{B.4}$$

$$\begin{aligned} \rho\sigma_R^2 = &- \frac{1}{r^{2\gamma}}\left[R^2\,\frac{(\gamma-4)\eta}{(\gamma-5)(\gamma-3)}\right.\\ &\left.-\,r^2\,\frac{(2\eta\gamma-1)(\gamma-5)+4\eta}{2\,(\gamma-5)\,(\gamma-3)\,(\gamma-1)}\right]\\ &+\frac{\mathcal{R}}{r^{\gamma+\delta}}\left[r^2\frac{(\delta-4)(\delta-1)\nu+(\gamma\eta-1)(\delta-5)}{(\delta-5)(\delta-3)(\gamma+\delta-2)}\right.\\ &\left.-\,R^2\frac{\delta\nu(\delta-3)+\gamma\eta(\delta-5)}{(\delta-5)(\delta-3)(\gamma+\delta)}\right]\\ &+\frac{\mu}{r^{\gamma+3}}\left[R^2\,\frac{\gamma\eta}{\gamma+3}-r^2\,\frac{\gamma\eta-1}{\gamma+1}\right] \end{aligned} \tag{B.5}$$

$$\begin{aligned} \rho\left(\overline{v_\varphi^2}-\sigma_R^2\right) = &\,\frac{R^2}{r^{2\gamma}}\,\frac{2\eta}{(\gamma-5)(\gamma-3)}\\ &-\mathcal{R}\,\frac{2\gamma R^2}{r^{\gamma+\delta}}\,\frac{\eta(\delta-5)-\nu(\delta-3)}{(\delta-5)(\delta-3)(\gamma+\delta)}\\ &+\mu\,\frac{R^2}{r^{\gamma+3}}\,\frac{2\gamma\eta}{(\gamma+3)}\,. \end{aligned} \tag{B.6}$$

Appendix C

Source code

As already described in Chapter 3, the code developed during this Thesis starts from a chosen density distribution which is axysimmetric and symmetric with respect to the equatorial plane, and solves the Poisson equation, the Jeans equations, and the projected dynamics integrations in order to derive the gravitational potential, the intrinsic, and projected dynamic fields, respectively. The flow-chart of the code is shown in Figure C.1. A complete run for a one-component model takes $\sim 10^2\,\mathrm{s}$ on a 1.33 GHz CPU, while for two-component models the time required increases by nearly 30%. Adding the central BH to both kind of models does not affect the execution time in a relevant way.

The code has been thought as a tool to study dynamics properties of any galaxy model whose density distribution satisfies the above symmetry constraints. Thus it has been developed to be flexible, accurate and as general as possible. The code has been written using ANSI C language, and relies on the LAPACK library (Anderson et al. 1999) for the solution of linear systems. All the computations are performed in double precision and the code is organized as a library of functions each solving a single task of the whole problem. In this way the code is lean and easy to maintain, and either it can be used as a whole, with many facilities that has been provided as a user-friendly interface, or it can be easily embedded in other codes as a library itself.

The code is quite complex and too long to be reported here entirely. Thus we present in the following an excerpt containing the most meaningful

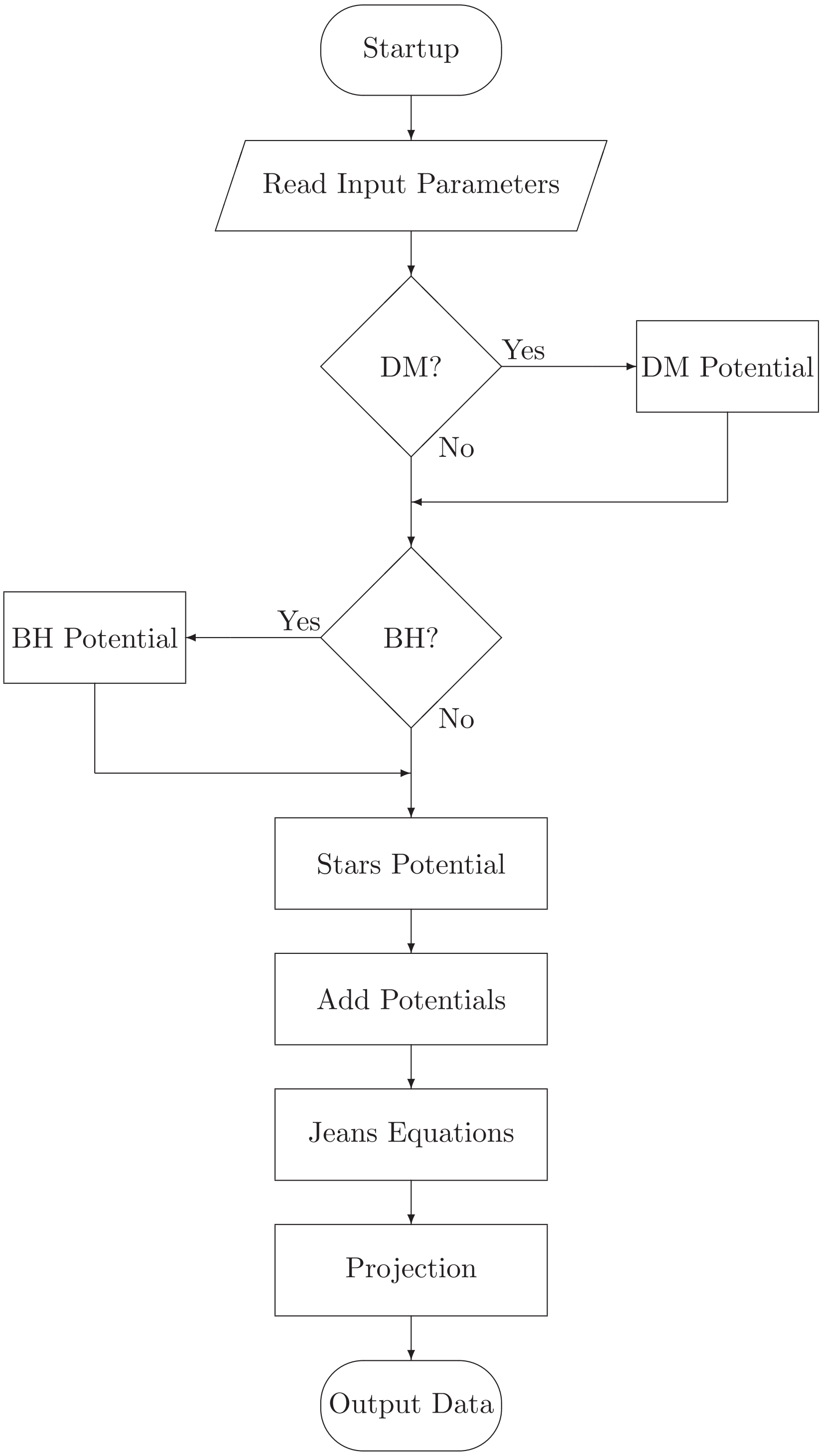

Figure C.1 – Code flow-chart.

parts of it. The complete distribution can be obtained contacting the author at his email address[1].

Some of the source files among which the code is split are reported below. A brief description of what these files contains follows:

my_gal.c Contains some utilities functions.

my_func.c Contains all the definitions for model density distributions, potential and velocity dispersion (when known).

my_spt.c Contains all the functions needed for the solution of the Poisson equation.

my_project.c Contains all the function needed for projected dynamics.

C.1 my_gal.c

```
#include "my_gal.h"

extern Array2d* set_map2D(Array1d *u, Array1d *v, Array1d *par, double
    (*f)(double, double, Array1d *))
{
  int i,j;
  int Nu, Nv;
  double y0;

  Array2d* map2D;

  Nu = u->nrows;
  Nv = v->nrows;

  map2D = new_Array2d(Nu, Nv);

  for (i = 0; i < Nu; i++) {
    y0 = u->a[i];
    for (j = 0; j < Nv; j++) {
      map2D->aa[i][j] = f(y0, v->a[j], par);
    }
  }

  return map2D;
}

```

---

[1] Author's email address: andrea.riciputi@bo.astro.it

```
extern Array1d* set_map1D(Array1d *u, Array1d *par, double (*f)(double
    , Array1d *))
{
  int i, Nu;

  Array1d* map1D;

  Nu = u->nrows;

  map1D = new_Array1d(Nu);

  for (i = 0; i < Nu; i++) {
    map1D->a[i] = f(u->a[i], par);
  }

  return map1D;
}

extern
Array2d*
multMaps(
          Array2d *x,
          Array2d *y)
{
  int i,j;

  int n1, n2;

  if ((x->nrows != y->nrows) || (x->ncols != y->ncols)) {
    return NULL;
  } else {
    n1 = x->nrows;
    n2 = x->ncols;
  }

  Array2d *result = new_Array2d(n1, n2);

  for(i = 0; i < n1; i++) {
    for(j = 0; j < n2; j++) {
      result->aa[i][j] = x->aa[i][j] * y->aa[i][j];
    }
  }

  return result;
}

extern
int
searchArray(
             Array1d *x,
```

```
               double x_bar)
{
  int i;
  int nx = x->nrows;

  int i_upper = nx - 1;
  int i_lower = 0;

  while (i_upper - i_lower > 1) {
    i = (i_upper + i_lower) / 2;

    if (x->a[i] > x_bar) {
      i_upper = i;
    } else if (x->a[i] <= x_bar) {
      i_lower = i;
    }
  }

  return i;
}
```

C.2 my_func.c

```
#include "my_func.h"

/* Hernquist oblate model */

extern double density_HO_cyl(double R, double zeta, Array1d *par)
{
  double q = par->a[0];
  double a = par->a[1];
  double m;

  m = sqrt(R * R + (zeta * zeta) / (q * q)) / a;

  return 1. / (2. * M_PI * q * m * (1. + m) * (1. + m) * (1. + m));
}

extern double density_HO_sph(double r, double x, Array1d *par)
{
  double q = par->a[0];
  double a = par->a[1];
  double elipt;

  elipt = sqrt(1. - x*x * (1. - 1./ (q*q))) / a;

  return 1. / (2. * M_PI * q * r * elipt *
               (1. + r*elipt) * (1. + r*elipt) * (1. + r*elipt));
}
```

```
/* Jaffe oblated model */

extern double density_Jaffe_cyl(double R, double zeta, Array1d *par)
{
  double qq = par->a[0] * par->a[0];

  return 1. / (1. + (R * R + zeta * zeta / (qq)) * (R * R + zeta *
      zeta / (qq)));
}

extern double density_Jaffe_sph(double r, double x, Array1d *par)
{
  const double x_square = x * x;
  const double r_quad = r * r * r * r;
  const double q_square = par->a[0] * par->a[0];

  return 1. / (1. + r_quad *
               (1. - x_square + (x_square / q_square)) *
               (1. - x_square + (x_square / q_square)));
}

/* Miyamoto-Nagai models */

extern double density_MN_cyl(double R, double z, Array1d *par)
{
  const double RR = R*R;
  const double s = par->a[0];
  const double eta = sqrt(1. + z * z);
  const double s_eta_sq = (s + eta) * (s + eta);
  const double R_s_eta = sqrt((RR + s_eta_sq) * (RR + s_eta_sq) *
                              (RR + s_eta_sq) * (RR + s_eta_sq) *
                              (RR + s_eta_sq));

  return (s * RR + (s + 3 * eta) * s_eta_sq) /
    (4. * M_PI * eta * eta * eta * R_s_eta);
}

extern double ddensity_dR_MN(double R, double z, Array1d *par)
{
  const double RR = R*R;
  const double s = par->a[0];
  const double eta = sqrt(1. + z * z);
  const double s_eta_sq = (s + eta) * (s + eta);
  const double R_s_eta = sqrt((RR + s_eta_sq) * (RR + s_eta_sq) *
                              (RR + s_eta_sq) * (RR + s_eta_sq) *
                              (RR + s_eta_sq) * (RR + s_eta_sq) *
                              (RR + s_eta_sq));

  return - (3.*R * (RR * s + s_eta_sq * (s + 5. * eta))) /
```

```
    (4. * M_PI * eta * eta * eta * R_s_eta);
}

extern double ddensity_dz_MN(double R, double z, Array1d *par)
{
  const double RR = R*R;
  const double s = par->a[0];
  const double ss = s*s;
  const double eta = sqrt(1. + z * z);
  const double etaeta = eta*eta;
  const double s_eta_sq = (s + eta) * (s + eta);
  const double R_s_eta = sqrt((RR + s_eta_sq) * (RR + s_eta_sq) *
                              (RR + s_eta_sq) * (RR + s_eta_sq) *
                              (RR + s_eta_sq) * (RR + s_eta_sq) *
                              (RR + s_eta_sq));

  return - (3.*z * (RR*RR * s + s_eta_sq * (s + eta) *
                    (ss + 4.*s*eta + 5.*etaeta)
                    + RR*s*(2.*ss + 7.*s*eta + 5*etaeta))) /
    (4. * M_PI * etaeta*etaeta*eta * R_s_eta);
}

extern double density_MN_sph(double r, double x, Array1d *par)
{
  const double s = par->a[0];
  const double R = r * sqrt(1. - x * x);
  const double RR = R*R;
  const double z = r * x;
  const double eta = sqrt(1. + z * z);
  const double s_eta_sq = (s + eta) * (s + eta);
  const double R_s_eta = sqrt((RR + s_eta_sq) * (RR + s_eta_sq) *
                              (RR + s_eta_sq) * (RR + s_eta_sq) *
                              (RR + s_eta_sq));

  return (s * RR + (s + 3 * eta) * s_eta_sq) /
    (4. * M_PI * eta * eta * eta * R_s_eta);
}

extern double dev_density_MN_sph(double r, double x, Array1d *par)
{
  const double s = par->a[0];
  const double jac_R = sqrt(1. - x * x);
  const double jac_z = x;
  const double R = r * jac_R;
  const double RR = R*R;
  const double z = r * x;

  const double eta = sqrt(1. + z * z);
  const double jac_eta = z / eta;
  const double eta2 = eta*eta;
```

```
  const double s_eta_sq = (s + eta) * (s + eta);
  const double R_s_eta = sqrt((RR + s_eta_sq) * (RR + s_eta_sq) *
                              (RR + s_eta_sq) * (RR + s_eta_sq) *
                              (RR + s_eta_sq) * (RR + s_eta_sq) *
                              (RR + s_eta_sq));

  const double drho_dR = -(3. * R * (RR * s + s_eta_sq *
                                     (s + 5. * eta))) /
    (4. * M_PI * eta2*eta * R_s_eta);

  const double drho_deta = -(3 * RR*RR * s + s_eta_sq * (s + eta)
                               * (s*s + 4.*s*eta + 5.*eta2)
                             + RR*s * (2.*s*s + 7.*s*eta + 5.*eta2))
    / (4. * M_PI * eta2*eta2 * R_s_eta);

  return drho_dR * jac_R + drho_deta * jac_eta * jac_z;
}

extern double potential_MN_cyl(double R, double z, Array1d *par)
{
  const double s = par->a[0];
  const double eta = sqrt(1. + z * z);

  return - 1. / sqrt(R * R + (s + eta) * (s + eta));
}

extern double potential_MN_sph(double r, double x, Array1d *par)
{
  const double s = par->a[0];
  const double rr = r * r;
  const double xx = x * x;
  const double eta = sqrt(1. + rr * xx);

  return - 1. / sqrt(rr * (1. - xx) + (s + eta) * (s + eta));
}

extern double dpot_dz_MN_cyl(double R, double z, Array1d *par)
{
  const double s = par->a[0];
  const double eta = sqrt(1. + z*z);
  const double s_eta = s + eta;
  const double R_s_eta = sqrt((R*R + s_eta*s_eta) *
                              (R*R + s_eta*s_eta) *
                              (R*R + s_eta*s_eta));

  return z * s_eta / (eta * R_s_eta);
}

extern double dpot_dR_MN_cyl(double R, double z, Array1d *par)
{
```

```
  const double s = par->a[0];
  const double eta = sqrt(1. + z*z);
  const double s_eta_sq = (s + eta) * (s + eta);
  const double R_s_eta = sqrt((R*R + s_eta_sq) *
                              (R*R + s_eta_sq) *
                              (R*R + s_eta_sq));

  return R / R_s_eta;
}

extern double dpot_dr_MN_sph(double r, double x, Array1d *par)
{
  const double s = par->a[0];
  const double rr = r*r;
  const double xx = x*x;
  const double eta = sqrt(1. + rr*xx);
  const double r_s_eta = sqrt((1. + rr + s*s + 2.*s*eta) *
                              (1. + rr + s*s + 2.*s*eta) *
                              (1. + rr + s*s + 2.*s*eta));

  return (r * (s * xx + eta)) / (eta * r_s_eta);
}

extern double dpot_dx_MN_sph(double r, double x, Array1d *par)
{
  const double s = par->a[0];
  const double rr = r*r;
  const double xx = x*x;
  const double eta = sqrt(1. + rr*xx);
  const double r_s_eta = sqrt((1. + rr + s*s + 2.*s*eta) *
                              (1. + rr + s*s + 2.*s*eta) *
                              (1. + rr + s*s + 2.*s*eta));

  return (rr * s * x) / (eta * r_s_eta);
}

extern double disp_MN_z(double R, double z, Array1d *par)
{
  const double s = par->a[0];
  const double RR = R * R;
  const double eta = sqrt(1. + z * z);
  const double s_eta_sq = (s + eta) * (s + eta);

  return s_eta_sq / (8. * M_PI * eta * eta * (RR + s_eta_sq) *
                     (RR + s_eta_sq) * (RR + s_eta_sq));
}

extern double disp_MN_phi(double R, double z, Array1d *par)
{
  const double s = par->a[0];
```

```
  const double RR = R * R;
  const double eta = sqrt(1. + z * z);
  const double s_eta_sq = (s + eta) * (s + eta);

  return (s * RR) / (4. * M_PI * eta*eta*eta * (RR + s_eta_sq) *
                     (RR + s_eta_sq) * (RR + s_eta_sq));
}

extern double disp_MN_los(double R, double z, Array1d *par)
{
  const double s = par->a[0];
  const double k = par->a[1];
  const double RR = R * R;
  const double eta = sqrt(1. + z * z);
  const double s_eta_sq = (s + eta) * (s + eta);
  const double kk = k * k;

  return (3. /
          (32. * eta * eta * sqrt((RR + s_eta_sq) * (RR + s_eta_sq) *
                                  (RR + s_eta_sq) * (RR + s_eta_sq) *
                                  (RR + s_eta_sq)))) *
    (0.5 * s_eta_sq + (1 - kk) * s * RR / eta);
}

extern double v_MN_los(double R, double z, Array1d *par)
{
  const double s = par->a[0];
  const double k = par->a[1];
  const double RR = R * R;
  const double eta = sqrt(1. + z * z);
  const double s_eta_sq = (s + eta) * (s + eta);
  const double kk = k * k;

  return (3. * kk * s * RR) /
    (32. * eta*eta*eta * sqrt((RR + s_eta_sq) * (RR + s_eta_sq)*
                              (RR + s_eta_sq) * (RR + s_eta_sq)*
                              (RR + s_eta_sq)));
}

extern double Sigma_MN_los(double R, double z, Array1d *par)
{
  const double s = par->a[0];
  const double RR = R*R;
  const double eta = sqrt(1. + z*z);
  const double s_eta_sq = (s + eta) * (s + eta);

  return (s * RR + (s + 2. * eta) * s_eta_sq) /
    (2. * M_PI * eta*eta*eta * (RR + s_eta_sq)*(RR + s_eta_sq));
}

```

```
extern double Sigma_MN_los_sph(double r, double theta, Array1d *par)
{
  const double s = par->a[0];
  const double R = r * cos(theta);
  const double z = r * sin(theta);
  const double RR = R*R;
  const double eta = sqrt(1. + z*z);
  const double s_eta_sq = (s + eta) * (s + eta);

  return (s * RR + (s + 2. * eta) * s_eta_sq) /
    (2. * M_PI * eta*eta*eta * (RR + s_eta_sq)*(RR + s_eta_sq));
}

/* Gamma-models */

extern double density_gamma_cyl(double R, double z, Array1d *par)
{
  const double gamma = par->a[0];
  const double q = par->a[1];
  const double mu = sqrt(R*R + z*z / (q*q));

  return (3. - gamma) / (q * pow(mu,gamma) * pow(1. + mu, 4. - gamma))
      ;
}

extern double density_gamma_sph(double r, double cos_theta, Array1d *
    par)
{
  const double gamma = par->a[0];
  const double q = par->a[1];
  const double R = r * sqrt(1. - cos_theta * cos_theta);
  const double z = r * cos_theta;
  const double mu = sqrt(R*R + z*z / (q*q));

  return (3. - gamma) / (q * pow(mu,gamma) * pow(1. + mu, 4. - gamma))
      ;
}

extern double ddensity_dR_gamma(double R, double z, Array1d *par)
{
  const double gamma = par->a[0];
  const double q = par->a[1];
  const double mu = sqrt(R*R + z*z / (q*q));

  return -((3. - gamma) * R * (4. * mu + gamma)) /
    (q * pow(mu, gamma + 2.) * pow(1. + mu, 5. - gamma));
}

extern double ddensity_dz_gamma(double R, double z, Array1d *par)
{
```

```
  const double gamma = par->a[0];
  const double q = par->a[1];
  const double mu = sqrt(R*R + z*z / (q*q));

  return -((3. - gamma) * z * (4. * mu + gamma)) /
    (q*q*q * pow(mu, gamma + 2.) * pow(1. + mu, 5. - gamma));
}

/* Ferrers ellipsoid */

extern double density_ferrer_cyl(double R, double z, Array1d *par)
{
  const double gamma = par->a[0];
  const double q = par->a[1];

  const double mm = R*R + z*z / (q*q);

  if (mm >= 1.) {
    return 0.;
  } else {
    return pow(1. - mm, gamma);
  }
}

extern double density_ferrer_sph(double r, double cos_theta, Array1d *
    par)
{
  const double gamma = par->a[0];
  const double q = par->a[1];

  const double RR = r * r * (1. - cos_theta * cos_theta);
  const double zz = r * r * cos_theta * cos_theta;

  const double mm = RR + zz / (q*q);

  if (mm >= 1.) {
    return 0.;
  } else {
    return pow(1. - mm, gamma);
  }
}

extern double ddensity_dR_ferrer(double R, double z, Array1d *par)
{
  const double gamma = par->a[0];
  const double q = par->a[1];

  const double mm = R*R + z*z / (q*q);

  if (mm >= 1.) {
```

```
    return 0.;
  } else if (gamma == 1.) {
    return -2. * gamma * R;
  } else {
    return -2. * gamma * R * pow(1. - mm, gamma - 1);
  }
}

extern double ddensity_dz_ferrer(double R, double z, Array1d *par)
{
  const double gamma = par->a[0];
  const double q = par->a[1];
  const double qq = q * q;

  const double mm = R*R + z*z / (qq);

  if (mm >= 1.) {
    return 0.;
  } else if (gamma == 1.) {
    return -2. * gamma * z / qq;
  } else {
    return -2. * gamma * z * pow(1. - mm, gamma - 1) / qq;
  }
}

/* Power law homeoidal ellipsoid */

extern double density_hom_cyl(double R, double z, Array1d *par)
{
  const double gamma = par->a[0];
  const double q = par->a[1];
  const double mu = sqrt(R*R + z*z / (q*q));

  return 1. / pow(mu,gamma);
}

extern double density_hom_sph(double r, double cos_theta, Array1d *par
    )
{
  const double gamma = par->a[0];
  const double q = par->a[1];
  const double R = r * sqrt(1. - cos_theta * cos_theta);
  const double z = r * cos_theta;
  const double mu = sqrt(R*R + z*z / (q*q));

  return 1. / pow(mu,gamma);
}

extern double ddensity_dR_hom(double R, double z, Array1d *par)
{
```

```
  const double gamma = par->a[0];
  const double q = par->a[1];
  const double mu = sqrt(R*R + z*z / (q*q));

  return -(gamma * R) / pow(mu, gamma + 2.);
}

extern double ddensity_dz_hom(double R, double z, Array1d *par)
{
  const double gamma = par->a[0];
  const double q = par->a[1];
  const double mu = sqrt(R*R + z*z / (q*q));

  return -(gamma * z) / (q*q * pow(mu, gamma + 2.));
}
```

C.3 my_spt.c

```
#include "my_spt.h"

extern
Array2d*
SPT_exp_coef_gauss(
                   int Nu_gauss, int Nv_gauss,
                   int nmax, int lmax,
                   Array1d *par, double (*f_rho)(double, double,
                       Array1d*))
{
  int i,j,k,h,l,n;

  double Dtheta, Du;
  double v_norm, u_norm;
  double u_h, tg;
  double theta_i, cos_theta_i, sin_theta_i;
  double Pl;
  double kk, y0;
  double norm, rho_i, cos_ji;
  double cos_nu;

  double alpha, beta;
  double sin_i, cos_i;
  double sin_ip1, cos_ip1;

  Array1d *theta, *cos_theta;
  Array1d *u, *r;
  Array2d *rho, *AA, *BB, *rho_l, *rho_nl;

  if (Nv_gauss%2 != 0) {
    Nv_gauss += 1;
```

```
  }

  Nv_gauss /= 2;

  theta = new_Array1d(Nv_gauss);
  cos_theta = new_Array1d(Nv_gauss);

  u = new_Array1d(Nu_gauss);
  r = new_Array1d(Nu_gauss);

  rho = new_Array2d(Nu_gauss, Nv_gauss);
  AA = new_Array2d(lmax, lmax);
  BB = new_Array2d(lmax, lmax);
  rho_l = new_Array2d(Nu_gauss, lmax);
  rho_nl = new_Array2d(nmax, lmax);

  Dtheta = 0.5 * M_PI / Nv_gauss;
  Du = M_PI / Nu_gauss;

  v_norm = 2. / Nv_gauss;
  u_norm = 2. / Nu_gauss;

  alpha = sin(Dtheta * 0.5); alpha = 2. * alpha * alpha;
  beta = sin(Dtheta);

  theta->a[0] = theta_i = Dtheta * 0.5;
  cos_theta->a[0] = cos_i = cos(theta_i);
  sin_i = sin(theta_i);

  for(i = 1; i < Nv_gauss; i++) {
    theta->a[i] = theta_i = Dtheta * (i + 0.5);

    cos_theta->a[i] = cos_i - (alpha * cos_i + beta * sin_i);
    sin_i = sin_i - (alpha * sin_i - beta * cos_i);

    cos_i = cos_theta->a[i];
  }

  for(h = 0; h < Nu_gauss; h++) {
    u->a[h] = u_h = Du * (h + 0.5);
    tg = tan(0.5 * u_h);
    r->a[h] = tg * tg;
  }

  for(i = 0; i < Nv_gauss; i++) {
    theta_i = theta->a[i];
    cos_theta_i = cos_theta->a[i];

    sin_theta_i = sin(theta_i);
    alpha = 2. * sin_theta_i * sin_theta_i;
```

```
    beta = 2. * sin_theta_i * cos_theta_i;

    for(l = 0; l < lmax; l += 2) {
      Pl = LegendreP_check(cos_theta_i, l);
      for(k = 0, sin_i = 0., cos_i = 1.; k <= l; k += 2) {
        AA->aa[k][l] +=  v_norm * Pl * cos_i;

        cos_ip1 = cos_i - (alpha * cos_i + beta * sin_i);
        sin_ip1 = sin_i - (alpha * sin_i - beta * cos_i);

        cos_i = cos_ip1;
        sin_i = sin_ip1;
      }
    }
  }

  for(l = 0; l < lmax; l += 2) {
    AA->aa[0][l] *= 0.5;
  }

  for(k = 0; k < lmax; k += 2) {
    kk = (double) k*k;
    for(j = 0; j < lmax; j += 2) {
      BB->aa[k][j] = - 2. * (kk + j*j - 1) / ((j - k - 1) * (j - k +
          1) * (j + k - 1) * (j + k + 1));
    }
  }

  for(h = 0; h < Nu_gauss; h++) {
    y0 = r->a[h];
    for(i = 0; i < Nv_gauss; i++) {
      rho->aa[h][i] = y0 * y0 * f_rho(y0, cos_theta->a[i], par);
    }
  }

  for(h = 0; h < Nu_gauss; h++) {
    for(l = 0; l < lmax; l += 2) {
      norm = (2. * l + 1.) / Nv_gauss;
      for(i = 0; i < Nv_gauss; i++) {
        rho_i = rho->aa[h][i];
        theta_i = theta->a[i];

        alpha = 2. * sin(theta_i) * sin(theta_i);
        beta = sin(2. * theta_i);

        for(j = 0, sin_i = 0., cos_i = 1.; j < lmax; j += 2) {
          cos_ji = cos_i;
          if(j == 0) cos_ji *= 0.5;
          for(k = 0; k <= l; k += 2) {
            rho_l->aa[h][l] += rho_i * cos_ji * AA->aa[k][l] * BB->aa[
```

```
                k][j];
          }
          cos_ip1 = cos_i - (alpha * cos_i + beta * sin_i);
          sin_ip1 = sin_i - (alpha * sin_i - beta * cos_i);

          cos_i = cos_ip1;
          sin_i = sin_ip1;
        }
      }
      rho_l->aa[h][l] *= norm;
    }
  }

  for(h = 0; h < Nu_gauss; h++) {
    u_h = u->a[h];

    alpha = 2. * sin(u_h * 0.5) * sin(u_h * 0.5);
    beta = sin(u_h);

    for(n = 0, sin_i = 0., cos_i = 1.; n < nmax; n++) {
      cos_nu = cos_i;
      for(l = 0; l < lmax; l += 2) {
        rho_nl->aa[n][l] += u_norm * rho_l->aa[h][l] * cos_nu;
      }
      cos_ip1 = cos_i - (alpha * cos_i + beta * sin_i);
      sin_ip1 = sin_i - (alpha * sin_i - beta * cos_i);

      cos_i = cos_ip1;
      sin_i = sin_ip1;
    }
  }

  for(l = 0; l < lmax; l += 2 ) {
    rho_nl->aa[0][l] *= 0.5;
  }

  delete_Array1d(theta);
  delete_Array1d(cos_theta);

  delete_Array1d(u);
  delete_Array1d(r);

  delete_Array2d(rho);
  delete_Array2d(AA);
  delete_Array2d(BB);
  delete_Array2d(rho_l);

  return rho_nl;
}
```

```
extern Array2d* SPT_potential_coeff_corr(Array2d *rho_nl)
{
  int i,j,l;
  int nmax, lmax;
  int nmax_redux, lmax_redux;

  maybelongint sys_size, sys_size_redux;
  maybelongint flag, flag_redux, nrhs = 1;
  maybelongint lwork, rank;
  maybelongint *pivot, *iwork;

  char trans;

  double  even_sum = 0.;
  double odd_sum = 0.;
  double rcond = -1.;

  Array2d *At;
  Array2d *phi_nl, *phi_ln;
  Array2d *Bt, *Bt_redux;

  Array1d *work, *s;

  nmax = rho_nl->nrows;
  lmax = rho_nl->ncols;

  nmax_redux = nmax - 1;
  lmax_redux = lmax - 1;

  sys_size = nmax;
  sys_size_redux = nmax_redux;

  phi_nl = new_Array2d(nmax, lmax);
  phi_ln = new_Array2d(lmax, nmax);

  Bt = new_Array2d(nmax, nmax);
  Bt_redux = new_Array2d(nmax_redux, nmax);

  At = new_Array2d(nmax, nmax);

  pivot = (maybelongint *) malloc(nmax * sizeof(maybelongint));

  for(i = 0; i < lmax; i += 2) {
    for(j = 0; j < nmax; j++) {
      phi_ln->aa[i][j] = rho_nl->aa[j][i];
    }
  }

  for(j = 0; j < nmax; j++) {
    if(j >= 2) At->aa[j-2][j] = 0.0625 * (j-2) * (j-1);
```

```
    if(j >= 1) At->aa[j-1][j] = 0.25 * (j-1);

    At->aa[j][j] = - 0.125 * j * j;

    if(j + 1 < nmax) At->aa[j+1][j] = - 0.25 * (j+1);
    if(j + 2 < nmax) At->aa[j+2][j] = 0.0625 * (j+2) * (j+1);
  }

  for(l = 2; l < lmax; l += 2) {

    for(j = 0; j < nmax; j++) {
      for(i = 0; i < nmax; i++) {
        Bt->aa[j][i] = At->aa[j][i];
        if (j == i) Bt->aa[j][i] -= l*(l+1);
      }
    }

    dgesv_(&sys_size, &nrhs, Bt->aa[0], &sys_size, pivot, phi_ln->aa[l
        ], &sys_size, &flag);

    if (flag != 0) {
      printf("Warning: error solving linear equation.\n");
      printf("l = %i\n", l);
    }
  }

  for(j = 0; j < nmax_redux; j++) {
    for(i = 0; i < nmax; i++) {
      Bt_redux->aa[j][i] = At->aa[j+1][i];
    }
  }

  trans = 'N';

  lwork = -1;

  iwork = (maybelongint *) malloc(100 * sizeof(maybelongint));
  work = new_Array1d(100);

  s = new_Array1d(nmax_redux);

  dgelsd_(&sys_size, &sys_size_redux, &nrhs, Bt_redux->aa[0], &
      sys_size,
          phi_ln->aa[0], &sys_size, s->a, &rcond, &rank, work->a, &
              lwork, iwork, &flag);

  lwork = (maybelongint) work->a[0];

  free(iwork);
  delete_Array1d(work);
```

```
  iwork = (maybelongint *) malloc(lwork * sizeof(maybelongint));
  work = new_Array1d(lwork);

  dgelsd_(&sys_size, &sys_size_redux, &nrhs, Bt_redux->aa[0], &
      sys_size,
          phi_ln->aa[0], &sys_size, s->a, &rcond, &rank, work->a, &
              lwork, iwork, &flag);

  if (flag != 0) printf(”Warning: error solving linear equation in the
       redux case.\n”);

  for(i = nmax - 1; i > 0; i--) {
    phi_ln->aa[0][i] = phi_ln->aa[0][i-1];
  }

  for(i = 1; i < nmax; i += 2) odd_sum += phi_ln->aa[0][i];

  for(i = 2; i < nmax; i += 2) even_sum += phi_ln->aa[0][i];

  phi_ln->aa[0][0] = odd_sum - even_sum;

  for(j = 0; j < lmax; j += 2) {
    for(i = 0; i < nmax; i++) {
      phi_nl->aa[i][j] = phi_ln->aa[j][i];
    }
  }

  delete_Array2d(phi_ln);
  delete_Array2d(Bt);
  delete_Array2d(Bt_redux);
  delete_Array2d(At);

  delete_Array1d(s);
  delete_Array1d(work);

  free(pivot);
  free(iwork);

  return phi_nl;
}

extern Array2d * SPT_disp_z_cspline3(double Dz, Array2d *rho, Array2d
    *dphi)
{
  int nrows, ncols;
  int i,j;

  maybelongint sys_size, nrhs, flag;
```

```c
  double sum;
  double m_drho, q_drho, m_phi, q_phi;

  double inv_Dz = 1. / Dz;
  double Dz3_24 = Dz * Dz * Dz / 24.;
  double Dz_2 = Dz * 0.5;

  Array2d *sigma_z, *bt;

  Array1d *d, *dl;

  nrhs = nrows = rho->nrows;
  ncols = rho->ncols;

  sys_size = ncols - 2;

  sigma_z = new_Array2d(nrows, ncols);

  d = new_Array1d((int) sys_size);
  dl = new_Array1d((int) sys_size);

  bt = new_Array2d(nrows, (int) sys_size);

  for(j = 0; j < sys_size; j++) {
    d->a[j] = 4. * Dz;
  }
  for(j = 0; j < sys_size - 1; j++) {
    dl->a[j] = Dz;
  }

  for(i = 0; i < nrows; i++) {
    for(j = 0; j < sys_size; j++) {
      bt->aa[i][j] = 6. * ((rho->aa[i][j+2] * dphi->aa[i][j+2] - rho->
          aa[i][j+1] * dphi->aa[i][j+1]) -
                          (rho->aa[i][j+1] * dphi->aa[i][j+1] - rho->
                              aa[i][j] * dphi->aa[i][j])) * inv_Dz;
    }
  }

  dptsv_(&sys_size, &nrhs, d->a, dl->a, bt->aa[0], &sys_size, &flag);

  for(i = 0; i < nrows; i++) {
    sum = (rho->aa[i][ncols-1] * dphi->aa[i][ncols-1] + rho->aa[i][
        ncols-2] * dphi->aa[i][ncols-2]) * Dz_2 -
      bt->aa[i][sys_size-1] * Dz3_24;

    sigma_z->aa[i][ncols - 2] = sum;

    for(j = ncols - 3; j > 0; j--) {
```

```
      sum += (rho->aa[i][j+1] * dphi->aa[i][j+1] + rho->aa[i][j] *
          dphi->aa[i][j]) * Dz_2 -
        (bt->aa[i][j] + bt->aa[i][j-1]) * Dz3_24;

      sigma_z->aa[i][j] = sum;
    }
      sum += (rho->aa[i][1] * dphi->aa[i][1] + rho->aa[i][0] * dphi->
          aa[i][0]) * Dz_2 -
        bt->aa[i][0] * Dz3_24;

      sigma_z->aa[i][0] = sum;

    sigma_z->aa[i][ncols-1] = sigma_z->aa[i][ncols-2];
  }

  delete_Array1d(d);
  delete_Array1d(dl);
  delete_Array2d(bt);

  return sigma_z;
}

extern Array2d * SPT_disp_phi_cspline(double Dw, Array2d *f)
{
  int nrows, ncols;
  int i,j;

  maybelongint sys_size, nrhs, flag;

  double sum;
  double Dw3_24 = Dw * Dw * Dw / 24.;
  double Dw_2 = Dw * 0.5;
  double inv_Dw = 1. / Dw;

  Array2d *F, *bt;

  Array1d *d, *dl;

  nrhs = nrows = f->nrows;
  ncols = f->ncols;

  sys_size = ncols - 2;

  F = new_Array2d(nrows, ncols);

  d = new_Array1d((int) sys_size);
  dl = new_Array1d((int) sys_size);

  bt = new_Array2d(nrows, (int) sys_size);
```

```
  for(j = 0; j < sys_size; j++) {
    d->a[j] = 4. * Dw;
  }
  for(j = 0; j < sys_size - 1; j++) {
    dl->a[j] = Dw;
  }

  for(i = 0; i < nrows; i++) {
    for(j = 0; j < sys_size; j++) {
      bt->aa[i][j] = 6. * ((f->aa[i][j+2] - f->aa[i][j+1]) -
                           (f->aa[i][j+1] - f->aa[i][j])) * inv_Dw;
    }
  }

  dptsv_(&sys_size, &nrhs, d->a, dl->a, bt->aa[0], &sys_size, &flag);

  for(i = 0; i < nrows; i++) {

    sum = (f->aa[i][ncols-1] + f->aa[i][ncols-2]) * Dw_2 - bt->aa[i][
        sys_size-1] * Dw3_24;

    F->aa[i][ncols-2] = sum;

    for(j = ncols - 3; j > 0; j--) {

      sum += (f->aa[i][j+1] + f->aa[i][j]) * Dw_2 - (bt->aa[i][j] + bt
          ->aa[i][j-1]) * Dw3_24;

      F->aa[i][j] = sum;
    }
    sum += (f->aa[i][1] + f->aa[i][0]) * Dw_2 - bt->aa[i][0] * Dw3_24;

    F->aa[i][0] = sum;

    F->aa[i][ncols-1] = F->aa[i][ncols-2];
  }

  delete_Array1d(d);
  delete_Array1d(dl);
  delete_Array2d(bt);

  return F;
}

extern
void SPT_pot_grad2(
                   Array1d *R, Array1d *z,
                   Array2d *phi_nl,
                   Array2d **phi_cyl,
                   Array2d **dphi_dR,
```

```
                  Array2d **dphi_dz)
{
  int nrows, ncols;
  int nmax, lmax;
  int i, j, l, n;

  Array2d *pot, *grad_R, *grad_z;

  nrows = R->nrows;
  ncols = z->nrows;

  nmax = phi_nl->nrows;
  lmax = phi_nl->ncols;

  pot = new_Array2d(nrows, ncols);
  grad_R = new_Array2d(nrows, ncols);
  grad_z = new_Array2d(nrows, ncols);

  for(i = 0; i < nrows; i++) {
    double R2 = R->a[i] * R->a[i];
    for(j = 0; j < ncols; j++) {
      double z1 = z->a[j];
      double r1 = sqrt(R2 + z->a[j] * z->a[j]);

      double cos_u = (1. - r1) / (1. + r1);
      double v = z1 / r1;

      double sint_sq = 1. - v*v;
      double sint = sqrt(sint_sq);

      double y0 = 0.5 * (1. + 2.*cos_u + cos_u*cos_u);
      double y1 = (1. + cos_u) / (1. - cos_u);

      double J_Ru = - sint * y0;
      double J_Rv = - v * sint * y1;
      double J_zu = - v * y0;
      double J_zv = sint_sq * y1;

      double sum1 = 0.;
      double sum2 = 0.;
      double sum3 = 0.;

      double Pl = 1.;
      double Pl_1 = 0.;
      double dPl = 0.;

      for(l = 0; l < lmax; l++) {

        double Tn = 1.;
        double dTn = 0.;
```

```
        double Tn1, dTn1;

        for(n = 0; n < nmax; n++) {

          double k_phi = phi_nl->aa[n][l];

          sum1 += k_phi * dTn * Pl;
          sum2 += k_phi * Tn * dPl;
          sum3 += k_phi * Tn * Pl;

          if(n == 0) {
            Tn = cos_u;
            Tn1 = 1.;
            dTn = 1.;
            dTn1 = 0.;
          } else {
            double temp2 = 2. * cos_u * Tn - Tn1;
            double temp3 = 2. * Tn + 2. * cos_u * dTn - dTn1;
            Tn1 = Tn;
            Tn = temp2;
            dTn1 = dTn;
            dTn = temp3;
          }
        }

        dPl = v * dPl + (l+1.) * Pl;
        double temp = ((2.*l + 1.) * v * Pl - l*Pl_1) / (l + 1.);
        Pl_1 = Pl;
        Pl = temp;

        l += 1;

        dPl = v * dPl + (l+1.) * Pl;
        temp = ((2.*l + 1.) * v * Pl - l*Pl_1) / (l + 1.);
        Pl_1 = Pl;
        Pl = temp;
      }
      grad_R->aa[i][j] = J_Ru * sum1 + J_Rv * sum2;
      grad_z->aa[i][j] = J_zu * sum1 + J_zv * sum2;
      pot->aa[i][j] = sum3;
    }
  }

  *phi_cyl = pot;
  *dphi_dR = grad_R;
  *dphi_dz = grad_z;
}
```

C.4 my_project.c

```
#include "my_project.h"

void
PRJ_satoh_decompose(
                     Array2d *sigma_z, Array2d *v_phi_sigma_z,
                     double k,
                     Array2d **sigma_phi, Array2d **v_phi_mean)
{
  double kk = k * k;

  int i, j, imax, jmax;

  Array2d *s_phi, *v_phi;

  imax = sigma_z->nrows;
  jmax = sigma_z->ncols;

  s_phi = new_Array2d(imax, jmax);
  v_phi = new_Array2d(imax, jmax);

  for(i = 0; i < imax; i++) {
    for(j = 0; j < jmax; j++) {

      v_phi->aa[i][j] = k * sqrt(fabs(v_phi_sigma_z->aa[i][j]));
      s_phi->aa[i][j] = sigma_z->aa[i][j] + (1. - kk) * v_phi_sigma_z
          ->aa[i][j];
    }
  }

  *sigma_phi = s_phi;
  *v_phi_mean = v_phi;
}

extern
double
PRJ_cspline_integrate_jacob(
                             double Dw,
                             Array1d *jacob,
                             Array1d *f)
{
  int nrows, ncols;
  int i,j;

  maybelongint sys_size, nrhs, flag;

  double sum;
  double sum1 = 0.;
```

```
  double sum2 = 0.;
  double Dw3 = Dw * Dw * Dw;
  double inv_Dw = 1. / Dw;

  double *m_ptr;

  Array1d *bt;

  Array1d *d, *dl;

  nrows = f->nrows;

  nrhs = 1;
  sys_size = nrows - 2;

  d = new_Array1d(sys_size);
  dl = new_Array1d(sys_size);

  bt = new_Array1d(nrows);

  for(i = 0; i < sys_size; i++) {
    d->a[i] = 4. * Dw;
  }
  for(i = 0; i < sys_size - 1; i++) {
    dl->a[i] = Dw;
  }

  m_ptr = bt->a + 1;

  for(i = 0; i < sys_size; i++) {
        m_ptr[i] = 6. * ((f->a[i+2] * jacob->a[i+2] - f->a[i+1] * jacob
            ->a[i+1]) -
                       (f->a[i+1] * jacob->a[i+1] - f->a[i] * jacob->a
                           [i])) * inv_Dw;
    }

  dptsv_(&sys_size, &nrhs, d->a, dl->a, m_ptr, &sys_size, &flag);

  for(i = 0; i < nrows - 1; i++) {
    sum1 += f->a[i+1] * jacob->a[i+1] + f->a[i] * jacob->a[i];
    sum2 += bt->a[i+1] + bt->a[i];
  }

  sum = sum1 * Dw * 0.5 - sum2 * Dw3 / 24.;

  delete_Array1d(d);
  delete_Array1d(dl);
  delete_Array1d(bt);

  return sum;
```

```
}

extern
void
PRJ_sigma_fields(
                 Array1d *xsi1, Array1d *xsi2, Array1d *xsi3,
                 double Dxsi3_tilde,
                 Array1d *Jxsi3,
                 Array1d *s, double Ds,
                 Array1d *w, double Dw,
                 Array2d *sigma_R, Array2d *sigma_phi, Array2d *v_phi,
                 Array2d *rho,
                 double alpha,
                 Array2d **sigmal_los,
                 Array2d **sigmap_los,
                 Array2d **vp_los,
                 Array2d **v2p_los,
                 Array2d **rho_los)
{
  int i,j,k;

  int n1 = xsi1->nrows;
  int n2 = xsi2->nrows;
  int n3 = xsi3->nrows;

  int nrows = s->nrows;
  int ncols = w->nrows;

  int Rtype, ztype;

  double cos_alpha = cos(alpha);
  double cos2_alpha = cos_alpha * cos_alpha;
  double sin_alpha = sin(alpha);
  double sin2_alpha = sin_alpha * sin_alpha;

  double inv_Ds = 1. / Ds;
  double inv_Dw = 1. / Dw;

  Array1d *rho_P, *rho_Q;
  Array1d *sp_P, *sp_Q;
  Array1d *vp_P, *vp_Q;
  Array1d *vp2_P, *vp2_Q;

  Array2d *sl_los, *sp_los;
  Array2d *v2_los, *v_los;
  Array2d *r_los;

  sl_los = new_Array2d(n1, n2);
  sp_los = new_Array2d(n1, n2);
  v_los = new_Array2d(n1, n2);
```

```c
v2_los = new_Array2d(n1, n2);
r_los = new_Array2d(n1, n2);

rho_P = new_Array1d(n3);
rho_Q = new_Array1d(n3);

sp_P = new_Array1d(n3);
sp_Q = new_Array1d(n3);

vp_P = new_Array1d(n3);
vp_Q = new_Array1d(n3);

vp2_P = new_Array1d(n3);
vp2_Q = new_Array1d(n3);

/****************************************************************/
/* For cicle is performed on the cartesian grid of the los RF, */
/* so that a conversion to firstly the cartesian natural RF,   */
/* and then to the cylindrical coordinates.                    */
/* x = RT_1(alpha) xsi                                          */
/****************************************************************/

for (i = 0; i < n1; i++) {
  double x_P = xsi1->a[i];
  double x_Q = xsi1->a[i];

  double xx_P = x_P * x_P;
  double xx_Q = x_Q * x_Q;

  for (j = 0; j < n2; j++) {
    for (k = 0; k < n3; k++) {
      double temp;
      unsigned int hh_P, ll_P, hh_Q, ll_Q;

      /* From los to natural Cartesian  coordinates. */

      double y_P = fabs(xsi2->a[j] * cos_alpha - xsi3->a[k] *
          sin_alpha); // xsi1, xsi3
      double z_P = fabs(xsi3->a[k] * cos_alpha + xsi2->a[j] *
          sin_alpha);

      double y_Q = fabs(xsi2->a[j] * cos_alpha + xsi3->a[k] *
          sin_alpha); // xsi1, -xsi3
      double z_Q = fabs(-xsi3->a[k] * cos_alpha + xsi2->a[j] *
          sin_alpha);

      /* From natural Cartesian to cylindrical. */

      double R_P = sqrt(xx_P + y_P*y_P);
      double cos_phi_P = x_P / R_P;
```

```
    double sin_phi_P = y_P / R_P;

    double R_Q = sqrt(xx_Q + y_Q*y_Q);
    double cos_phi_Q = x_Q / R_Q;
    double sin_phi_Q = y_Q / R_Q;

    double cos2_phi_P = cos_phi_P * cos_phi_P;
    double sin2_phi_P = sin_phi_P * sin_phi_P;

    double cos2_phi_Q = cos_phi_Q * cos_phi_Q;
    double sin2_phi_Q = sin_phi_Q * sin_phi_Q;

    /* Remapping R and z in s and w */

    double s_bar_P = 2. * atan(R_P); // R > 0, hence 0 <= atan(R) <= Pi/2
    double w_bar_P = 2. * atan(z_P); // z > 0, hence 0 <= atan(z) <= Pi/2

    double s_bar_Q = 2. * atan(R_Q); // R > 0, hence 0 <= atan(R) <= Pi/2
    double w_bar_Q = 2. * atan(z_Q); // z > 0, hence 0 <= atan(z) <= Pi/2

    /* Bi-linear interpolation of sigma_R, sigma_phi e v_phi in P and Q*/

    if(s_bar_P <= s->a[0]) {
      hh_P = 0;
    } else if(s_bar_P >= s->a[nrows-1]) {
      hh_P = nrows - 2;
    } else {
      hh_P = (unsigned int) ((s_bar_P * inv_Ds) - 0.5);
    }

    if(w_bar_P <= w->a[0]) {
      ll_P = 0;
    } else if(w_bar_P >= w->a[ncols-1]) {
      ll_P = ncols - 2;
    } else {
      ll_P = (unsigned int) ((w_bar_P * inv_Dw) - 0.5);
    }

    if(s_bar_Q <= s->a[0]) {
      hh_Q = 0;
    } else if(s_bar_Q >= s->a[nrows-1]) {
      hh_Q = nrows - 2;
    } else {
      hh_Q = (unsigned int) ((s_bar_Q * inv_Ds) - 0.5);
    }
```

```
    if(w_bar_Q <= w->a[0]) {
      ll_Q = 0;
    } else if(w_bar_Q >= w->a[ncols-1]) {
      ll_Q = ncols - 2;
    } else {
      ll_Q = (unsigned int) ((w_bar_Q * inv_Dw) - 0.5);
    }

    double t1_P = (s_bar_P - s->a[hh_P]) / (s->a[hh_P+1] - s->a[
        hh_P]);
    double t2_P = (w_bar_P - w->a[ll_P]) / (w->a[ll_P+1] - w->a[
        ll_P]);

    double t1_Q = (s_bar_Q - s->a[hh_Q]) / (s->a[hh_Q+1] - s->a[
        hh_Q]);
    double t2_Q = (w_bar_Q - w->a[ll_Q]) / (w->a[ll_Q+1] - w->a[
        ll_Q]);

    double sigma_R_bar_P = (1. - t1_P) * (1. - t2_P) * sigma_R->aa
        [hh_P][ll_P] +
      t1_P * (1. - t2_P) * sigma_R->aa[hh_P+1][ll_P] +
      t1_P * t2_P * sigma_R->aa[hh_P+1][ll_P+1] +
      (1. - t1_P) * t2_P * sigma_R->aa[hh_P][ll_P+1];

    double sigma_phi_bar_P = (1. - t1_P) * (1. - t2_P) * sigma_phi
        ->aa[hh_P][ll_P] +
      t1_P * (1. - t2_P) * sigma_phi->aa[hh_P+1][ll_P] +
      t1_P * t2_P * sigma_phi->aa[hh_P+1][ll_P+1] +
      (1. - t1_P) * t2_P * sigma_phi->aa[hh_P][ll_P+1];

    double v_phi_bar_P = (1. - t1_P) * (1. - t2_P) * v_phi->aa[
        hh_P][ll_P] +
      t1_P * (1. - t2_P) * v_phi->aa[hh_P+1][ll_P] +
      t1_P * t2_P * v_phi->aa[hh_P+1][ll_P+1] +
      (1. - t1_P) * t2_P * v_phi->aa[hh_P][ll_P+1];

    double sigma_R_bar_Q = (1. - t1_Q) * (1. - t2_Q) * sigma_R->aa
        [hh_Q][ll_Q] +
      t1_Q * (1. - t2_Q) * sigma_R->aa[hh_Q+1][ll_Q] +
      t1_Q * t2_Q * sigma_R->aa[hh_Q+1][ll_Q+1] +
      (1. - t1_Q) * t2_Q * sigma_R->aa[hh_Q][ll_Q+1];

    double sigma_phi_bar_Q = (1. - t1_Q) * (1. - t2_Q) * sigma_phi
        ->aa[hh_Q][ll_Q] +
      t1_Q * (1. - t2_Q) * sigma_phi->aa[hh_Q+1][ll_Q] +
      t1_Q * t2_Q * sigma_phi->aa[hh_Q+1][ll_Q+1] +
      (1. - t1_Q) * t2_Q * sigma_phi->aa[hh_Q][ll_Q+1];

    double v_phi_bar_Q = (1. - t1_Q) * (1. - t2_Q) * v_phi->aa[
```

```
        hh_Q][ll_Q] +
      t1_Q * (1. - t2_Q) * v_phi->aa[hh_Q+1][ll_Q] +
      t1_Q * t2_Q * v_phi->aa[hh_Q+1][ll_Q+1] +
      (1. - t1_Q) * t2_Q * v_phi->aa[hh_Q][ll_Q+1];

    double rho_bar_P = (1. - t1_P) * (1. - t2_P) * rho->aa[hh_P][
        ll_P] +
      t1_P * (1. - t2_P) * rho->aa[hh_P+1][ll_P] +
      t1_P * t2_P * rho->aa[hh_P+1][ll_P+1] +
      (1. - t1_P) * t2_P * rho->aa[hh_P][ll_P+1];

    double rho_bar_Q = (1. - t1_Q) * (1. - t2_Q) * rho->aa[hh_Q][
        ll_Q] +
      t1_Q * (1. - t2_Q) * rho->aa[hh_Q+1][ll_Q] +
      t1_Q * t2_Q * rho->aa[hh_Q+1][ll_Q+1] +
      (1. - t1_Q) * t2_Q * rho->aa[hh_Q][ll_Q+1];

    /* Density. */

    rho_P->a[k] = rho_bar_P;
    rho_Q->a[k] = rho_bar_Q;

    /* Computing sigma_p, v_p and v_p^2 */

    sp_P->a[k] = sin2_alpha * (sigma_R_bar_P * sin2_phi_P +
        sigma_phi_bar_P * cos2_phi_P) +
      cos2_alpha * sigma_R_bar_P;
    temp = -sin_alpha * cos_phi_P * v_phi_bar_P;

    /* Check against division by zero error */

    if (rho_bar_P == 0) {
      vp2_P->a[k] = 0.;
    } else {
      vp2_P->a[k] = temp * temp / rho_bar_P;
    }

    vp_P->a[k] = temp;

    sp_Q->a[k] = sin2_alpha * (sigma_R_bar_Q * sin2_phi_Q +
        sigma_phi_bar_Q * cos2_phi_Q) +
      cos2_alpha * sigma_R_bar_Q;
    temp = -sin_alpha * cos_phi_Q * v_phi_bar_Q;

    /* Check against division by zero error */

    if (rho_bar_Q == 0.) {
      vp2_Q->a[k] = 0.;
    } else {
      vp2_Q->a[k] = temp * temp / rho_bar_Q;
```

```
      }

      vp_Q->a[k] = temp;

    } /* For k cicle ends */

    /* Los integration */

    double r_los_P = PRJ_cspline_integrate_jacob(Dxsi3_tilde, Jxsi3, rho_P);
    double r_los_Q = PRJ_cspline_integrate_jacob(Dxsi3_tilde, Jxsi3, rho_Q);

    double sp_los_P = PRJ_cspline_integrate_jacob(Dxsi3_tilde, Jxsi3, sp_P);
    double sp_los_Q = PRJ_cspline_integrate_jacob(Dxsi3_tilde, Jxsi3, sp_Q);

    double vp_los_P = PRJ_cspline_integrate_jacob(Dxsi3_tilde, Jxsi3, vp_P);
    double vp_los_Q = PRJ_cspline_integrate_jacob(Dxsi3_tilde, Jxsi3, vp_Q);

    double vp2_los_P = PRJ_cspline_integrate_jacob(Dxsi3_tilde, Jxsi3, vp2_P);
    double vp2_los_Q = PRJ_cspline_integrate_jacob(Dxsi3_tilde, Jxsi3, vp2_Q);

    // sigma2_l_los = sp_los + vp2_los - vp_los**2 e vp_los.

    double rho_ij =  r_los_P + r_los_Q;

    double vp_ij = vp_los_P + vp_los_Q;
    double vp2_ij = vp2_los_P + vp2_los_Q;
    double sp_ij = sp_los_P + sp_los_Q;

    r_los->aa[i][j] = rho_ij;
    v_los->aa[i][j] = vp_ij;
    v2_los->aa[i][j] = vp2_ij;
    sp_los->aa[i][j] = sp_ij;

    /* Check against division by zero error */

    if (rho_ij == 0.) {
      sl_los->aa[i][j] = 0.;
    } else {
      sl_los->aa[i][j] = (sp_ij) + (vp2_ij) - (vp_ij * vp_ij) / (rho_ij);
    }
  }
```

```
  }

  *rho_los = r_los;

  *sigmal_los = sl_los;
  *sigmap_los = sp_los;

  *vp_los = v_los;
  *v2p_los = v2_los;

  delete_Array1d(sp_P);
  delete_Array1d(sp_Q);
  delete_Array1d(vp_P);
  delete_Array1d(vp_Q);
  delete_Array1d(vp2_P);
  delete_Array1d(vp2_Q);
}

extern Array2d* PRJ_construct_cspline(double Dw, Array2d *f)
{
  maybelongint sys_size, nrhs, flag;

  int nrows, ncols;
  int i,j;

  double sum;
  double Dw3 = Dw * Dw * Dw;
  double inv_Dw = 1. / Dw;

  Array2d *bt, *m_spline;

  Array1d *d, *dl;

  nrhs = nrows = f->nrows;
  ncols = f->ncols;

  sys_size = ncols - 2;

  d = new_Array1d(sys_size);
  dl = new_Array1d(sys_size);

  bt = new_Array2d(nrows, (int) sys_size);
  m_spline = new_Array2d(nrows, ncols);

  for(j = 0; j < sys_size; j++) {
    d->a[j] = 4. * Dw;
  }
  for(j = 0; j < sys_size - 1; j++) {
    dl->a[j] = Dw;
  }
```

```
  for(i = 0; i < nrows; i++) {
    for(j = 0; j < sys_size; j++) {
      bt->aa[i][j] = 6. * ((f->aa[i][j+2] - f->aa[i][j+1]) -
                           (f->aa[i][j+1] - f->aa[i][j])) * inv_Dw;
    }
  }

  dptsv_(&sys_size, &nrhs, d->a, dl->a, bt->aa[0], &sys_size, &flag);

  for(i = 0; i < nrows; i++) {
    for(j = 1; j < ncols-1; j++) {
      m_spline->aa[i][j] = bt->aa[i][j-1];
    }
  }

  delete_Array1d(d);
  delete_Array1d(dl);
  delete_Array2d(bt);

  return m_spline;
}

extern
Array2d*
remap2Sph(
          Array2d *old,
          Array1d *x1_t,
          Array1d *x2_t,
          Array1d *r,
          Array1d *theta)
{
  int i,j;
  int ii, jj;

  int n1 = x1_t->nrows;
  int n2 = x2_t->nrows;

  int nr = r->nrows;
  int nt = theta->nrows;

  double Dx1_t = M_PI / n1;
  double Dx2_t = M_PI / n2;

  double inv_Dx1_t = 1. / Dx1_t;
  double inv_Dx2_t = 1. / Dx2_t;

  double x1_bar, x2_bar;
  double x1_bar_t, x2_bar_t;
  double t1, t2;
```

```
  Array1d *cos_t = new_Array1d(nt);
  Array1d *sin_t = new_Array1d(nt);
  Array2d *new = new_Array2d(nr, nt);

  for(j = 0; j < nt; j++) {
    cos_t->a[j] = cos(theta->a[j]);
    sin_t->a[j] = sin(theta->a[j]);
  }

  for(i = 0; i < nr; i++) {
    double r_i = r->a[i];
    for(j = 0; j < nt; j++) {
      x1_bar = r_i * cos_t->a[j];
      x2_bar = r_i * sin_t->a[j];

      x1_bar_t = 2. * atan(x1_bar);
      x2_bar_t = 2. * atan(x2_bar);

      ii = floor(x1_bar_t * inv_Dx1_t - 0.5);
      jj = floor(x2_bar_t * inv_Dx2_t - 0.5);

      if(ii < 0) {
        ii = 0;
      } else if(ii > n1 - 2) {
        ii = n1 - 2;
      }
      if(jj < 0) {
        jj = 0;
      } else if(jj > n2 - 2) {
        jj = n2 - 2;
      }

      t1 = (x1_bar_t - x1_t->a[ii]) / (x1_t->a[ii+1] - x1_t->a[ii]);
      t2 = (x2_bar_t - x2_t->a[jj]) / (x2_t->a[jj+1] - x2_t->a[jj]);

      new->aa[i][j] = (1. - t1) * (1. - t2) * old->aa[ii][jj] + t1 *
          (1. - t2) * old->aa[ii+1][jj]
        + t1 * t2 * old->aa[ii+1][jj+1] + (1. - t1) * t2 * old->aa[ii
            ][jj+1];
    }
  }
  return new;
}

extern
void
PRJ_HalfLight(
              Array2d *rho,
              Array1d *Jr,
```

```
                Array1d *r,
                Array1d *r_tilde,
                Array1d *theta,
                double *TotalLight,
                double *HalfLight,
                int *idx)
{
  int i,j;

  int nr = r_tilde->nrows;
  int nt = theta->nrows;

  double Dtheta = 0.5 * M_PI / nt;
  double Dtheta_2 = 0.5 * Dtheta;
  double Dtheta3_24 = Dtheta * Dtheta * Dtheta / 24.;

  Array2d *rho_t = new_Array2d(nr, nt);
  Array2d *m_theta = new_Array2d(nr, nt);
  Array1d *f_r = new_Array1d(nr);
  Array1d *partial_sum = new_Array1d(nr);

  for(i = 0; i < nr; i++) {
    double k = Jr->a[i] * r->a[i];
    for(j = 0; j < nt; j++) {
      rho_t->aa[i][j] = rho->aa[i][j] * k;
    }
  }

  /* Theta integration */

  m_theta = PRJ_construct_cspline(Dtheta, rho_t);

  {
    double sum1, sum2;
    for(i = 0; i < nr; i++) {
      for(j = 0, sum1 = sum2 = 0.; j < nt-1; j++) {
        sum1 += rho_t->aa[i][j+1] + rho_t->aa[i][j];
        sum2 += m_theta->aa[i][j+1] + m_theta->aa[i][j];
      }
      f_r->a[i] = sum1 * Dtheta_2 - sum2 * Dtheta3_24;
    }
  }

  /* r integration */

  {
    maybelongint sys_size, nrhs, flag;

    double sum1, sum2;

```

```
  double Dr = M_PI / nr;
  double Dr3 = Dr * Dr * Dr;
  double inv_Dr = 1. / Dr;

  double *m_ptr;

  Array1d *bt;

  Array1d *d, *dl;


  nrhs = 1;
  sys_size = nr - 2;

  d = new_Array1d(sys_size);
  dl = new_Array1d(sys_size);

  bt = new_Array1d(nr);

  for(i = 0; i < sys_size; i++) {
    d->a[i] = 4. * Dr;
  }
  for(i = 0; i < sys_size - 1; i++) {
    dl->a[i] = Dr;
  }

  m_ptr = bt->a + 1;

  for(i = 0; i < sys_size; i++) {
    m_ptr[i] = 6. * ((f_r->a[i+2] - f_r->a[i+1]) -
                     (f_r->a[i+1] - f_r->a[i])) * inv_Dr;
  }

  dptsv_(&sys_size, &nrhs, d->a, dl->a, m_ptr, &sys_size, &flag);

  for(i = 0, sum1 = sum2 = 0.; i < nr - 1; i++) {
    sum1 += f_r->a[i+1] + f_r->a[i];
    sum2 += bt->a[i+1] + bt->a[i];

    partial_sum->a[i] = sum1 * Dr * 0.5 - sum2 * Dr3 / 24.;
  }
  partial_sum->a[nr-1] = partial_sum->a[nr-2];

  delete_Array1d(d);
  delete_Array1d(dl);
  delete_Array1d(bt);
}

/* Half light radius */

```

```
  {
    double tot = partial_sum->a[nr-1];
    double half;

    int  i_upper = nr - 1;
    int  i_lower = 0;

    while (i_upper - i_lower > 1) {
      i = (i_upper + i_lower) / 2;

      half = partial_sum->a[i];

      if (half > tot * 0.5) {
        i_upper = i;
      } else if (half <= tot * 0.5) {
        i_lower = i;
      }
    }

    *idx = i;
    *TotalLight = tot;
    *HalfLight = half;
  }

  delete_Array2d(rho_t);
  delete_Array2d(m_theta);

  delete_Array1d(f_r);
  delete_Array1d(partial_sum);
}

extern
Array1d*
PRJ_IntegrateOnCircle(
                       Array2d *f,
                       Array1d *Jr,
                       Array1d *r,
                       Array1d *r_tilde,
                       Array1d *theta,
                       int rt_max)
{
  int i,j;

  int nr = r_tilde->nrows;
  int nt = theta->nrows;

  double Dtheta = 0.5 * M_PI / nt;
  double Dtheta_2 = 0.5 * Dtheta;
  double Dtheta3_24 = Dtheta * Dtheta * Dtheta / 24.;

```

```
  Array2d *f_tilde = new_Array2d(nr, nt);
  Array2d *m_theta = new_Array2d(nr, nt);

  Array1d *f_r = new_Array1d(nr);
  Array1d *partial_sum = new_Array1d(nr);

  for(i = 0; i < nr; i++) {
    double k = Jr->a[i] * r->a[i];
    for(j = 0; j < nt; j++) {
      f_tilde->aa[i][j] = f->aa[i][j] * k;
    }
  }

  /* Theta integration */

  m_theta = PRJ_construct_cspline(Dtheta, f_tilde);

  {
    double sum1, sum2;
    for(i = 0; i < nr; i++) {
      for(j = 0, sum1 = sum2 = 0.; j < nt-1; j++) {
        sum1 += f_tilde->aa[i][j+1] + f_tilde->aa[i][j];
        sum2 += m_theta->aa[i][j+1] + m_theta->aa[i][j];
      }
      f_r->a[i] = 4.*(sum1 * Dtheta_2 - sum2 * Dtheta3_24);
    }
  }

  /* r integration */

  {
    maybelongint sys_size, nrhs, flag;

    double sum1, sum2;

    double Dr = M_PI / nr;
    double Dr3 = Dr * Dr * Dr;
    double inv_Dr = 1. / Dr;

    double *m_ptr;

    Array1d *bt;

    Array1d *d, *dl;


    nrhs = 1;
    sys_size = nr - 2;

    d = new_Array1d(sys_size);
```

```
    dl = new_Array1d(sys_size);

    bt = new_Array1d(nr);

    for(i = 0; i < sys_size; i++) {
      d->a[i] = 4. * Dr;
    }
    for(i = 0; i < sys_size - 1; i++) {
      dl->a[i] = Dr;
    }

    m_ptr = bt->a + 1;

    for(i = 0; i < sys_size; i++) {
      m_ptr[i] = 6. * ((f_r->a[i+2] - f_r->a[i+1]) -
                       (f_r->a[i+1] - f_r->a[i])) * inv_Dr;
    }

    dptsv_(&sys_size, &nrhs, d->a, dl->a, m_ptr, &sys_size, &flag);

    for(i = 0, sum1 = sum2 = 0.; i < nr - 1; i++) {
      sum1 += f_r->a[i+1] + f_r->a[i];
      sum2 += bt->a[i+1] + bt->a[i];

      partial_sum->a[i] = sum1 * Dr * 0.5 - sum2 * Dr3 / 24.;
    }
    partial_sum->a[nr-1] = partial_sum->a[nr-2];

    delete_Array1d(d);
    delete_Array1d(dl);
    delete_Array1d(bt);
  }

  delete_Array2d(f_tilde);
  delete_Array2d(m_theta);

  delete_Array1d(f_r);

  return partial_sum;
}


extern
double
PRJ_sigma_vir(
              Array2d *f1,
              Array2d *f2,
              Array1d *JR,
              Array1d *Jz,
              Array1d *R,
```

```
              Array1d *R_tilde,
              Array1d *z_tilde)
{
  int i,j;

  int nR = R_tilde->nrows;
  int nz = z_tilde->nrows;

  double Dz_t = M_PI / nz;
  double Dz_t_2 = 0.5 * Dz_t;
  double Dz_t3_24 = Dz_t * Dz_t * Dz_t / 24.;

  double result;

  Array2d *f = new_Array2d(nR, nz);
  Array2d *m_z = new_Array2d(nR, nz);
  Array1d *f_R = new_Array1d(nR);

  for(i = 0; i < nR; i++) {
    double j1 = JR->a[i] * R->a[i];
    for(j = 0; j < nz; j++) {
      double j2 = Jz->a[j];
      f->aa[i][j] = f1->aa[i][j] * f2->aa[i][j] * j1 * j2;
    }
  }


  m_z = PRJ_construct_cspline(Dz_t, f);

  {
    double sum1, sum2;
    for(i = 0; i < nR; i++) {
      for(j = 0, sum1 = sum2 = 0.; j < nz-1; j++) {
        sum1 += f->aa[i][j+1] + f->aa[i][j];
        sum2 += m_z->aa[i][j+1] + m_z->aa[i][j];
      }
      f_R->a[i] = sum1 * Dz_t_2 - sum2 * Dz_t3_24;
    }
  }

  {
    maybelongint flag;
    maybelongint nrhs = 1;
    maybelongint sys_size = nR - 2;

    double DR_t = M_PI / nR;
    double DR_t_2 = 0.5 * DR_t;
    double DR_t3_24 = DR_t * DR_t * DR_t / 24.;
    double inv_DR_t = 1. / DR_t;

```

```
    double sum1, sum2;

    double *m_ptr;

    Array1d *bt = new_Array1d(nR);

    Array1d *d = new_Array1d(sys_size);
    Array1d *dl = new_Array1d(sys_size);

    for(i = 0; i < sys_size; i++) {
      d->a[i] = 4. * DR_t;
    }
    for(i = 0; i < sys_size - 1; i++) {
      dl->a[i] = DR_t;
    }

    m_ptr = bt->a + 1;

    for(i = 0; i < sys_size; i++) {
      m_ptr[i] = 6. * ((f_R->a[i+2] - f_R->a[i+1]) -
                        (f_R->a[i+1] - f_R->a[i])) * inv_DR_t;
    }

    dptsv_(&sys_size, &nrhs, d->a, dl->a, m_ptr, &sys_size, &flag);

    for(i = 0, sum1 = sum2 = 0.; i < nR - 1; i++) {
      sum1 += f_R->a[i+1] + f_R->a[i];
      sum2 += bt->a[i+1] + bt->a[i];
    }

    result = sum1 * DR_t_2 - sum2 * DR_t3_24;

    delete_Array1d(d);
    delete_Array1d(dl);
    delete_Array1d(bt);
  }

  delete_Array2d(f);
  delete_Array2d(m_z);

  delete_Array1d(f_R);

  return 2. * M_PI * result;
}
```

Acknowledgments

I would like to acknowledge the contributions of all those who have helped me with this work. In particular I would like to thank Luca Ciotti for his invaluable lessons of astrophysics and life, and Pasquale Londrillo for his support and priceless suggestions in developing numerical code. I would like to thank also Barbara Lanzoni for her willingness and patience.

I would like to thank all the students that had been shared the Thursday's briefings with me, in particular: Matteo Barnabè (aka “Il Marchese”), Silvia Bonoli, Sara Caucci, Sinue Serra, Daniele Fantin, Emanuele Spitoni.

In addition I would like to thank many people not directly involved in this work, but whose presence was important during these years: Luca Angeretti, Gianni Bernardi, Manuela Calabrese, Erika De Simone, Giuliana Fiorentino, Italo Foppiani, Marcello Giroletti, Myriam Gitti, Andrea Gualandi, Marcella Maio, Andrea Melandri, Carlo Nipoti, Francesco Poppi, Claudia Porcu, Elena Sabbi, Antonio Sollima, Fabio Terenziani, Elena Valenti.

I would like thank all the Open Source community that supported me in technicalities and computer-related problems. In particular I would like to mention: Fernando Pérez, David Beazly, Travis Oliphant, Martin Costabel, André Wobst, Jörg Lehmann, Jeff Whitaker, all the Fink Core Team, Guido van Rossum and all the Python community, and many many others that I'm not able to remember now.

I would like also thank my “crew”: Umbi, Jacopo, Gigi, Alessio, Inno, Ste, Filo, Ro, Vitti, Mata, Luga, Kappa, “il Giudice”, Letal, Bri, Cino, Pietro, Paglio, Piter, Dona, Anto, Dejano, for helping me in wasting my nights and early mornings chasing our *Chimera*.

A special thanks to my parents Piero and Simonetta, and to my sisters Francesca and Benedetta, without their love and support all this work would

have not been possible. Thanks also to the “Altipiano di Lavarone”, because wherever I am, I know it is always there.

Bibliography

Abramowitz, M. & Stegun, I. A. 1972, Handbook of Mathematical Functions with Formulas, Graphs and Mathematical Tables (National Bureau of Standards)

Anderson, E., Bai, Z., Bischof, C., et al. 1999, LAPACK Users' Guide, 3rd edn. (Philadelphia, PA: Society for Industrial and Applied Mathematics)

Arfken, G. B. & Weber, H. J. 2000, Mathematical methods for physicists, 5th edn. (Academic Press)

Barkana, R. 1997, ApJ, 489, 21

Barnabè, M., Fraternali, F., Ciotti, L., & Sancisi, R. 2005, A&A, *submitted*

Bender, R., Burstein, D., & Faber, S. M. 1992, ApJ, 399, 462

Bender, R., Burstein, D., & Faber, S. M. 1993, ApJ, 411, 153

Bertin, G., Ciotti, L., & Principe, M. D. 2002, A&A, 386, 149

Binney, J. 1976, MNRAS, 177, 19

Binney, J. 1978, MNRAS, 183, 501

Binney, J. 1981, MNRAS, 196, 455

Binney, J., Davies, R. L., & Illingworth, G. 1990, ApJ, 361, 78

Binney, J. & Tremaine, S. 1987, Galactic Dynamics (Princeton University Press)

Bower, R. G., Lucey, J. R., & Ellis, R. S. 1992, MNRAS, 254, 601

Burstein, D., Davies, R. L., Dressler, A., Faber, S. M., & Lynden-Bell, D. 1988, in Proceedings of the Fifth Workshop of the Advanced School of Astronomy, ed. Dordrecht (Kluwer Academic Publishers)

Canuto, C., Hussani, M., Y., Quarteroni, A., & Zang, T., A. 1987, Spectral Methods in Fluid Dynamics (Springer-Verlag)

Caon, N., Capaccioli, M., & D'Onofrio, M. 1993, MNRAS, 265, 1013

Chandrasekhar, S. 1969, Ellipsoidal figures of equilibrium (Yale University Press, New Haven)

Ciotti, L. 1997, in Galaxy Scaling Relations: Origins, Evolution and Applications, ed. L. N. da Costa & A. Renzini, ESO (38)

Ciotti, L. 2000, Lecture Notes on Stellar Dynamics (Scuola Normale Superiore Pisa)

Ciotti, L. & Bertin, G. 2005, A&A, *submitted*

Ciotti, L. & Lanzoni, B. 1997, A&A, 321, 724

Ciotti, L., Lanzoni, B., & Renzini, A. 1996, MNRAS, 282, 1

Ciotti, L. & Pellegrini, S. 1992, MNRAS, 255, 561

Ciotti, L. & Pellegrini, S. 1996, MNRAS, 279, 240

Ciotti, L. & van Albada, T. S. 2001, ApJ, 552, L13

Courant, R. & Hilbert, D. 1953, Methods of Mathematical Physics (New York: Interscience Publication)

Davies, R. L., Efstathiou, G., Fall, S. M., Illingworth, G., & Schechter, P. L. 1983, ApJ, 266, 41

de Vaucouleurs, G. 1948, Ann. d'Astroph.

de Zeeuw, T. 2001, in Black Holes in Binaries and Galactic Nuclei, 78

Dehnen, W. 1993, MNRAS, 265, 250

Djorgovski, G. & Davis, M. 1987, ApJ, 313, 59

Djorgovski, S. G. 1995, ApJ, 438, L29

Dressler, A., Lynden-Bell, D., Burstein, D., et al. 1987, ApJ, 313, 42

Eggen, O. J., Lynden-Bell, D., & Sandage, A. R. 1962, ApJ, 136, 748

Evans, N. M. 1994, MNRAS, 267, 333

Evans, N. M. & de Zeeuw, P. T. 1994, MNRAS, 271, 202

Faber, S. M., Dressler, A., Davies, R. L., et al. 1987, in Nearly Normal galaxies: From the Planck time to the present, ed. S. M. Faber (Springer, New York), 175–183

Faber, S. M. & Jackson, R. E. 1976, ApJ, 204, 668

Ferrarese, L. 2001, in Current High-Energy Emission around Black Holes, ed. C. H. Lee & H. Y. Chang (Singapore: World Scientific Publishing), 3–8

Ferrarese, L. & Merritt, D. 2000, ApJ, 539, L9

Ferrers, N. M. 1877, Quart. J. Pure and Appl. Math., 14

Gebhardt, K., Bender, R., Bower, G., et al. 2000, ApJ, 539, L13

Gonzáles, A. C. & van Albada, T. S. 2003, MNRAS

Gottlieb, D. & Orszag, S. A. 1977, Numerical analysis of spectral methods : theory and applications (Philadelphia: Society for Industrial and Applied Mathematics)

Graham, A. & Colless, M. 1995, MNRAS, 445, 55

Hernquist, L. 1990, ApJ, 356, 359

Hjorth, J. & Madsen, J. 1995, ApJ, 445, 55

Illingworth, G. 1977, ApJ, 218, L43

Jaffe, W. 1983, MNRAS, 202, 995

Jørgensen, I., Franx, M., Hjorth, J., & van Dokkum, P. G. 1999, MNRAS, 308, 833

Jørgensen, I., Franx, M., & Kjærgaard, P. 1993, ApJ, 411, 34

Jørgensen, I., Franx, M., & Kjærgaard, P. 1996, MNRAS, 280, 167

Kellogg, O. D. 1953, Foundation of potential theory (Dove, New York)

Koopmans, L. V. E. & Treu, T. 2002, ApJ, 568, L5

Kormendy, J. 1977, ApJ, 218, 333

Kormendy, J. & Richstone, D. 1995, ARA&A, 33, 581

Lanzoni, B. & Ciotti, L. 2003, A&A, 404, 819

Londrillo, P. & Messina, A. 1990, MNRAS, 242, 595

Lynden-Bell, D. 1962, MNRAS, 123, 447

Magorrian, J., Tremaine, S., Richstone, D. O., et al. 1998, AJ, 115, 2285

Merritt, D. & Ferrarese, L. 2001a, MNRAS, 320, L30

Merritt, D. & Ferrarese, L. 2001b, ApJ, 547, 140

Morse, P. M. & Feshbach, H. 1953, Methods of Theoretical Physics, International Series in Pure and Applied Physics (New York: McGraw-Hill)

Nagai, R. & Miyamoto, M. 1976, Publ. Astron. Soc. Japan, 28, 1

Narayan, R. & Bartelmann, M. 1999, in Formation of structure in the Universe, ed. A. Dekel & J. P. Ostriker (Cambridge University Press)

Nipoti, C., Londrillo, P., & Ciotti, L. 2002, MNRAS, 332, 901

Nipoti, C., Londrillo, P., & Ciotti, L. 2003a, in The Mass of Galaxies at Low and High Redshift, 70

Nipoti, C., Londrillo, P., & Ciotti, L. 2003b, MNRAS, 342, 501

Pahre, M. A., de Carvalho, R. R., & Djorgovski, S. G. 1998, AJ, 116, 1606

Pentericci, L., Ciotti, L., & Renzini, A. 1995, Astrophys. Lett. Commun., 33, 213

Press, W. H., Teukolsky, S. A., Vetterling, W. T., & Flannery, B. P. 1992, Numerical Recipes in C (Cambridge University Press)

Prugniel, P. & Simien, F. 1994, A&A, 282, L1

Prugniel, P. & Simien, F. 1996, A&A, 309, 749

Prugniel, P. & Simien, F. 1997, A&A, 321, 111

Qian, E. E., de Zeeuw, P. T., van der Marel, R. P., & Hunter, C. 1995, MNRAS, 274, 602

Refsdal, S. 1964, MNRAS, 128, 370

Renzini, A. & Ciotti, L. 1993, ApJ, 416, L49

Riciputi, A., Lanzoni, B., Bonoli, S., & Ciotti, L. 2005, A&A, 443, 133

Roberts, P. H. 1962, ApJ, 136, 1108

Saglia, R. P., Bender, R., & Dressler, A. 1993, A&A, 279, 75

Satoh, C. 1980, PASJ, 32, 41

Schechter, P. L., Bailyn, C. D., Barr, R., et al. 1997, ApJ, 475, L85

Schwarzschild, M. 1979, ApJ, 232, 236

Scodeggio, M., Gavazzi, G., Belsole, E., Pierini, D., & Boselli, A. 1998, MNRAS, 301, 1001

Sersic, J. L. 1968, Atlas de galaxias australes (Cordoba, Argentina: Observatorio Astronomico, 1968)

Stäckel, P. 1890, Math. Ann., 35, 91

Stoer, J. & Bulirsch, R. 1980, Introduction to Numerical Analysis (Springer-Verlag)

Tassoul, J.-L. 1978, Theory of rotating stars, Princeton Series in Astrophysics (Princeton University Press)

Tremaine, S., Gebhardt, K., Bender, R., et al. 2002, ApJ, 574, 740

Tremaine, S., Richstone, D. O., Byun, Y., et al. 1994, AJ, 107, 634

Treu, T. & Koopmans, L. V. E. 2002a, ApJ, 575, 87

Treu, T. & Koopmans, L. V. E. 2002b, MNRAS, 337, L6

van Albada, T. S., Bertin, G., & Stiavelli, M. 1995, MNRAS, 276

van der Marel, R. P. 1991, MNRAS, 253, 710

van der Marel, R. P. 1999, AJ, 117, 744

van der Marel, R. P., Binney, J., & Davies, R. L. 1990, MNRAS, 245, 582

Weymann, R. J., Latham, D., Roger, J., et al. 1980, Nature, 285, 641